Université du Québec

INRS-Eau, Terre et Environment

Caractérisation quantitative des graviers fluviaux pour la modélisation de la disponibilité d'interstices utilisables par le saumon Atlantique (*Salmo salar*) juvénile en comportement hivernal

Par

Patrice Carbonneau

Thèse présentée

Pour l'obtention

du grade de Philosophiae doctor (Ph.D.)

en sciences de la terre

Jury

Président du jury et examinateur interne	Normand Tassé, INRS-Eau, Terre et Environment
Examinateurs externes	Michel Lapointe, Département de Géographie, Université McGill
	Alfonso Condal, Sciences Géomatiques, Université Laval
Directeur de recherche	Normand Bergeron, INRS-Eau, Terre et Environment
Co-directeur de recherche	Stuart Lane, School of Geography, University of Leeds, UK.

Imagination is more important than knowledge

Albert Einstein

Remerciements

Résumé

Pendant la saison hivernale, les saumons juvéniles s'enfouissent dans les interstices du substrat afin d'échapper à la prédation et de minimiser leurs dépenses énergétiques. L'habitat interstitiel est donc essentiel à la survie hivernale de l'espèce. Pour des fins de gestion, il s'avère nécessaire d'évaluer la disponibilité d'interstices offerts par un substrat de rivière donné. Les méthodes actuelles de caractérisation ne sont basées que sur une description de la granulométrie du substrat. L'agencement spatial des roches a toutefois une influence importante sur la géométrie interstitielle qui n'est pas prise en compte. Cette lacune est principalement attribuable à un manque de méthodes et de concepts applicables à la quantification des caractéristiques, autres que granulométriques, des graviers fluviaux.

Ce projet de recherche a pour objectif général d'améliorer les connaissances quantitatives de la structure du substrat graveleux des lits des rivières à saumons. Plus précisément, cette recherche a pour objectif de développer un modèle prédictif de la disponibilité d'habitat fondé sur une caractérisation quantitative qui tient compte de la structure et de la granulométrie du substrat. Pour arriver à cette fin, de nouvelles méthodes et concepts de quantification de l'agencement des graviers ont été développés. Une nouvelle méthode de photogrammétrie digitale plus accessible a été mise au point pour caractériser la microtopographie des lits de gravier. Cette méthode a permis de modéliser la topographie des sites d'études avec des Modèles Numériques de Terrain (MNT) ayant une résolution au sol de 1mm² et une précision de ±2-8mm. Les MNT ont été utilisés pour développer une nouvelle mesure de la rugosité des surfaces. Cette mesure, le R_{84}, quantifie la rugosité d'une surface en utilisant le 84ième percentile de la distribution des différences d'élévations sur la surface et ce pour une distance horizontale choisie. Ensuite, les MNT ont été appliqués pour quantifier le niveau d'organisation des agencements de graviers. Une nouvelle

méthode a été mise au point en appliquant des principes de vision numérique et de traitement d'images pour évaluer la dimension fractale des surfaces avec l'information topographique des MNT. Afin de compléter ces informations avec une description plus explicite de l'agencement des particules des graviers, une nouvelle méthode de quantification de la structure des lits de graviers a été mise au point. Cette méthode, qui emploie elle aussi des outils de vision numérique et de traitement d'images, s'appuie sur deux nouvelles variables: Le chevauchement des particules voisines et le pourcentage de sable en surface, pour quantifier des phénomènes connus tels que l'imbrication et l'enchâssement. Cette méthode permet de quantifier des structures de graviers qui auparavant étaient décrites de façon qualitative. Les méthodes précédentes ont été appliquées afin de quantifier de façon très détaillée des surfaces de graviers où les interstices avaient été recensés et mesurés. L'utilisation de la régression logistique a permis d'établir le premier modèle prédictif de la présence d'interstices sur une surface de graviers. De plus ce modèle a permis d'établir les variables importantes pour la disponibilité d'interstices. Alors qu'il est généralement admis que les interstices sont associés au substrat grossier, nos résultats montrent que la taille des particules est nécessaire mais non-suffisante pour prédire adéquatement la disponibilité d'interstices. Le modèle de prédiction des interstices le plus parcimonieux et performant est fonction de la taille des particules, de la rugosité de la surface et du pourcentage de sable en surface. Les résultats de la thèse suggèrent que les effets de structure des lits de graviers doivent être incorporés dans les méthodes d'évaluation de l'habitat hivernal disponible pour le saumon juvénile.

TABLE DES MATIÈRES

CHAPITRE 6: NEW METHODS FOR THE QUANTITATIVE ANALYSIS OF STREAM GRAVEL BED SURFACE STRUCTURE

Liste des figures

Liste des tableaux

Chapitre 1 : Introduction

La gestion des stocks de saumon atlantique est une problématique d'importance au Québec. Face à une diminution constante des stocks mondiaux (Parrish *et al.* 1998), les gestionnaires de rivières sont placés devant le défi d'équilibrer conservation de la ressource et pêche sportive. Cette gestion des stocks nécessite une connaissance de la capacité de production d'une rivière qui s'évalue à partir des facteurs biotiques et abiotiques qui gouvernent l'habitat du saumon. Actuellement, les facteurs abiotiques tels que la vitesse de courant, la profondeur de la rivière et la qualité du substrat ainsi que les facteurs biotiques tels que la disponibilité de nutriments sont souvent évalués en période estivale. Les interventions conçues à partir de ces connaissances ont donc pour principale lacune de négliger les conditions nécessaires à la survie hivernale.

Plusieurs recherches sur le comportement hivernal ont pourtant mis en évidence une différence importante entre le comportement hivernal et estival des saumons juvéniles (Rimmer *et al.* 1983, Cunjak 1988, Griffith et Smith 1993, Mäki-Petäys *et al.* 1997, Vladimarsson et Metcalf 1998). Durant l'été, les saumons juvéniles se maintiennent en place dans le courant au-dessus d'une roche mère («home stone») et ils s'alimentent en saisissant des insectes en dérive. Cependant, ce comportement change lors de la transition automne-hiver. Lorsque la température de l'eau tombe sous une certaine température seuil, les juvéniles adoptent un comportement nocturne. La température critique semble varier légèrement selon la population et/ou la géographie, mais en général, la transition se fait à des températures entre 8 et 10 °C (Rimmer *et al.* 1983, Riehle et Griffith 1995, Cunjak *et al.* 1998). Suite à cette transition, les juvéniles deviennent inactifs durant le jour alors qu'ils s'enfouissent dans les interstices du substrat. Durant la nuit, les saumons juvéniles émergent du substrat et sélectionnent les zones d'écoulement à vitesses faibles. La figure 1.1, tirée de Rimmer *et al.* (1983) montre la taille des gravillons sélectionnés en période estivale (en jaune) et en période hivernale (en bleu). On peut y voir le changement dans la

sélection du substrat reflétant la transition de comportement. L'enfouissement dans les interstices du substrat durant le jour offre aussi un abri contre les prédateurs endothermiques diurnes (Vladimarsson et Metcalf 1998). L'émergence de nuit donne l'occasion pour une alimentation minimale (Cunjak 1988, 1996, Metcalf et Thorpe 1992, Cunjak 1996, Fraser et Metcalf 1997, Whalen *et al.* 1999) et permet d'échapper aux changements rapides des conditions d'écoulement ou d'englacement qui surviennent souvent au cours de la nuit durant l'hiver (Cunjak et Randall 1993).

Mason (1976) a rapporté que l'échec d'un programme d'ensemencement était en partie attribuable au fait qu'aucune attention n'avais été portée à la disponibilité d'habitat physique hivernal adéquat caractérisé par une quantité suffisante d'habitat interstitiel dans le substrat. La caractérisation de l'habitat interstitiel est actuellement difficile en raison d'un manque de méthodes appropriées. Conséquemment, plusieurs travaux s'intéressant à l'habitat interstitiel du saumon juvénile (Cunjak 1996, Heggenes 1996, Mäki-Petäys *et al.* 1997) assument que la présence de substrat grossier lessivé de particules fines est un indicateur fiable de la présence d'interstices. Par contre, Meyer et Griffith (1997) ont démontré que pour une granulométrie donnée, les truites juvéniles avaient une préférence pour les agencements où la distance entre les particules était plus grande. La caractérisation seule de la granulométrie des roches qui composent le substrat semble donc insuffisante, ce qui implique que l'agencement spatial des particules doit être considéré.

Les travaux de cette thèse tentent donc de combler les lacunes méthodologiques et conceptuelles concernant la caractérisation physique des graviers fluviaux. La thèse a aussi pour objectif de mettre au point un modèle prédictif de la disponibilité de l'habitat interstitiel. Cette thèse par article commence par une revue des notions de bases de géomorphologie, de photogrammétrie et de traitement d'images numériques utilisées dans la recherche. Le chapitre 3

présente ensuite la synthèse des articles de la thèse, discute de la contribution de chaque article et, illustre les liens entre les articles. Les quatre chapitres suivants présentent les quatre articles scientifiques rédigés, en anglais, dans le cadre des recherches de cette thèse. La thèse se termine par une brève conclusion qui discute des perspectives d'application et d'avenir de cette recherche.
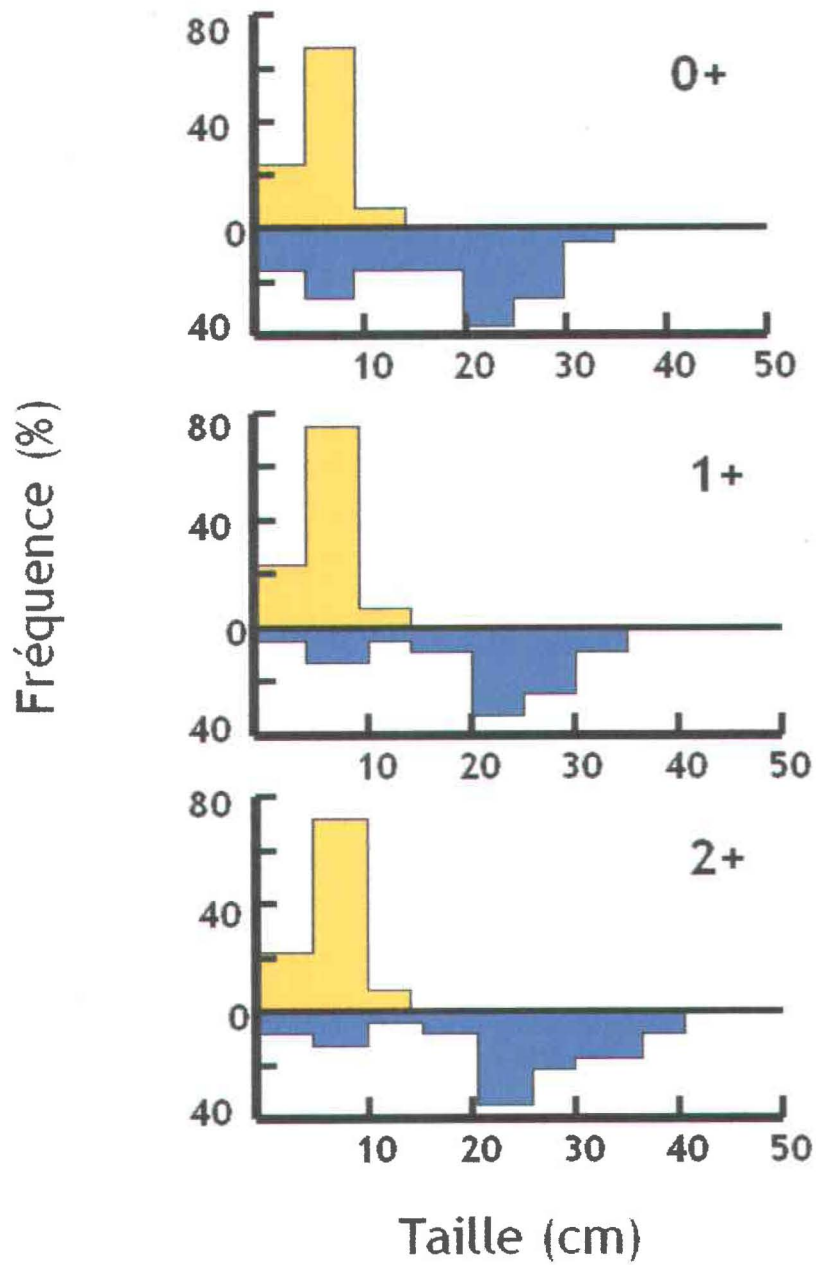
Figure 1.1. Sélection d'habitat de saumons juvéniles. Modifiée de Rimmer *et al.* (1983).

Chapitre 2: Revue des notions pertinentes

Ce chapitre présente une revue des notions de géomorphologie, de photogrammétrie et de traitement d'images qui sont appliquées dans les articles des chapitres 4 à 7.

2.1 Caractéristiques physiques des assemblages de graviers

2.1.1 Échelle des particules

Il est généralement admis que la morphologie des graviers fluviaux peut adéquatement être caractérisée par un ellipsoïde triaxial symétrique (Lord Rayleigh 1942, Koster *et al.* 1980, Janoo 1998). Sur cet ellipsoïde, on définit par convention l'axe long comme étant l'axe A, l'axe moyen comme étant l'axe B et l'axe court comme étant l'axe C.

2.1.2 Échelle d'un assemblage de graviers fluviaux

Church *et al.* (1987) distinguent quatre types de structure de lits de graviers fluviaux. Tout d'abord, comme le montre la figure 2.1a, on distingue les graviers en armature ('framework'). Il s'agit d'un agencement de cailloux grossiers en contact tangentiel où les vides sont partiellement remplis par des particules plus fines. Les graviers censurés (Figure 2.1b), présentent aussi une structure en contact tangentiel mais où la couche supérieure du substrat a été lessivée de ses particules fines par l'écoulement. Les graviers remplis (Figure 2.1c) sont à l'opposé des graviers censurés. Ils ont une structure de contact tangentiel, mais c'est ici la sous-surface qui est libre de fines, les interstices de la couche supérieure étant bouchés par une déposition de fines. Si la quantité de fines est importante, tel qu'illustré dans la figure 2.1d, les cailloux grossiers sont supportés par cette matrice de fines plutôt que par le contact tangentiel.

On peut remarquer l'importance de l'effet de colmatage des interstices par les particules fines. En présence d'une quantité importante de particules fines, on

observe en général la présence de l'enchâssement des particules grossières. Bunte et Abt (2001) définissent l'enchâssement (embeddedness) comme un enfouissement partiel des particules grossières par des particules plus fines. Les interstices normalement associés aux particules grossières seront donc colmatés si celles-ci sont recouvertes de particules fines. Une autre structure de graviers importante est l'imbrication des particules grossières (Church *et al.* 1987, Jain 1990, Robert 1991a, Chin *et al.* 1994, Powell 1998, Bunte et Abt 2001). Bunte et Abt définissent cette structure comme étant un agencement de roches en bardeaux où les particules du côté amont reposent sur les particules du côté aval. L'axe C des particules est en général parallèle à l'écoulement et le plan A-B des particules est face à l'amont. Il est logique de penser que l'imbrication plus ou moins grande des particules réduit la quantité et la taille des interstices en surface et, par conséquent, qu'elle réduit la disponibilité d'habitat. Cette hypothèse est supportée par les résultats de Meyer et Griffith (1997) qui ont montré qu'une augmentation de la distance séparant les particules d'un substrat artificiel a comme conséquence une augmentation de la disponibilité d'habitat.

Les structures de graviers, telles que l'imbrication et l'enchâssement, voir l'exemple de la figure 2.2, influencent donc la disponibilité d'interstices pour ce substrat. Par contre l'évaluation quantitative de cette influence est actuellement limitée par un manque de méthodes quantitatives capables de mesurer la structure des graviers fluviaux. La prochaine section discute de concepts et méthodes capables de corriger cette situation et d'améliorer notre capacité à prédire la présence d'interstices dans un substrat donné.

2.2 Rugosité des surfaces de graviers

La rugosité d'une surface peut se définir comme étant le degré d'irrégularité topographique de celle-ci. Dans cette optique, la rugosité de la surface sera certainement une fonction de l'agencement des particules du lit. Il est intuitivement facile de concevoir que pour deux graviers ayant la même

distribution granulométrique, l'organisation des particules détermine la rugosité de la surface. Une étude plus approfondie de la rugosité pourrait donc approfondir notre compréhension des agencements de graviers et fournir un paramètre quantitatif décrivant l'organisation et l'agencement des particules des lits de graviers. Cependant, il n'existe pas de méthodes standardisées pour mesurer la rugosité d'un lit. Il est donc difficile d'inclure ce paramètre dans une étude quantitative.

L'étude de la rugosité des lits de graviers s'est presque exclusivement faite dans le contexte de l'hydraulique. Dans ce domaine, un des problèmes principaux est la détermination et la prédiction de la résistance à l'écoulement d'un cours d'eau. La rugosité du lit intervient dans la dissipation de l'énergie dans la couche limite de l'écoulement (Kironoto et Graaf 1994). En milieu graveleux, on évalue généralement la rugosité en utilisant une valeur de percentile de la distribution granulométrique, telle que le $84^{ième}$, noté D_{84} (Robert 1991a). L'hypothèse sous jacente à l'utilisation d'une fraction granulométrique pour estimer la rugosité est que cette rugosité sera corrélée à la granulométrie. L'effet de l'organisation des particules est donc négligé dans les méthodes actuelles d'évaluation de la rugosité. Par contre, certains chercheurs ont fait le lien entre l'organisation des lits de graviers et la rugosité. Les travaux plus récents de Bergeron (1998) et Robert(1988, 1991b) ont employé l'étude des propriétés auto-affines des lits de graviers pour tenir compte des effets d'organisation des particules. Ces travaux utilisent l'analyse des propriétés d'auto-affinité et des bandes fractales des surfaces pour distinguer les différentes échelles de rugosité présentes sur une surface. Le succès de cette approche suggère que les propriétés auto-affines ont un potentiel pour quantifier l'organisation des particules d'un lit de gravier.

2.3 Analyse fractale et auto-affinité des surfaces

Le fondement de la théorie des fractales (Mandelbrot 1982) est la propriété d'auto-similarité. L'auto-similarité est une propriété d'invariance sous transformations d'échelle. Ainsi, pour un système auto-similaire, au moins une propriété reste constante même s'il y a variation l'échelle à laquelle le système est examiné. Par exemple, si on regarde une photo aérienne d'une ligne côtière prise à une altitude de 1 km et qu'ensuite on regarde une autre photo de la même région prise à une altitude de 500 m, on remarquera que la forme irrégulière de la côte demeure semblable. L'auto-affinité est un cas spécifique de l'auto-similarité. Dans ce cas, l'auto-similarité de l'objet se fait selon une direction seulement. Étant donné que les quantités statistiques sont scalaires (*i.e.* sans direction), elles sont bien adaptées aux analyses d'auto-affinité. En géomorphologie, on évalue généralement les propriétés d'auto-affinité à l'aide du semi-variogramme (Robert 1988, Bergeron 1998). Le semi-variogramme est un graphe de la semi-variance d'une série en fonction de l'échelle spatiale. Donc, on cherche à déterminer si la semi-variance, une statistique de la distribution d'élévations topographiques, est invariante sous transformations d'échelle. La semi-variance γ d'une série est définie comme la moitié de la variance des incréments $[Z(x+h)-Z(x)]$ (Robert 1988):

$$2\gamma(h)=\mathrm{Var}\left[Z(x+h)-Z(x)\right] \qquad (2.1)$$

Si la distribution des différences d'élévations $[Z(x+h)-Z(x)]$ est gaussienne, on peut écrire que :

$$2\gamma(h)=E\left[Z(x+h)-Z(x)\right]^{2} \qquad (2.2)$$

où E est l'espérance mathématique (Stark et Woods 1994), Z est la variable d'intérêt et h est le pas des incréments. La semi-variance empirique d'une série est donnée par:

$$2\hat{\gamma}(h)=\frac{1}{N-h}\sum_{i=1}^{N-h}[Z(x_i+h)-Z(x_i)]^2 \qquad (2.3)$$

où N est le nombre d'observations. Dans le contexte d'une étude de la rugosité, la microtopographie est la variable étudiée. La figure 2.3 présente, sur échelle logarithmique, le semi-variogramme d'un profil microtopographique mesuré sur un lit de gravier. On peut y voir deux sections de droites.

Un tel semi-variogramme peut être modélisé par une loi de puissance de la forme:

$$F(x)\sim x^{-a} \qquad (2.4)$$

Lorsque l'on trace un semi-variogramme sur axes logarithmiques, a est la pente d'une section de droite. Avec les pentes obtenues à partir du semi-variogramme, il est possible de calculer la dimension fractale du profil microtopographique à condition que la distribution des différences d'élévation soit gaussienne. Pour les séries à une dimension, tels que les profils microtopographiques, la dimension fractale, D, se calcule selon (Robert 1988, Schroeder 1991)

$$D=2-a/2 \qquad (2.5)$$

Cette dimension fractale donne une mesure de la complexité de la série. Plus la dimension fractale est élevée, plus la série est complexe. Sur la figure 2.3, la section de gauche d'une dimension fractale de 1.55 montre l'auto similarité des cailloux individuels. La loi de puissance de la section de droite, de dimension fractionnaire 1.71, montre une autre auto similarité reliant des objets plus grand. Ces objets ont été identifiés comme étant des formes de lit tels que les amas de cailloux (Brayshaw 1984, Robert 1991b) et la séquence seuil-mouille (Bathurst 1982, Robert 1991a). Ces deux invariances sous échelle présente dans les rivières graveleuses sont donc associées à deux échelles de la rugosité du lit,

celle des grains et celle des formes du lit. Ce semi-variogramme montre que les grains ont une structure moins complexe que les formes.

Cette application du semi-variogramme pour étudier les propriétés d'auto-affinité des profils topographiques peut être adaptée aux surfaces. Dans ce cas, l'équation du calcul du semi-variogramme pour une surface est donnée par :

$$\gamma(p,q)=\frac{1}{2(N-|p|)(M-|q|)}\sum_{i=1+\frac{|p|-p}{2}}^{N-\frac{|p|+p}{2}}\sum_{j=1+\frac{|q|-q}{2}}^{M-\frac{|q|+q}{2}}[Z(i+p,j+q)-Z(i,j)]^2 \qquad (2.6)$$

où γ est la semi-variance, p et q sont les pas dans les directions x et y, respectivement, N et M donne le nombre de lignes et de colonnes de la matrice Z qui représente les données d'élévations de la surface. Le résultat est une surface de semi-variance.

La figure 2.4 montre un exemple d'un semi-variogramme en 2 dimensions. Pour analyser ce type de semi-variogramme, les méthodes développées dans le contexte des semi-variogrammes en 1 dimension sont applicables mais elles ne sont pas idéales. En général, des profils de semi-variance sont extraits de la surface de semi-variance et la dimension fractale des bandes linéaires peut ensuite se calculer selon l'équation :

$$D=3-a/2 \qquad (2.7)$$

La première difficulté se présente lors de l'identification des bandes linéaires, puisqu'il n'existe pas de méthodes pour déterminer la présence de bandes auto-affines de façon totalement objective. Ceci rend fastidieux l'analyse de toute l'information disponible dans une surface de semi-variance et en général seulement 4 ou 8 profils sont extraits de la surface. La deuxième difficulté concerne la représentation concise du volume important d'informations associées aux surfaces de semi-variance.

Avant même de corriger ces lacunes, l'utilisation des surfaces de semi-variance pour l'étude de l'organisation des particules dans les lits de graviers nécessitera les données topographiques appropriées. Il sera donc nécessaire d'obtenir des informations topographiques précises et de haute résolution spatiale décrivant les surfaces de graviers. La photogrammétrie digitale est une des méthodes les plus répandue pour obtenir de telles données topographiques.

2.4 Photogrammétrie digitale

La photogrammétrie digitale est un outil puissant de caractérisation de la microtopographie capable d'une haute précision et d'une haute résolution spatiale. Cet outil permet de recueillir les données nécessaires à l'évaluation de la complexité de la surface et, de plus, les images obtenues peuvent servir à d'autres analyses. Nous ferons ici une brève discussion des bases pratiques et théoriques de la photogrammétrie.

2.4.1 Théorie

La photogrammétrie est basée sur un cas spécial de projection en perspective (Gosh 1971, Wolf 1983, Atkinson 1996). Le système optique de la caméra projette les trois dimensions de l'image réelle sur la pellicule bidimensionnelle (Figure 2.5) (Lane *et al.* 1993). À l'aide de cette figure, il est possible de définir deux espaces distincts. Tout d'abord l'espace réel, qui est tridimensionnel, et l'espace de l'image qui est en 2 dimensions. Le point qui relie ces deux espaces est appelé le point de perspective. À ce point, les rayons lumineux convergent pour assurer la transformation d'un espace à l'autre. Dans la réalité, c'est le système optique de la caméra qui assure cette convergence. La distance focale de ce système détermine donc la distance normale entre le point de perspective et l'espace image.

Mathématiquement, la transformation entre l'espace image et l'espace réel peut s'écrire (Atkinson 1996):

$$\begin{bmatrix} x_a \\ y_a \\ -c \end{bmatrix} = \mu^{-1} \begin{bmatrix} r_{11} r_{12} r_{13} \\ r_{21} r_{22} r_{23} \\ r_{31} r_{32} r_{33} \end{bmatrix} \begin{bmatrix} X_A - X_O \\ Y_A - Y_O \\ Z_A - Z_O \end{bmatrix} \tag{2.8}$$

où x_a et y_a sont les coordonnées de l'objet dans l'espace image, c est la distance focale de la caméra, μ est la constante de proportionnalité, X_A, Y_A et Z_A, sont les coordonnées de l'objet dans l'espace objet, X_0, Y_0 et Z_0 sont les coordonnées de la caméra dans l'espace objet et les r_{ij} sont les composantes de la matrice de rotation tridimensionnelle (Kreyszig 1996, Carbonneau 1998). Si on développe cette équation matricielle on, peut obtenir des équations pour x_a et y_a:

$$x_a = \frac{-c[r_{11}(X_O - X_A) + r_{12}(Y_O - Y_A) + r_{13}(Z_O - Z_A)]}{[r_{31}(X_O - X_A) + r_{32}(Y_O - Y_A) + r_{33}(Z_O - Z_A)]} \tag{2.9}$$

$$y_a = \frac{-c[r_{21}(X_O - X_A) + r_{22}(Y_O - Y_A) + r_{23}(Z_O - Z_A)]}{[r_{31}(X_O - X_A) + r_{32}(Y_O - Y_A) + r_{33}(Z_O - Z_A)]} \tag{2.10}$$

Ces équations sont appelées les équations de colinéarité. La résolution analytique de ces équations pour un couplet d'images chevauchantes permet la restitution tridimensionnelle des objets photographiés. Cette résolution se fait en deux étapes, la résection et l'intersection (Wong 1980, Atkinson 1996). Durant la résection, on mesure sur une seule image la position dans l'espace image d'au moins trois points. La position des ces trois points dans l'espace réel doit être connue. On obtient alors six équations et six inconnus, les trois angles de la matrice de rotation r_{ij} et X_0, Y_0, Z_0. On répète ensuite la procédure pour l'autre image. Il est absolument essentiel que les trois points connus soient visibles sur les deux images. Le calcul de la position XYZ d'un objet dans l'espace réel peut maintenant se faire en mesurant les coordonnées images d'un même objet sur chaque photo. On obtient donc un système redondant de quatre équations pour les trois inconnus de position (Wolf 1983). Il est donc possible de calculer la

topographie d'un terrain avec un couplet stéréoscopique (i.e. deux photographies qui se chevauchent) et d'au moins trois points arpentés.

2.4.2 La caméra et sa calibration

Dans la section précédente, la caméra était représentée par un point dans l'espace où les rayons lumineux convergent. Cette caméra conceptuelle est dite «idéale» car les rayons ne subissent aucune distorsion en la traversant et la distance focale est exactement connue. Les caméras réelles ne sont pas idéales. En traversant le système optique de n'importe quelle caméra, les rayons lumineux subissent une distorsion optique plus ou moins grande et la distance focale exacte, précise au micron près, n'est jamais connue à priori pour un système de lentille. De plus, le point principal, défini comme l'intersection de l'axe de la caméra et du plan de la pellicule, n'est pas parfaitement au centre de la pellicule.

La distorsion des rayons lumineux et l'alignement imparfait de l'axe de la lentille induit de l'erreur dans les équations de colinéarité et leur compréhension est essentielle en photogrammétrie. On distingue deux types de distorsion optique, la distorsion radiale et la distorsion tangentielle (Atkinson 1996). La distorsion radiale est une aberration qui déplace les points dans l'espace image plus loin du centre de l'image par rapport à leur position idéale. Elle est causée par des imperfections du système optique et est présente dans tout les systèmes de lentilles. La distorsion tangentielle cause plutôt un déplacement horizontal ou vertical des points dans l'espace image. Elle est causé par un mauvais alignement du centre de l'image par rapport à l'axe optique de la caméra. Les effets de la distorsion tangentielle sont en général plus faibles que les effets de la distorsion radiale. En effet, la distorsion tangentiele peut se minimiser par un bon alignement de l'axe optique alors que la distorsion radiale est un défaut intrinsèque de tout système optique qui est beaucoup plus difficile a éliminer. Il est donc fréquent de négliger la distorsion tangentielle et nous allons donc nous

attarder à la distorsion radiale. La modélisation de la distorsion radiale, à des fins de corrections, se fait à l'aide d'une série de puissance impaire (Atkinson 1996):

$$\delta_r = K_1 r^3 + K_2 r^5 + K_3 r^7 + ... \qquad (2.11)$$

où δ_r est la distorsion radiale, K_i sont des constantes et r est la distance radiale au centre.

En pratique, pour calculer les coefficients K_i, on utilise encore les équations de colinéarité. En disposant de plusieurs points XYZ connus pour une image, il est possible de prévoir la position de ces points dans l'espace image et ainsi de calculer la distorsion radiale entre la position prévue et la position observée. Une régression par moindres carrées donnera ensuite les coefficients K_i. Simultanément, il est possible de considérer la distance focale et le point principal comme inconnus et de calculer sa valeur lors de la régression. On peut donc comprendre que la calibration de la distorsion radiale et de la distance focale nécessite plusieurs points XYZ connus. En pratique, cela implique que plusieurs points, des points dit «de contrôle», doivent être arpentés. Il est donc nécessaire d'effectuer une étape de calibration de la caméra où des photographies sont prises avec plusieurs points de contrôle. Pour ce faire, deux approches sont possibles : la calibration en laboratoire et la calibration *in situ* (Chandler 1999). Lors de la calibration en laboratoire, une image est prise d'une série de cibles intérieures dont la position est connue avec une très haute précision. La calibration *in situ* s'effectue sur le terrain au moment même de faire la levée photogrammétrique. Des cibles sont alors introduites dans le champ optique de la caméra et elles sont arpentées avec la plus grande précision possible. La calibration en laboratoire offre l'avantage d'un arpentage très précis des cibles dans un environnement contrôlé. Cependant, ceci implique que le système optique est stable et que les paramètres de distorsion, de distance focale et de

point principal ne varieront pas entre le moment de calibration et la prise des levées. La calibration *in situ* offre l'avantage de calibrer la caméra au moment où l'image est prise. Par contre, l'arpentage sur le terrain est en général moins précis que celui en laboratoire. Selon la caméra utilisée et la situation exacte, le photogrammétriste doit choisir la méthode de calibration appropriée lors de la planification des levées.

2.4.3 Qualité des levés photogrammétriques

La qualité des levés photogrammétriques peut s'évaluer selon 2 mesures : la précision et la justesse («accuracy» en anglais). La précision représente une variation aléatoire autour de la valeur exacte. La justesse représente un biais systématique par rapport à la valeur exacte. En génal, la précision est plus utilisée que la justesse en photogrammétrie. Par exemple, avec une calibration appropriée, il a été montré que, pour les cas où les différences d'élévations de la surface sont petites par rapport à la hauteur de la caméra, la précision des levés photogrammétrique est de l'ordre de la résolution des images. Il est donc possible d'estimer rapidement la précision d'une campagne de photogrammétrie selon la règle suivante :

$$\frac{p}{G} = \frac{f}{H} \tag{2.12}$$

où p est la résolution de l'image, G est la largeur d'image au sol, f est la longueur focale de la caméra et H est la hauteur de la caméra. Prenons deux exemples. Pour une caméra 35mm montée au sol à une hauteur de 1 m et couvrant une largeur au sol de 28 cm, l'erreur est d'environ 1 mm. Pour une caméra de focale 50mm aéroportée à une hauteur de 155 m avec une largeur au sol de 93 m, l'erreur est de 3 cm.

La photogrammétrie est donc un outil quantitatif puissant d'un grand intérêt pour la géomorphologie fluviale comme le montre le nombre croissant d'applications

de la photogrammétrie en géomorphologie (Welsh et Jordan 1983, Lane *et al.* 1993, 1994, 2000, Stojic *et al.* 1998, Butler *et al.* 1998, 2001a, 2001b).

2.5 Traitement d'images numériques

L'utilisation d'images à des fins de mesures quantitatives en science ne se limite pas à la photogrammétrie. Le développement du format numérique pour les images a entraîné le développement d'un nouveau champ d'expertise : le traitement d'images numériques. En format numérique on peut distinguer les images en noir et blanc et les images en couleurs. En noir et blanc, chaque pixel est associé à un seul niveau de gris. Le reproduction des images en couleur se fonde sur le fonctionnement du système visuel humain qui est doté de récepteurs sensible au rouge, au vert et au bleu. Il est donc possible de reproduire des images couleurs numériquement en combinant différentes intensités de ces trois couleurs primaires. Pour les images numériques, l'information nécessaire à l'imagerie couleur est organisée selon 3 bandes, 3 matrices distinctes, de couleurs, chaque pixel est associé à trois niveaux de gris représentant les 3 couleurs primaires: rouge, vert et bleu. Il est possible d'effectuer des mesures quantitatives sur les propriétés spectrales des pixels ou encore sur les propriétés géométriques de groupes de pixels. De plus, la définition de groupe de pixels par segmentation d'image peut se faire automatiquement, soit par des méthodes statistiques, soit par des méthodes qui s'apparentent à la vision artificielle. Dans le cadre de cette thèse, les méthodes de segmentation sont appliquées pour identifier des gravillons et pour quantifier le pourcentage de sable sur une surface de gravier.

2.5.1 Segmentation en groupes de pixels

Rappelons qu'une image digitale est simplement une matrice de valeurs de ton de gris. En général, on utilise encore aujourd'hui 256 (0-255) niveaux de gris allant du noir au blanc. Il n'existe donc *a priori* aucun lien entre les pixels voisins d'une image numérique. Par contre, dans les applications du traitement d'images

numériques aux sciences de la terre, il est généralement nécessaire de distinguer des objets tels que des forêts en milieu urbain ou des zones de sables parmi des graviers. Il est donc nécessaire de définir des groupes de pixels ayant une propriété commune. De préférence, ce processus doit être pleinement automatisé. Nous discuterons ici de trois approches possibles qui ont été employé dans cette thèse : l'approche par seuillage, l'approche par opérateur de convolution et l'approche par texture.

2.5.1.1 Segmentation par seuillage

Prenons par exemple une image de grains de riz (MathWorks 2001) (figure 2.6). Il est facile de noter que la couleur de chaque grain de riz est similaire et que la couleur du fond de l'image est relativement uniforme. Si nous traçons un simple histogramme des tons de gris de l'image, on obtient la figure 2.7. Il est clair que deux modes existent. Le premier mode correspond au fond de l'image et le second correspond aux grains. Avec cet histogramme, nous pouvons donc établir un seuil capable de différencier les grains et le fond. Il existe un grand nombre de méthodes pour parvenir à cette fin mais elles ont toutes pour objectif de définir le seuil de partition entre les deux classes de l'histogramme. La méthode la plus simple consiste à établir le seuil à mi-chemin entre les maximums des deux modes de l'histogramme (Castleman 1996). Cependant, si l'histogramme n'est pas nettement bi-modal, cette méthode peut être inefficace. D'autres méthodes ont donc été développées pour faire le seuillage des histogrammes de forme plus complexe. La Méthode de Otsu (1979) établi le seuil avec les deux premiers moments de l'histogramme. Cette méthode procède en minimisant la variance entre les deux classes de l'image obtenues après le seuillage. Une fois le seuil calculé, il est possible de produire une image binaire (figure 2.8). Dans cette nouvelle image, les pixels dont la valeur est au-dessus du seuil dans l'image originale ont la valeur de 1. Il est à noter que la méthode de segmentation par seuillage est très fréquemment employée suite à des manipulations de l'image visant à mettre en évidence certains aspects de celle-ci.

Par exemple, les deux autres méthodes de segmentation décrites dans cette section feront appel à cette technique pour distinguer les groupes dans des images transformés.

L'image binaire obtenue après le seuillage de l'image de grains de riz peut donc servir à la création de groupes correspondant aux grains individuels. Il s'agit de distinguer chaque grain individuel. La création de groupes se fait à partir de critères dits de «connectivité». On définit un groupe de pixels comme étant 4-connecté si tous les pixels du groupe sont en contact via les arrêtes des pixels (figure 2.9). De plus, on définit un groupe de pixels comme étant 8-connecté si les pixels sont en contact via les arrêtes ou les coins des pixels. Un ensemble de pixels 4-connecté est donc 8-connecté mais l'inverse est faux. À partir de ces critères il est donc possible de construire un algorithme qui parcours l'image pour définir les groupes. L'information est généralement représentée sous forme d'une troisième image en fausses couleurs (figure 2.10) ou la matrice d'image est constituée des numéros d'objet. Une telle image peut ensuite être employée pour faire des mesures de la géométrie des objets. Par exemple, la surface de chaque grain individuel, sa largeur et sa longueur.

2.5.1.2 Segmentation par opérateurs de convolution

Dans l'exemple précédent, l'image était constituée d'un groupe d'objets de couleur uniforme sur un fond uniforme. Puisque la segmentation par seuillage utilise uniquement l'information de l'histogramme, on considère seulement les niveaux de gris des pixels sans tenir compte de leur position dans l'image. Une approche alternative peut s'élaborer en considérant les propriétés de l'image de façon plus locale. Par exemple, au lieu d'établir un seuil pour distinguer tous les grains de riz de l'ensemble du fond, il est possible de rechercher des contrastes locaux de couleurs pour trouver les endroits de l'image ou la frontière d'un grain de riz est en contact avec le fond de l'image. C'est le fondement de la détection

des discontinuités («edge detection» en anglais) (Castleman 1996, Richards et Jia 1999).

La détection de discontinuités a plusieurs applications mais nous la considérons ici seulement dans l'optique de définition de groupes de pixels. Il s'agit donc de trouver un groupe de pixel dont la couleur contraste avec le fond de l'image de façon local. Ceci se fait par opérateur de convolution. L'opérateur de Sobel est le plus communément appliqué (Castleman 1996, Richards 1999).

L'opérateur de Sobel est constitué de deux kernels matriciels, tels qu'illustré à la figure 2.11. Le premier kernel détecte les discontinuités à tendance horizontale alors que le second détecte les discontinuités verticales. La méthode de Sobel procède donc en convoluant l'image avec chaque kernel et prend ensuite le résultat maximal pour produire une image de discontinuité. La figure 2.12a montre l'image de riz traité par la méthode de Sobel. On peut voir que les contours des grains ont été mis en évidence. Il y aura donc un nouveau mode dans l'histogramme à la valeur 255 qui permettra de segmentater les contours de valeur 255 et le reste de l'image dont le mode est a environ 70 (Figure 2.12b).

Une fois les contours de l'objet détecté, la méthode de seuillage peut être appliquée pour obtenir une image binaire des contours à laquelle peut s'appliquer des algorithmes de remplissage afin de créer une image binaire qui sera groupé par méthode de connectivité. L'algorithme de remplissage est une méthode simple qui permet de remplir les trous dans les objets d'une image binaire. On commence tout d'abord par définir les trous. Ceux-ci sont définis comme étant les zones de l'image qui ne peuvent êtres atteints si on propage des pixels de valeurs 1 à partir des bords de l'image avec la condition que cette propagation s'arrête lorsqu'un pixel dont la valeur est déjà 1 est atteint. Les pixels associés aux trous sont ensuite mis à la valeur 1. La figure 2.13 illustre le fonctionnement de l'algorithme de remplissage.

La figure 2.14 montre le résultat de l'application du seuillage à la figure 2.12b suive de l'application de l'algorithme de remplissage. Les grains dont seulement les contours sont tracés illustrent la plus grande difficulté d'application de la segmentation par détection par des discontinuités. Il n'est pas rare que le kernel de sobel mettent en évidence trop faiblement une discontinuité soit totalement ou en partie. Par conséquent, lors du seuillage, il arrive que certains contours soient absents ou rompus. Alors, l'algorithme de remplissage donne des résultats imparfaits. Il est donc nécessaire d'ajuster le processus de seuillage pour chaque application afin d'améliorer les résultats.

Nous nous attardons ici pour considérer une classe particulière de groupes d'images : les groupes de forme rectiligne. Les opérateurs de convolution décrits plus haut peuvent être employés pour détecter les lignes dans une image. Le chapitre 5 repose sur une méthode automatisée de détection des sections rectilinéaires dans un profil de semi-variance. Cette méthode applique des opérateurs de convolution qui sont en fait une généralisation de l'opérateur de Sobel.

2.5.1.3 Segmentation par opérateurs de texture

L'image de grains de riz employée comme exemple est très simple. Les grains de riz sont de couleur uniforme sur un fond sombre uniforme. Si on compare avec une image numérique de graviers fluviaux (figure 2.15), il est clair que des méthodes plus avancées seront requises pour délimiter des groupes de pixels dans les images de graviers. Ce problème constitue une application typique de la segmentation par opérateurs de texture. Dans le cas des images, la texture peut se définir comme un attribut représentant l'agencement spatial des niveaux de gris des pixels dans une région (Castleman 1996, IEEE 1990). La texture peut donc se concevoir comme étant une quantification de l'aspect plus ou moins poivré d'une image. Pour quantifier la texture, la première étape est le calcul de la matrice de co-occurrence. La matrice de co-occurrence quantifie la texture

d'une image en comptant l'occurrence de pixels voisins de niveau de gris donnés. Le pixel de coordonnée i,j dans la matrice de co-occurrence **P** a comme valeur la fréquence normalisée qu'un pixel de niveau de gris i se trouve à coté d'un pixel de niveau de gris j. Ce calcul peut aussi se faire pour des distances de séparations des pixels variables. En général, on ré-échantillonne les images à un niveau de gris inférieur pour accélérer le calcul. La figure 2.16 montre un exemple d'image de graviers avec sable tiré du chapitre 5 et la matrice de co-occurrence qui lui est associée. L'image représente deux gravillons enchâssés dans le sable. La matrice de co-occurrence est présentée sous forme d'image avec la valeur de co-occurrence pour une entrée donnée de la matrice représentée en tons de gris. Pour faire le calcul de la matrice, l'image fut ré-échantillonnée à 32 niveaux de gris. On constate d'abord un point de haute fréquence au niveau de gris (32,32). Ceci signifie qu'une majorité de pixels de niveau de gris 32 sont voisins de pixels de niveau 32. En examinant l'image on voit que c'est la particule plus grossière de l'image qui est de couleur blanche uniforme qui est responsable de ce résultat. On constate aussi au centre de la matrice une tache diffuse causée par le sable où des niveaux de gris inégaux sont en contact. Cependant, on peut observer que la localisation spatiale de ces objets de l'image a été perdue dans le calcul de la matrice de co-occurrence.

Il est possible de quantifier la matrice de co-occurrence avec un seul nombre. Cette quantification s'effectue avec des mesures de textures. Ces mesures de texture quantifient la valeur des points et la forme de la matrice de co-occurrence. Nous discuterons ici des quatre principales mesures de textures :

L'inertie :

$$I = \sum_{i=0}^{L-1} \sum_{j=0}^{L-1} (i-j)^2 P_{ij} \qquad (2.12)$$

L'homogénéité :

$$L=\sum_{i=0}^{L-1}\sum_{j=0}^{L-1}\frac{1}{1+(i-j)^2}P_{ij}$$

(2.13)

L'énergie :

$$E=\sum_{i=0}^{L-1}\sum_{j=0}^{L-1}[P_{ij}]^2$$

(2.14)

L'entropie :

$$H=\sum_{i=0}^{L-1}\sum_{j=0}^{L-1}P_{ij}\log(P_{ij})$$

(2.15)

L'inertie et l'homogénéité sont des mesures qui quantifient la largeur de la matrice de co-occurrence par rapport à la diagonale principale. Dans le cas de l'inertie, le terme $(i-j)^2$ donne plus de poids aux valeurs de co-occurrence éloigné de la diagonale où $i=j$. Les images avec une forte inertie seront donc celles qui sont très irrégulières et où des pixels de niveau de gris très inégaux sont en contact. Dans le cas de l'homogénéité, ce sont les valeurs sur la diagonale qui ont le plus de poids. Donc, les images plus homogènes sont celles ou des pixels de niveau de gris similaires sont en contact.

Les mesures d'énergie et d'entropie tiennent seulement compte des valeurs des pixels dans la matrice de co-occurrence. L'énergie donne une mesure de la concentration de pixels de couleur uniforme. La mise à la puissance 2 dans l'équation 2.14 donne plus de poids aux fortes valeurs de co-occurrence. L'entropie est une mesure similaire mais plus sensible à cause du comportement du logarithme dans l'équation 16.

Il est possible de calculer une seule matrice de co-occurrence pour une image et ensuite d'évaluer une mesure de texture. Mais comme l'illustre la figure 2.16, la localisation spatiale des groupes d'objets d'une image est perdue si on calcule une seule matrice de co-occurrence. Donc, il est plus utile d'étudier les variations de textures à une échelle plus locale de l'image afin de conserver la localisation spatiale des objets dans l'image. Ainsi, les méthodes de segmentation par texture cartographient la variation d'une ou plusieurs mesures de textures sur une image donnée avec l'objectif de distinguer les objets dans l'image à partir de leurs propriétés texturales. On calcule d'abord la matrice de co-occurrence sur une fenêtre de l'image de petite dimension. On évalue ensuite les mesures de textures sur cette fenêtre. Finalement, on répète le processus pour une nouvelle position de la fenêtre et on analyse toute l'image de cette façon.

La figure 2.17 montre les cartes des quatre mesures de texture pour l'image de la figure 2.16a. Les cartes sont produites avec des fenêtres de dimension 20X20. La figure 2.17a montre la carte d'inertie. On y distingue bien le sable et la particule plus grossière. La particule grossière étant de couleur très uniforme, les pixels voisins sont de couleur uniforme et donc de faible valeur d'inertie. Dans le cas du sable, la forte variation spatiale de couleurs donne des plus fortes valeurs d'inertie. La petite particule est aussi visible. La figure 2.17b montre la carte d'homogénéité. Dans ce cas, le sable est peu homogène et les particules sont plus homogènes. Les figures 2.17c et 2.17d illustre bien la différence de sensibilité de l'énergie et d'entropie. En comparant la figure 2.17c avec l'image originale, on voit que la région très uniforme de la particule grossière domine la carte d'énergie. Par contre, dans le cas de l'entropie, il est possible de distinguer les particules et le sable. Dans le cas des figures 2.17 a,b et c l'application du seuillage donnera de bons résultats pour distinguer le sable et les gravillons (voir chapitre 5)

La segmentation par opérateurs de texture a donc la capacité de créer des groupes dans une image même si la distribution spatiale des niveaux de gris est très complexe. Comme démontré dans le chapitre 5, l'approche texturale peut différencier des objets dans des cas ou la seule application du seuillage échoue. C'est donc une approche qui a beaucoup de potentiel en sciences de la terre où les images sont en général très complexes.

2.5.2 Opérations morphologiques binaires

Les opérations morphologiques binaires sont fréquemment employées en traitement d'images pour corriger des imperfections mineures qui empêchent le bon fonctionnement d'un algorithme. Il est donc utile d'en discuter brièvement ici. Deux opérations fondamentales sont définies : l'érosion et la dilatation. Rappelons que ces opérateurs sont définis pour des images binaires. L'opérateur d'érosion fait passer la valeur des pixels aux frontières d'un objet de 1 à 0. La dilatation est l'opération inverse, elle fait passer les pixels immédiatement à l'extérieur de la frontière de 0 à 1. Les applications successives de l'érosion et de la dilation donnent lieu à d'autres opérateurs distincts. On définit l'opérateur d'ouverture comme étant l'application d'un opérateur d'érosion suivi de l'application d'un opérateur de dilation. À l'inverse, la fermeture est effectuée par l'application de la dilatation suivie de l'érosion. La figure 2.18 illustre les opérations morphologiques discutées ci-haut. La figure 2.18a montre l'application d'un opérateur d'ouverture pour séparer deux carrés liés par un pixel. On peut y voir l'effet des applications successives de l'érosion et de la dilatation. La figure 2.18b montre l'application d'un opérateur de fermeture à l'objet de la figure 2.18a. Il s'agit ici de fusionner les deux carrés. La figure 2.18 illustre l'utilisation des opérateurs morphologiques binaires pour diviser des objets liés par erreur ou pour fusionner des objets divisés par erreur. Les opérateurs morphologiques binaires sont donc appliqués après la binarisation d'une image et avant de grouper les pixels avec les critères de connectivité décrit plus haut. Par exemple, ils sont fréquemment employés avant l'application d'un algorithme de

remplissage pour fermer les contours d'objets rompus et s'assurer du bon fonctionnement de l'algorithme.
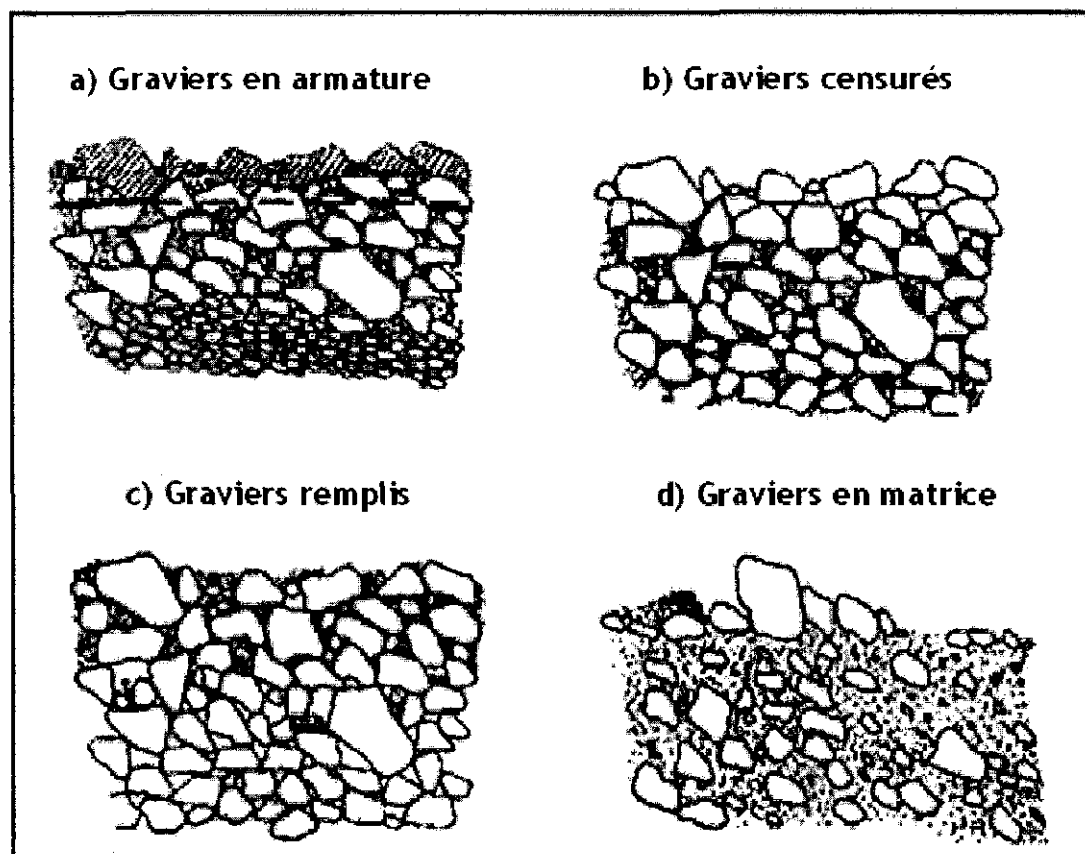
Figure 2.1. Classification des lits de graviers selon Church *et al.* (1987).
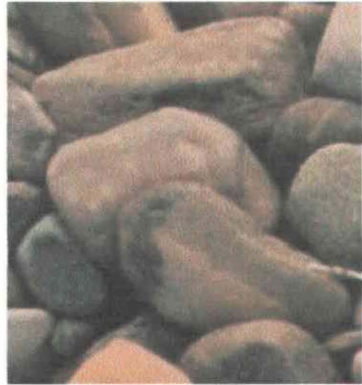
(a)   (b)

Figure 2.2. A) Exemple de gravillons imbriqués. B) Exemple d'un gravillon enchâssé.
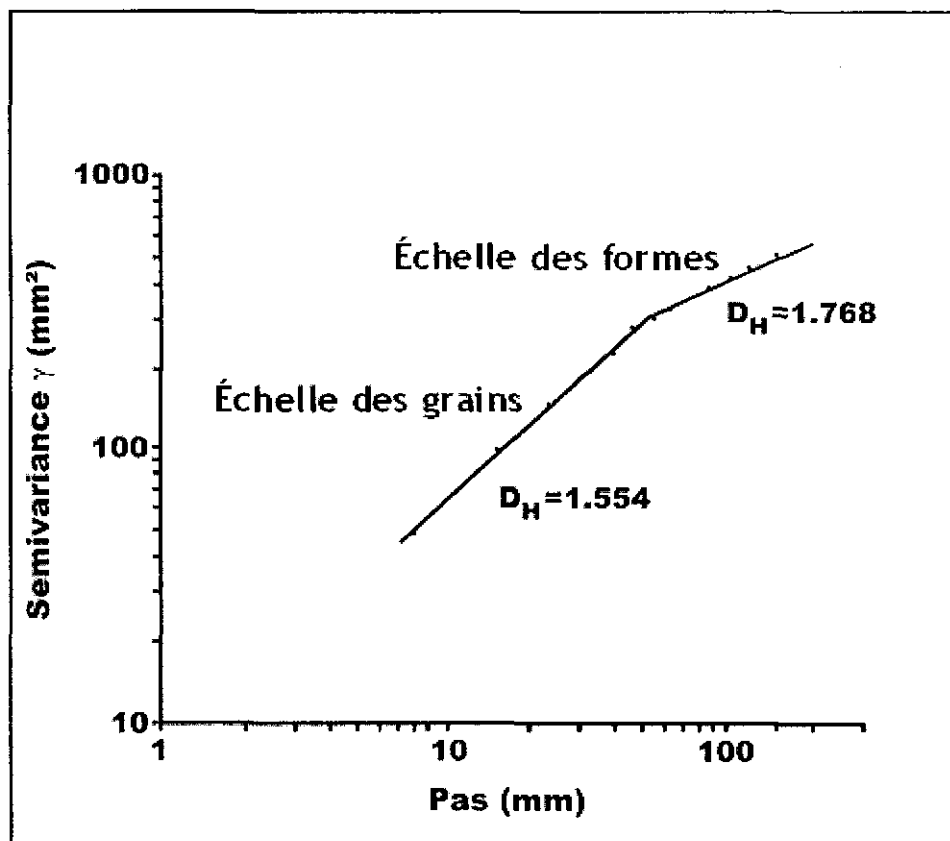
Figure 2.3. Exemple de profil de semi-variance. Tirée de Robert (1988).
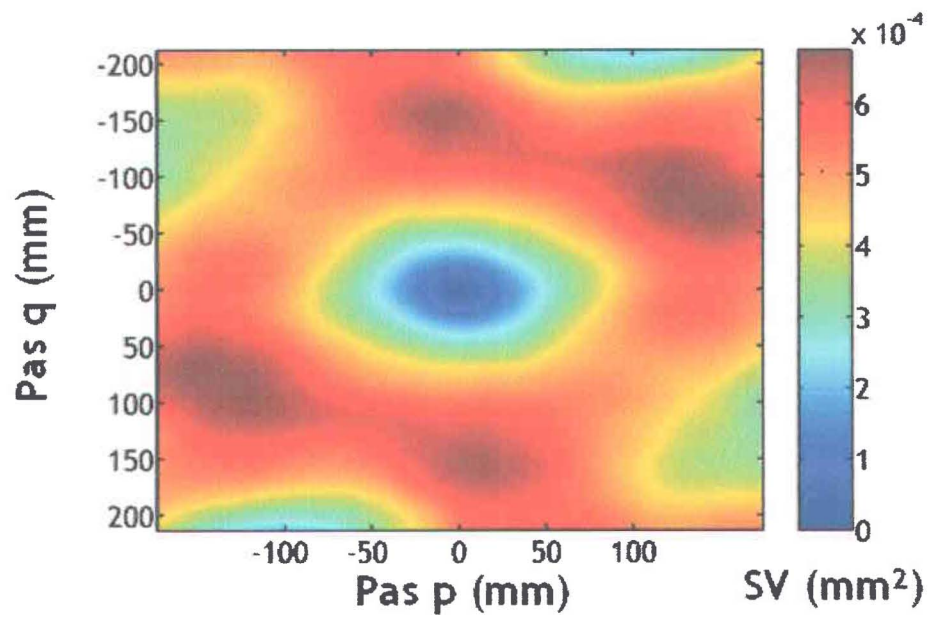
Figure 2.4. Exemple d'une surface de semi-variance.
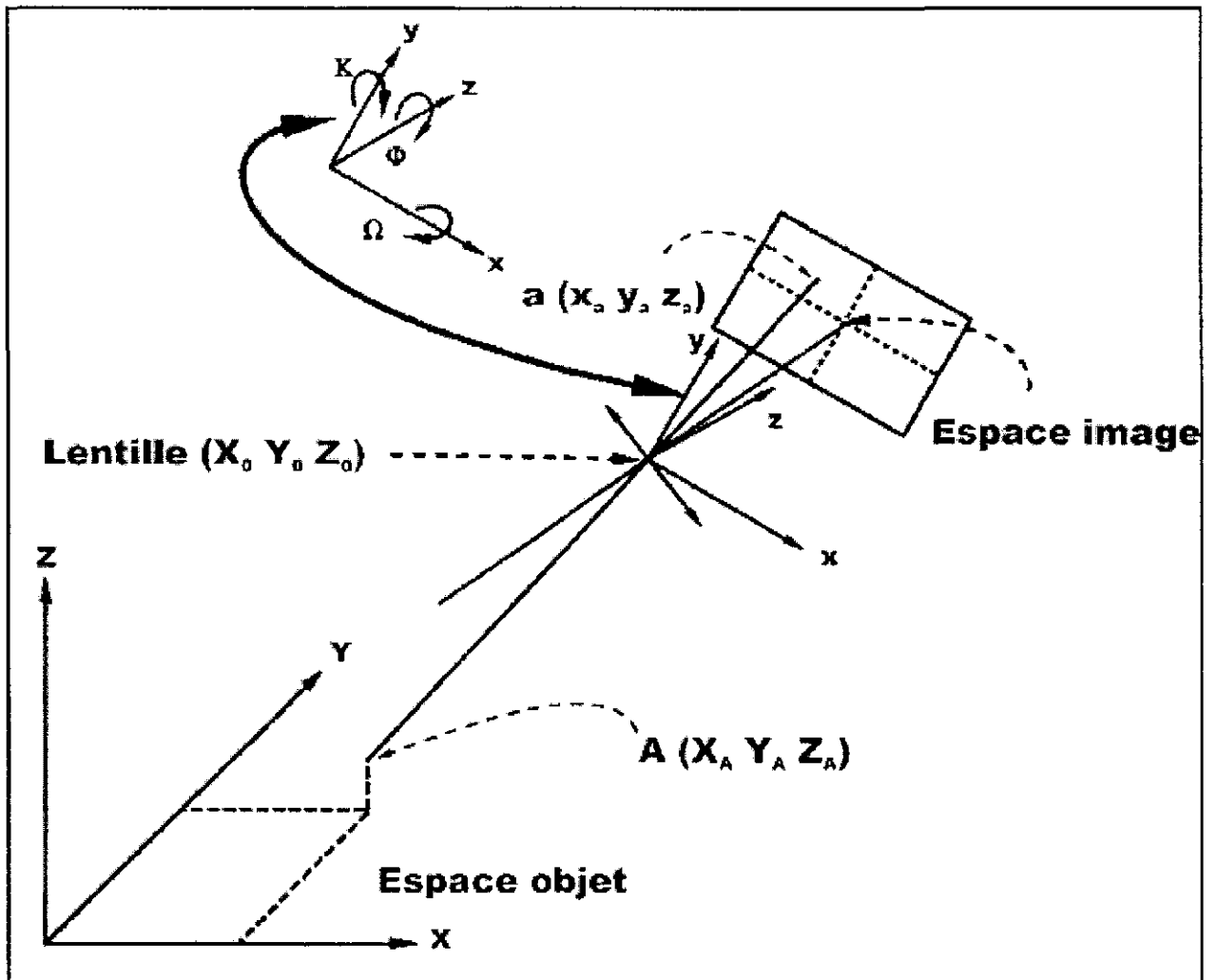
Figure 2.5. Schéma géométrique de la projection en perspective. Tirée de Lane *et al.* (1993).
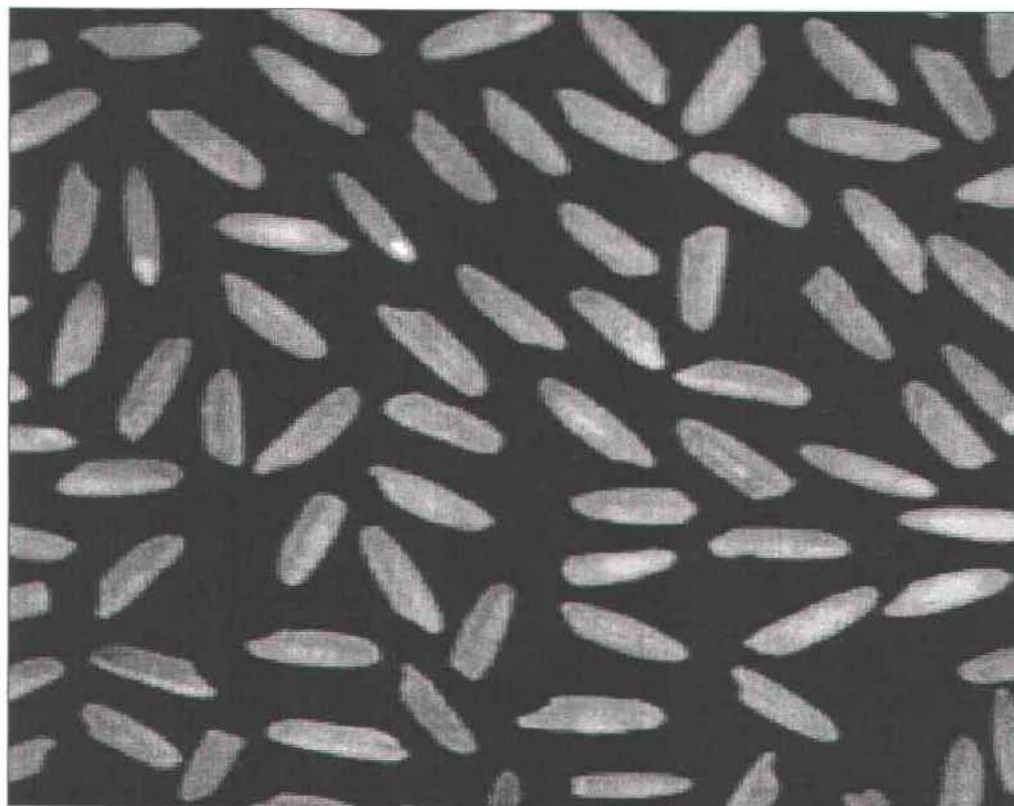
Figure 2.6. Image de grains de riz. Tirée de MathWorks (2001).
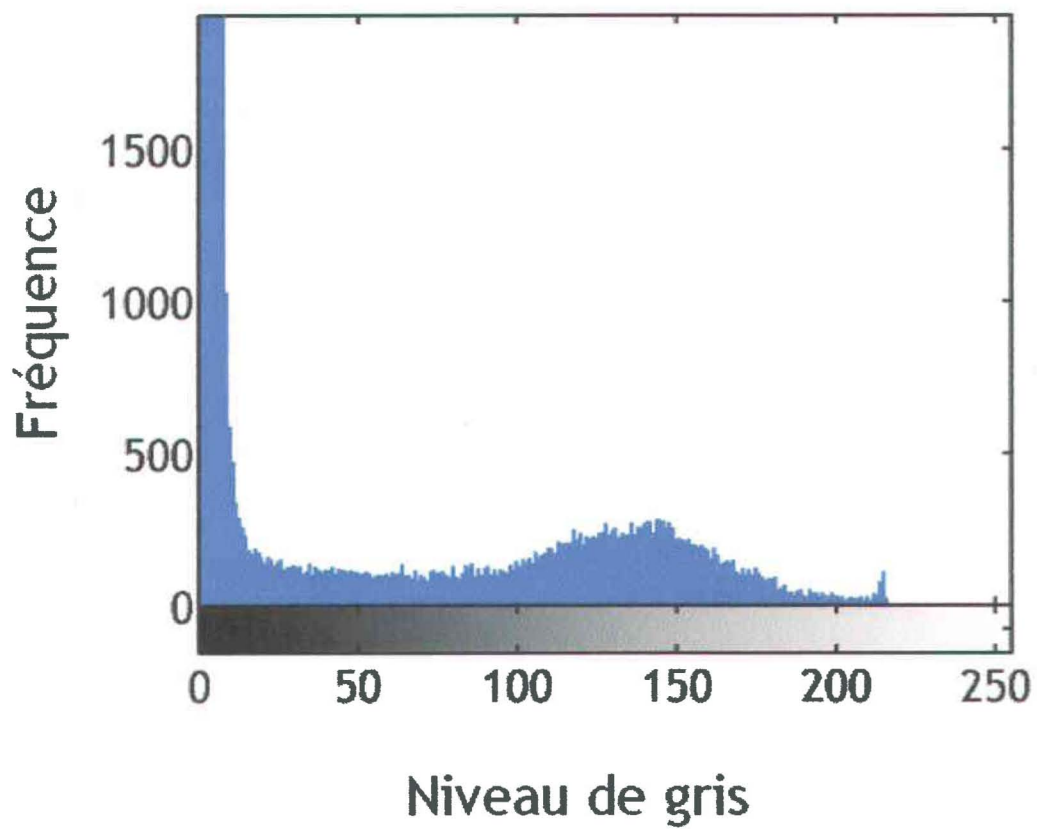
Figure 2.7. Histogramme des niveaux de gris de la figure 2.5.
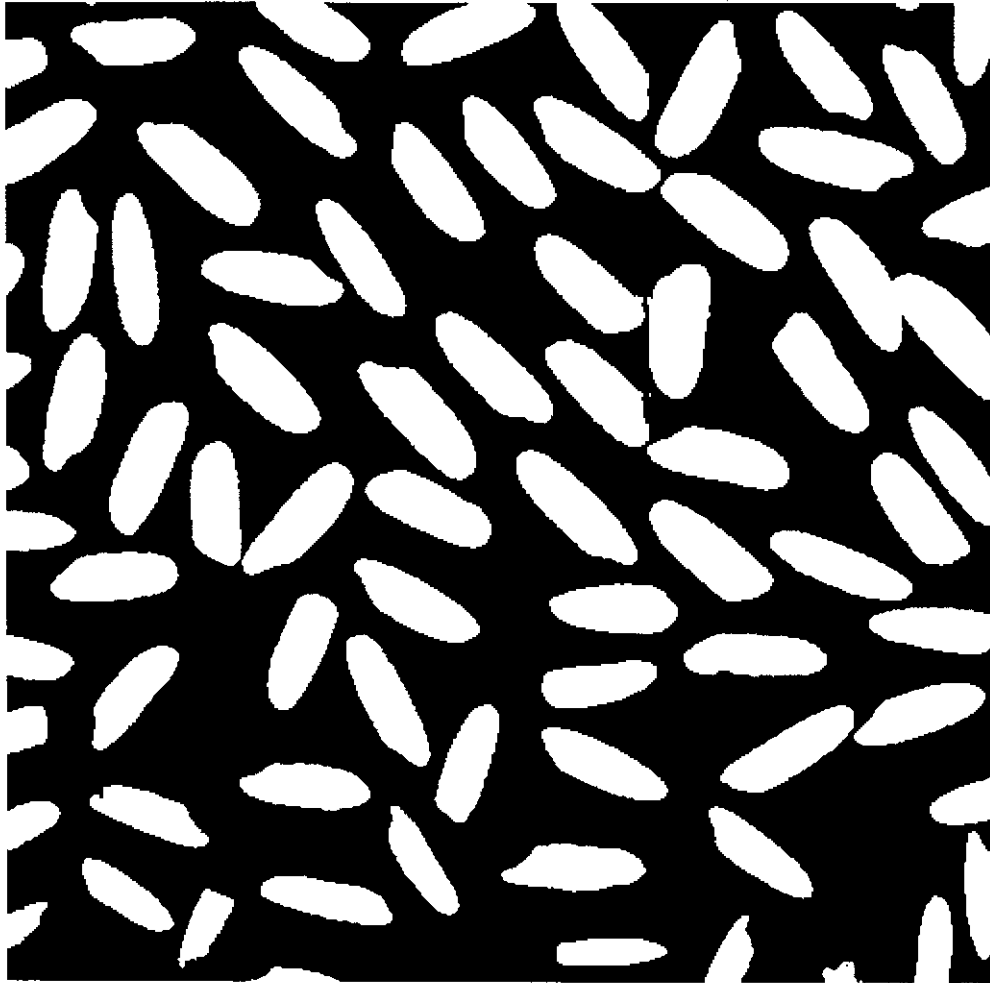
Figure 2.8. Image de riz binarisée.

(a)

(b)

Figure 2.9. Illustration des critères de connectivité. A) groupes de pixels 4-connectés. B) groupes de pixels 8-connectés.
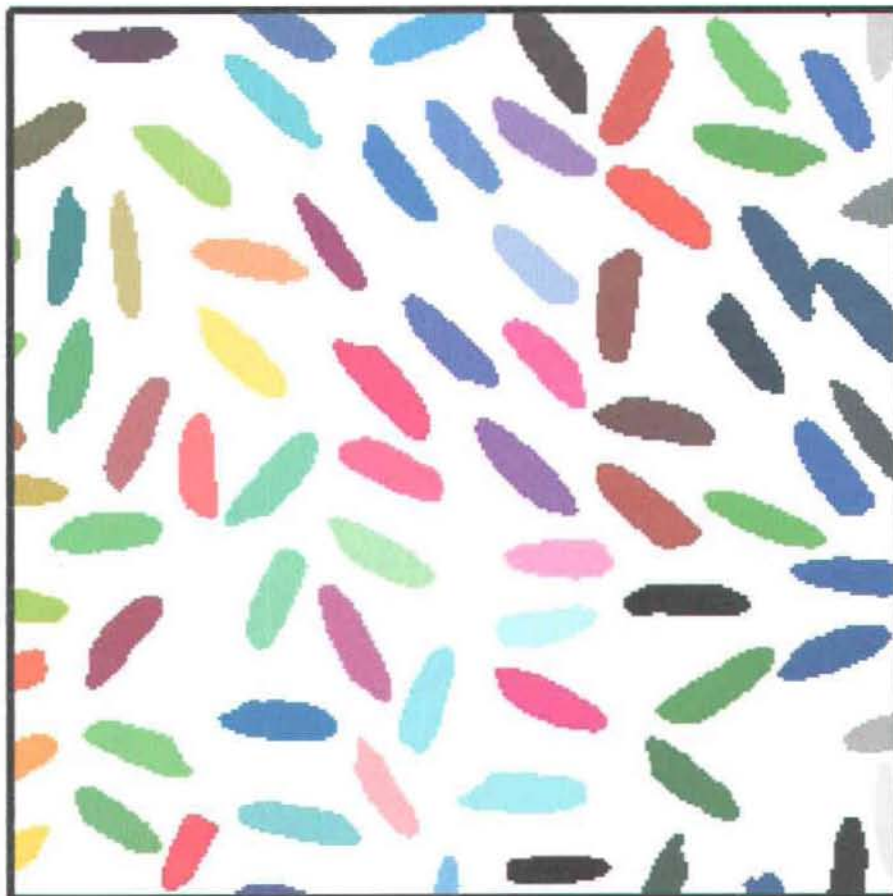
Figure 2.10. Image des groupes définissant les grains de riz individuels.

-1	-2	-1
0	0	0
1	2	1

-1	0	1
-2	0	2
-1	0	1

Figure 2.11. Opérateurs de Sobel pour la détection des discontinuités.

(a)
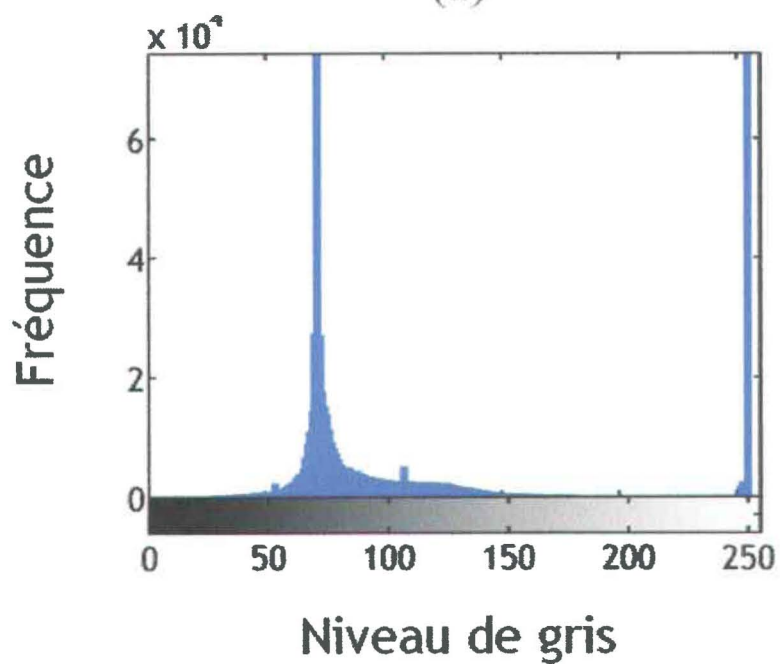
(b)

Figure 2.12. A) Image de grains de riz traitée par la méthode de Sobel. B) histogramme associé.
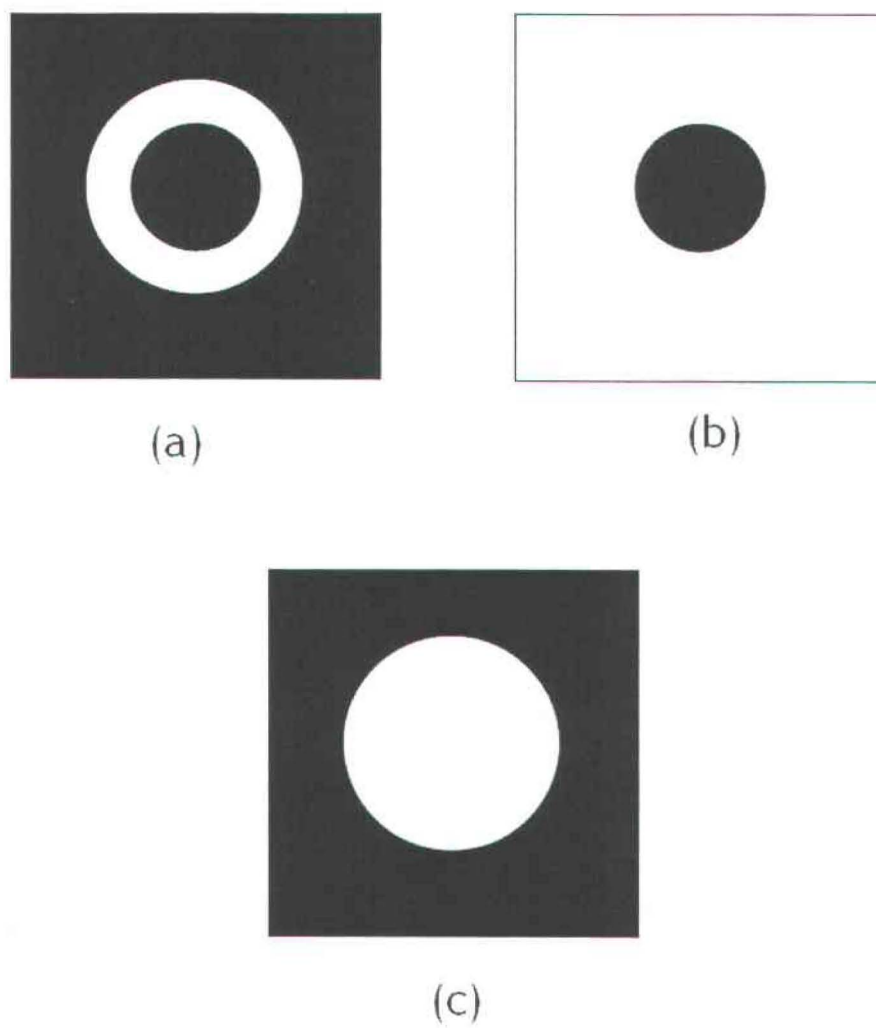
Figure 2.13. Algorithme de remplissage. A) Objet initial avec trou au centre.   B)
Résultat de la phase de propagation conditionnelle. C) Objet final sans trou.
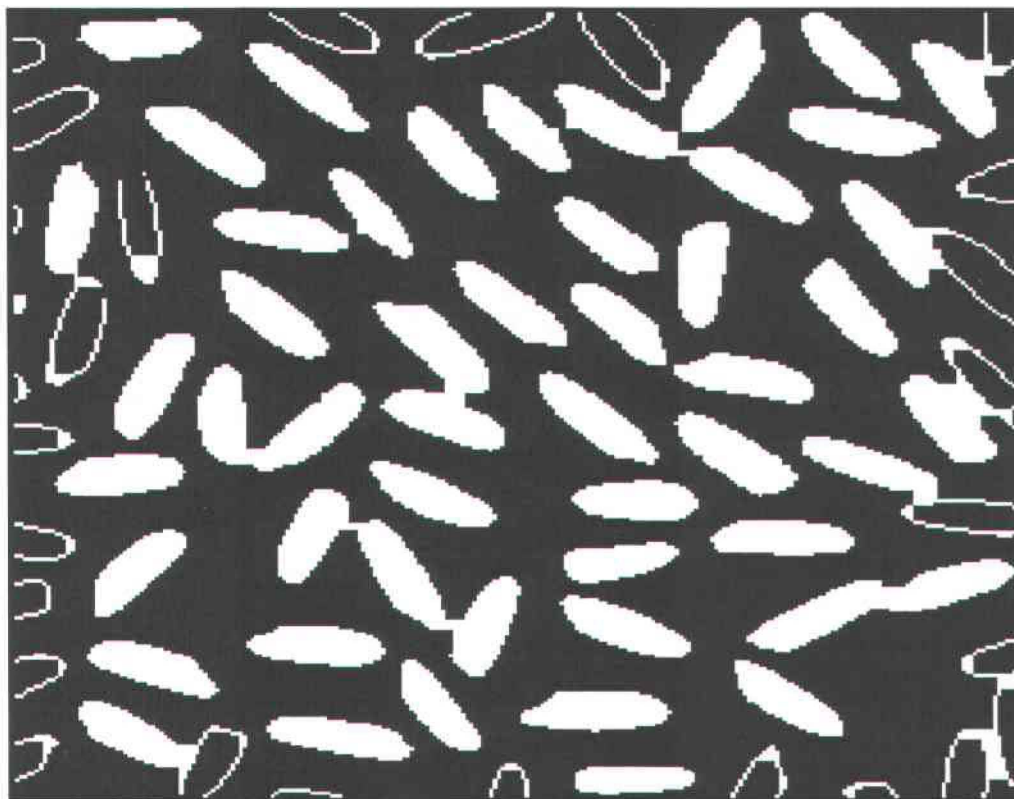
Figure 2.14. Image binarisée des grains de riz avec la méthode segmentation par détection des discontinuités.

Figure 2.15. Exemple d'image de graviers fluviaux.
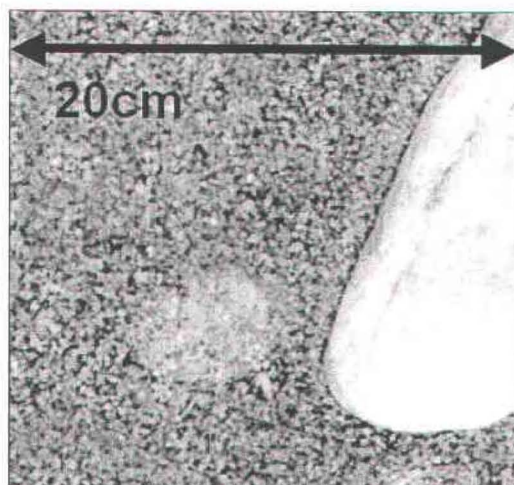
(a)
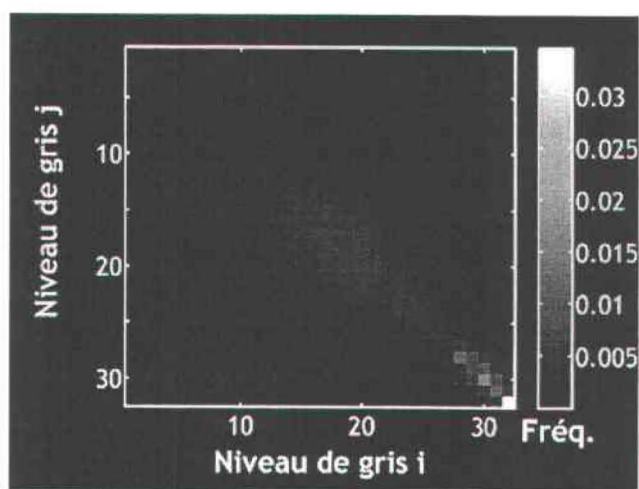
(b)

Figure 2.16. (A) Image de gravier avec sable et (B) matrice de co-occurrence associé.
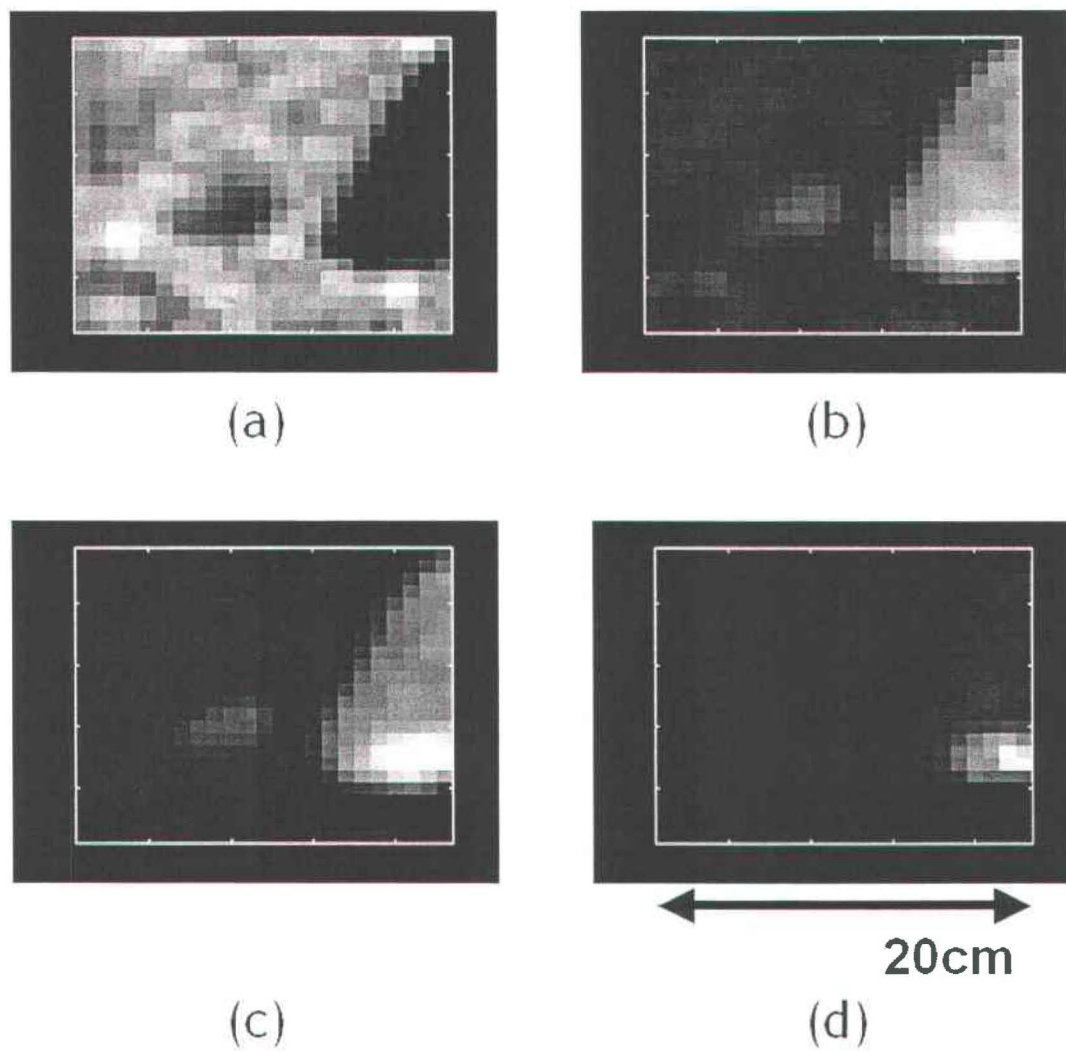
Figure 2.17. Cartes de propriétés texturales de l'image 2.16a. A) Carte d'inertie. B) Carte d'homogénéité. C) Carte d'entropie. D) carte d'énergie.
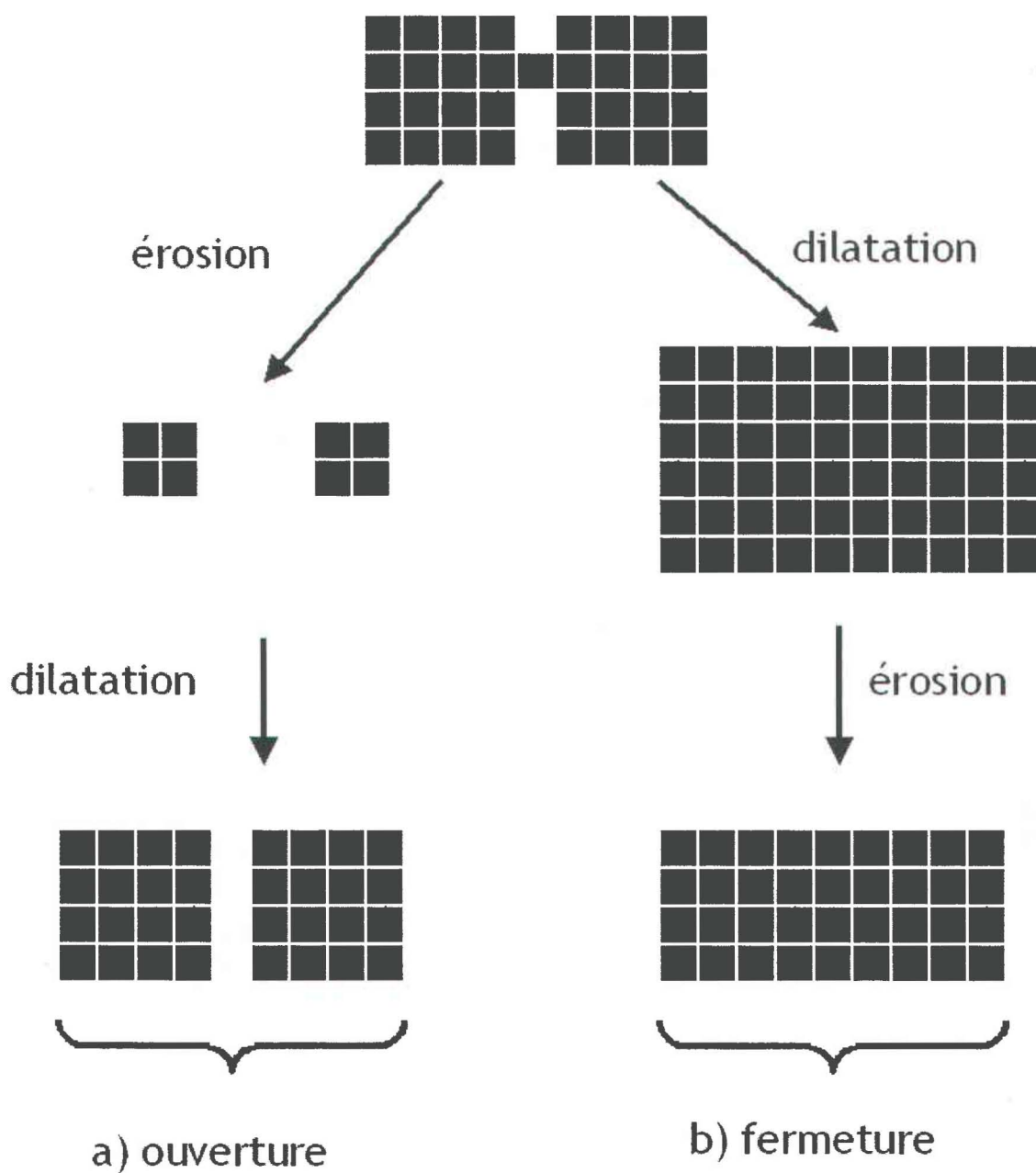
Figure 2.18. Illustration des opérations morphologiques binaires d'ouverture et de fermeture avec détail des effets de l'érosion et de la dilatation.

Chapitre 3 : Contributions de la thèse

Les quatre articles de la thèse ont comme auteurs le candidat, le directeur Normand Bergeron et le co-directeur Stuart Lane. La place du deuxième auteur est donnée au directeur ou au co-directeur selon le degré d'implication dans l'article en question. Toutefois, dans tous les cas, les deuxièmes et troisièmes auteurs ont accompli une tache de supervision normale et les travaux de recherche, de terrain, d'analyse et de rédaction sont en tous points la contribution du candidat.

Comme mentionné dans le chapitre précédent, l'incapacité actuelle à prévoir la disponibilité des interstices dans un substrat provient largement d'un manque de méthodes et de concepts applicables à la caractérisation des graviers fluviaux. Il a donc été nécessaire de déployer un effort de recherche important pour développer des méthodes et des concepts capables de décrire de façon quantitative les agencements de graviers fluviaux. Pour cette raison, les travaux et résultats des trois premiers articles sont en large partie des développements méthodologiques et conceptuels. Les travaux de recherche des trois premiers articles n'ont pas été faits seulement dans la perspective de l'habitat du saumon juvénile. Ces articles sont rédigés dans une optique d'application plus large que la modélisation de l'habitat du saumon. Finalement, Les méthodes et concepts développés dans les trois premiers articles ont été appliqué à la mise au point d'un modèle capable de prédire la présence d'interstices sur une surface de graviers. Ce modèle est discuté dans le quatrième article.

3.1 Contribution du chapitre 4

La photogrammétrie digitale automatisée, qui fut développé dans les années '90, est particulièrement intéressante pour la géomorphologie car elle offre la possibilité d'obtenir des Modèles Numériques de Terrain (MNT) de très haute densité et ce à très haute résolution spatiale. Butler *et al.* (1998, 2001a, 2001b) ont démontré que la photogrammétrie digitale est capable de caractériser la

structure et la rugosité des lits de graviers. Par contre, la méthode décrite par ces auteurs exige des investissements importants vers l'acquisition du matériel et des connaissances spécialisées. Il en résulte donc que cette méthode est sous-utilisée. La recherche du chapitre 4 avait pour objectif la mise au point d'une méthode de photogrammétrie plus accessible aux études de géomorphologie. Cet article démontre qu'il est possible d'effectuer des levées précises de photogrammétrie digitale avec une caméra 35mm commerciale et un numériseur commercial. L'utilisation d'équipements commerciaux moins dispendieux que les équipements spécialisés rend cette méthode plus accessible que celle décrite par Butler *et al.* (1998).

Ce chapitre se place aussi à l'avant garde sur une autre question, celle l'évaluation de la qualité des données. La pratique traditionnelle de la photogrammétrie exige que la qualité de chaque MNT soit vérifiée par des points de vérification indépendants. Par contre, avec les nouvelles méthodes de photogrammétrie digitale automatisée, le nombre de points des MNT augmente de 1 ou 2 ordres de grandeur. Il est donc devenu très difficile d'arpenter un nombre suffisant de points de vérifications. Par exemple, les MNT de cette thèse ont environ 160 000 points d'élévations. Si on fixe le nombre de points nécessaire à 1% du nombre de points dans le MNT, il faut donc 1600 points de vérification. C'est une tâche qui frôle le ridicule si on considère que la superficie totale du MNT est de 160 cm². De nouvelles méthodes d'étude de qualité des MNT sont donc requises. Une piste intéressante est l'application des propriétés d'auto-affinité des surfaces naturelles pour l'étude de qualité des MNT. Polidori *et al.* (1991) ont montré que l'application des propriétés d'auto-affinité permet d'identifier la présence d'anomalie dans un MNT. Ceci suggère qu'il soit possible d'utiliser les propriétés d'auto-affinité comme outil d'évaluation de qualité des MNT. Le chapitre 4 va dans ce sens en examinant l'effet des erreurs sur les propriétés d'auto-affinité d'un MNT. La démonstration que les propriétés d'auto-affinité sont en effet capables d'identifier un MNT avec d'importantes erreurs

pourra possiblement permettre d'établir les propriétés d'auto-affinité des surfaces naturelles. Ces propriétés pourraient ensuite servir au développement de méthodes automatisées de correction des MNT. Par contre, des recherches supplémentaires sont nécessaires pour bien comprendre l'effet des erreurs dans les MNT.

3.2 Contribution du chapitre 5

Les résultats du chapitre 5 sont en fait la suite logique de l'application des propriétés d'auto-affinité à l'étude de la qualité des MNT. Ces travaux ont mis en évidence les lacunes des méthodes actuelles pour calculer et représenter les propriétés d'auto-affinité des surfaces.

La première contribution de cet article réside dans une nouvelle approche pour identifier les bandes fractales auto-affine d'une surface topographique. La nouvelle approche requiert toujours le calcul du semi-variogramme en 2 dimensions, mais c'est dans l'analyse du semi-variogramme que cette méthode innove. Comme mentionné à la section 2.4, l'identification des bandes linéaires dans le semi-variogramme permet d'évaluer les propriétés d'auto-affinité des surfaces. Les méthodes statistiques d'identification de sections linéaires sont difficiles à appliquer ici car elles nécessitent une connaissance *a priori* du nombre de bandes fractales présente dans la surface, *i.e.* du nombre de bandes linéaires présentes dans un même profil de semi-variance. Pour cette raison, nous avons mis au point une méthode qui utilise la vision numérique pour identifier les segments linéaires. La méthode présentée applique des opérateurs de convolutions à des profils de semi-variance transformés en image pour chercher et identifier toutes les sections linéaires. Cette méthode s'inspire de la capacité du système visuel humain à identifier les lignes dans une image. Il s'agit d'une méthode automatisée qui ne requiert aucune connaissance *a priori* de la surface et qui est capable d'identifier les bandes fractales auto-affines d'une surface. L'algorithme est aussi capable d'établir l'absence de bande fractale pour une

surface donnée. Une fois l'identification faite, l'algorithme calcul la dimension fractale de chaque bande. Il s'agit de la première application de la vision numérique à l'analyse fractale des surfaces.

La seconde innovation de cet article se trouve dans la méthode de représentation des données obtenues. L'algorithme d'identification donne comme résultat une dimension fractale sur une étendue donnée et ce pour chaque direction sur la surface allant de 0 à 180° par incréments de 1°. Il était donc nécessaire de développer une méthode de représentation concise pour visualiser ces résultats. C'est à cette fin que la carte de dimension fractale a été mise au point. La carte de dimension fractale, telle que présentée dans le chapitre 5, permet une lecture rapide du nombre de bandes fractales et de leurs dimensions respectives pour toutes les directions d'une surface donnée. Cette carte est donc utile aux études s'intéressant aux propriétés d'anisotropie d'auto affinité des surfaces, que ce soit pour étudier les erreurs dans les MNT ou encore pour étudier les caractéristiques fractales des surfaces naturelles ou artificielles. Il s'agit de la première méthode de représentation de la dimension fractale d'une surface capable de représenter la dimension fractale de plusieurs bandes et ce, pour toutes les directions.

L'article se termine par une démonstration de l'utilité des cartes de dimension fractale. L'analyse de qualité des MNT avec les propriétés d'auto-affinité des surfaces entamé au chapitre 4 est approfondie grace à l'application des cartes de dimension fractale. Les qualité des MNT du chapitre 4 est analysé de nouveau et il est démontré que la carte de dimension fractale permet un diagnostic plus complet des caractéristiques des erreurs des MNT.

3.3 Contribution du chapitre 6

L'objectif de l'article du chapitre 6 était de quantifier des caractéristiques bien connues des assemblages de graviers telles que l'imbrication et l'enchâssement en vue d'une modélisation de la probabilité de présence des interstices. Ces

phénomènes sont bien décrits dans la littérature mais les méthodes de quantification demeurent inadéquates. Aucune méthode n'a été trouvée ans la littérature pour quantifier le degré d'imbrication d'une surface de gravier. De plus, les méthodes de quantification de l'enchâssement présentée par Bunte et Abt (2001) sont très difficiles à appliquer sur le terrain (voir chapitre 6).

La principale contribution de l'article est un ensemble de méthodes quantitatives applicable à la caractérisation du recouvrement des particules et de l'ensablement en surface. Ces méthodes de quantification ont été inspirées par des observations sur le terrain qui suggérèrent que le degré de recouvrement des particules voisines peut servir à quantifier l'imbrication à condition que le lit soit constitué de particules grossières. Parallèlement, l'enchâssement des particules grossières est causé par la présence d'une importante quantité de sable en surface. Un point commun important peut être observé entre l'imbrication et l'enchâssement; dans les deux cas les particules grossières sont recouvertes par des particules voisines. De plus, l'article démontre que l'utilisation des estimation visuelles pour quantifier la présence de sable en surface est d'une utilité très limité et aussi que la caractérisation du recouvrement des particules voisines ne peut se faire par estimation visuelle.

3.4 Contribution du chapitre 7

Tout d'abord, cet article fait une contribution générale au domaine de la géomorphologie. La rugosité des surfaces fut postulée comme ayant une influence sur la disponibilité d'interstices. Il a donc été nécessaire de quantifier la rugosité à partir des MNT et non à partir de la granulométrie afin de tenir compte des effets d'agencements tels l'imbrication et l'enchâssement. Pour exprimer la rugosité d'une surface avec un seul paramètre significatif, la mesure du R_{84} a été mise au point. Le R_{84} représente une hauteur caractéristique des dénivelés topographiques pour une distance horizontale choisie. Cette mesure,

décrite dans le chapitre 7, donne donc une nouvelle façon de quantifier la rugosité d'une surface dont l'application n'est pas limitée à la géomorphologie.

L'objectif premier du chapitre 7 était d'arriver à un modèle capable de prédire la disponibilité d'interstices pour un substrat donné. Les méthodes des chapitres 4, 5 et 6 ont été appliquées sur les sites de l'étude et mises en relation avec des mesures directes des interstices. Il a donc été possible d'examiner quel ensemble de paramètres avait la plus grande capacité pour prédire la disponibilité d'interstices dans un substrat. Les méthodes de régression multiple ayant échoué, il a été décidé que pour cette première étape de modélisation des interstices dans un gravier fluvial, seulement la probabilité de présence d'un ou plusieurs interstice sur une surface donnée sera modélisée. Le modèle logistique développé emploie donc toutes les méthodes quantitatives mise au point dans les trois premiers articles de la thèse. Il a été trouvé qu'une bonne prédiction de la probabilité de présence des interstices est possible avec des mesures du diamètre maximal (D_{100}), le R_{84} et le pourcentage de sable en surface. Il s'agit à notre connaissance du premier modèle de prédiction de disponibilité des interstices de surface pour un gravier fluvial. De plus, les résultats indiquent que lorsque seul le diamètre maximal des particules est considéré, la prédiction de présence des interstices réussie dans 50% des cas. Il est donc nécessaire de réviser les pratiques actuelles d'évaluation d'habitat hivernal du saumon juvénile qui considèrent seulement la taille du substrat et négligent les effets de structure.

Chapitre 4: Cost effective non-metric close range digital photogrammetry and its application to a study of coarse gravel river beds

Cost effective non-metric close range digital photogrammetry and its application to a study of coarse gravel river beds*

Patrice E. Carbonneau[1†]

Stuart N. Lane[1]

Normand E. Bergeron[2]

1 Université du Québec, INRS-ETE, 880 chemin Ste-Foy, CP 7500, G1V 4C7, Québec, Canada, phone: (418) 654-2647 fax: (418) 654-2615 email: pcarbonn@nrcan.gc.ca

2 School of Geography, University of Leeds, Leeds, UK

*Contribution to the program of CIRSA (Centre Inter universitaire de Recherche sur le Saumon Atlantique)

4.1 Résumé

La photogrammétrie digitale est reconnue comme étant un outil puissant en géomorphologie. Par contre, les coûts matériels élevés nécessaires à l'application de cette méthode peuvent dissuader les géomorphologues de l'appliquer pour leurs travaux. Cet article présente une méthode de photogrammétrie au sol accessible à un plus large groupe d'utilisateurs et capable de donner des informations topographiques de haute densité et de haute résolution avec un coût minimal. Des Modèles numériques de terrains (MNT) de lits graveleux ont été produits à partir d'images d'échelle 1:165 obtenues avec une caméra 35mm à pellicule, un numériseur commercial et un logiciel de photogrammétrie. L'utilisation de matériel commercial réduit les coûts d'une façon importante en comparaison avec les équipements spécialisée normalement employés. Par contre, ce matériel n'étant pas conçu pour des travaux quantitatifs, il faut prévoir une dégradation de la qualité des résultats. Les analyse de qualité des résultats montrent que la précision des résultats est systématiquement inférieure a 10% du D_{50} des particules du lit. Ceci équivaut à une précision sub-centimétrique. Même si la photogrammétrie digitale est actuellement capable d'une beaucoup meilleure précision, ces résultats sont de qualité suffisante pour de nombreuses applications géomorphologiques. Donc, les simplifications méthodologiques et matérielles de cette méthode qui rendent la photogrammétrie plus accessible sont acceptables.

4.2 Abstract

Digital photogrammetry is now recognised as being a powerful tool in geomorphology. However, the high material costs and skills required by digital photogrammetry may deter non-photogrammetrists from using this technique in their research. This paper demonstrates the use of a close range digital photogrammetric methodology accessible to non-photogrammetrists and yet capable of yielding good quality topographic information on coarse gravel riverbeds at minimal cost. Digital Elevation Models (DEMs) were derived from 1:165 scale imagery obtained with a 35-mm film SLR camera, a commercial desktop scanner and a softcopy photogrammetry package. Quality assessment was based upon independent checkpoints and scaling analysis, it showed that precision of the DEMs was consistently less than 10% of the D_{50} of the bed particles. This translates into sub-centimetric precision. Whilst photogrammetry is presently capable of a better data quality at this scale, quality must be judged with respect to the requirements of the geomorphological applications under consideration. Thus, the methodological simplifications adopted in this research are acceptable in order to make photogrammetry both cost effective and accessible.

4.3 Introduction

Digital elevation models (DEMs) are increasingly being used in fluvial geomorphology for modelling and monitoring riverbed structure. Using close range digital photogrammetry, Butler *et al.* (1998, 2001b), Lane *et al.* (2001) and Stojic *et al.* (1998) have demonstrated the quality and density of data that can be achieved which, allows an investigation of the complex structures of riverbeds that has previously been impossible.

The research presented in this paper was initiated by a need to obtain high-density topographic information concerning the coarse gravel beds used as over-wintering habitat by juvenile Atlantic salmon (*salmo salar* L.). During winter days, the survival strategy of juvenile salmons involves concealment in the interstitial voidspaces of the bed (Cunjak 1988, Rimmer *et al.* 1983). It is well established that the river reaches selected by Atlantic salmon for over-wintering are comprised of coarse gravel (Heggenes 1996, Rimmer *et al.* 1983). Currently, understanding and modelling of this available habitat space is limited by a lack of geomorphologic knowledge consequent with a lack of methods for quantifying and describing the structure of coarse gravel beds and their interstitial voidspaces.

In this context, the digital photogrammetric methodology presented here was developed to obtain topographic information of sufficient resolution and precision to yield high-density information on the surface structure of coarse gravel beds. The precision requirements were established based on the scale of interest. Rimmer *et al.* (1983) have shown that juvenile salmon preferentially select their habitat near coarse particles ('home stones') having a mean diameter of approximately 17 cm during winter. Gregory and Griffith (1996) examined the selection of artificial concealment spaces and found that preferred spaces were those where the fish were able to set their pectoral fins on the riverbed while leaving the dorsal and caudal fins free to move. Suitable concealment spaces are

therefore approximately of a few centimetres in size. The aim of this paper is to assess the extent to which an accessible, cost-effective, close range digital photogrammetric methodology is applicable to this scale of work.

4.4 Photogrammetric and analytical considerations

This section reviews the key concepts that make implementation of cost-effective photogrammetry possible and reviews the concepts relevant to data quality.

4.4.1 Hardware advances

Use of digital imagery and advances in computer-related technologies have made the material requirements of digital photogrammetry less stringent than those of traditional analogue photogrammetry (Chandler and Padfield 1996; Chandler 1999). Experience of camera calibration procedures, such as the self-calibrating bundle adjustment, now make it possible for digital photogrammetry to be carried out with non-metric commercial 35-mm SLR cameras (either digital or film based) instead of the traditional calibrated metric cameras (Fryer 1996, Short 1992). One such package, CUBA (City University Bundle Adjustment), is freely available on the World Wide Web (Short 1999). Thus, with effective calibration, use of 35-mm film cameras could potentially make photogrammetry much more cost effective albeit with some loss of accuracy (Chandler and Padfield 1996). The key question that remains is whether or not this loss of accuracy is acceptable for a given application. This was answered in the affirmative for non-metric close range analytical photogrammetry based on 35-mm camera imagery of streambed morphology (Welsh and Jordan 1983). If it also holds for digital photogrammetric applications, which must consider additional issues such as scanning and the effects of automated DEM extraction, then it allows for the replacement of traditionally expensive and specialized cameras by inexpensive, 'off the shelf' equipment. Softcopy photogrammetry packages, which replace the analogue stereo plotter, have a comparatively lower cost and are much easier to use (Chandler and Padfield 1996). Furthermore,

these packages often offer an automated collection procedure that offers the tempting possibility of easily generated high density DEMs.

4.4.2 Implications of automated DEM generation for data quality

Traditional photogrammetry relied on the user to identify conjugate points in a stereo pair in order to restitute the three dimensional geometry of the object/landform under consideration and so, if data quality may be assessed, automation of this process has some appeal. Manual data collection results in a time limit upon the total number of elevations that can be collected. Automated collection procedures use pixel information to match conjugate points. The most commonly used matching procedure is area-based. Image patches, comprising a pixel submatrix from each image are cross-correlated. Conjugate point pairs are identified as the highest pixel patch cross-correlation (Dowman 1996, Butler *et al.* 1998). Automation of the matching process greatly increases the size of DEMs that can be attained and it also implies that the user no longer requires specialist knowledge to extract DEMs, therefore opening the field of photogrammetry to non-photogrammetrists. However, this apparent ease of use must be treated with caution. The replacement of human judgement during matching introduces the potential of additional error. Matching errors take two forms, incorrect and unsuccessful matches. Incorrect matches occur when the algorithm falsely matches two points. Alternatively, an unsuccessful match occurs when if the algorithm fails completely to identify a conjugate for a given point. In the first case the resulting elevation will be false. In the second, elevation accuracy depends on the effectiveness of interpolation which, is a function of surface structure (Lane *et al.* 2000). A classic difficulty where either error may occur is the perspective problem. During matching, the highest correlation will be achieved for two identical patches. An image of a given object should be identical in both images of the stereo pair for a perfect match to occur. However, photogrammetric restitution of an object's geometry is made possible by the fact that images are taken from different camera stations. In the case of

three-dimensional objects, this creates differences in patch appearance on the two images that will be proportional to the ratio of the relative roughness in the image to the flying height of the camera (camera-object distance). In the cases where this ratio is high, images along the edges of larger objects may in fact be quite different, figure 4.1 shows an example where targets adjacent to a stone and visible in the right images are hidden by this stone in the left image. These differences in images, common along edges, cause the matching algorithm to fail and are known as perspective errors. Thus perspective errors may cause incorrect matches if the algorithm is still able to find patches with sufficient correlation. Unsuccessful matches may also occur, leaving elevations to be determined by interpolation.

The number of unsuccessful matches in a DEM is generally expressed with a percentage of matched points. An automatically collected DEM will therefore typically contain a combination of matched points and interpolated points.

Thus, the transition to automated DEM generation therefore introduces errors that must be assessed (Lane *et al.* 2000). Data quality may be examined according to three aspects, precision, accuracy and external reliability (Butler *et al.* 1998). DEM precision is controlled by random error. Accuracy is controlled by systematic error. External reliability refers to the sensitivity of parameters derived from the DEM to DEM error. Surface accuracy and point accuracy should be distinguished. Point accuracy is systematic error in point elevations while surface accuracy is systematic error on the surface. Thus, the ensemble effects of point precision and accuracy control the standard deviation of errors (SDE) and the mean error (ME) of the surface.

One difficulty of quality assessment is the acquisition of a sufficient amount of independent survey data, also called check data, to properly represent the surface (Lane *et al.* 2000). Even when such data is available, Lane *et al.* (2000) found that accuracy statistics remain insensitive to changes in parameters used

in the DEM collection algorithm. Furthermore, spatially distributed parameters such as slopes and aspects derived from DEMs were found to be sensitive to the DEM collection parameters. For this reason, external reliability approaches may be used to obviate the need for check data during DEM quality assessment.

4.4.3 Basis for external reliability analysis

External reliability is evaluated by comparing a parameter derived from the DEM with a theoretical reference. In large scale DEMs, external reliability can be based upon slope values (Lane *et al.* 2000) or other hydrologically relevant parameters (Walker and Willgoose 1999). However, this is inappropriate for the small scale DEMs of interest to this study. Recently, Butler *et al.* (2001b) have compared DEM scaling properties to the expected scaling properties of natural surfaces as predicted by fractal theory (Nikora *et al.* 1998; Russ 1994). In the case of natural surfaces scaling properties are studied by computing the variance of elevation differences as a function of scale. In geomorphology, computation of the semi-variogram is the most reliable method for this analysis (Butler, *et al.* 2001b). Robert (1988, 1991b) and Bergeron (1998) have both used the semi-variogram to study roughness characteristics of linear topographic profiles of streambeds. Butler *et al.* (2000) have used 2 dimensional semi-variograms to study scaling properties of surfaces obtained with digital photogrammetry.

The two-dimensional semi-variogram is given by (generalized from Butler *et al.* 2000):

$$\gamma(p,q) = \frac{1}{2(N-|p|)(M-|q|)} \sum_{i=1+\frac{|p|-p}{2}}^{N-\frac{|p|+p}{2}} \sum_{j=1+\frac{|q|-q}{2}}^{M-\frac{|q|+q}{2}} [Z(i+p,j+q)-Z(i,j)]^2 \qquad (4.1)$$

Where p and q are the lags in the x and y directions, M and N are the dimensions of the surface in the x and y directions respectively and Z(i, j) is the elevation at point (i, j). The complex form of the summation indexes is necessary for the computation of negative lags. Negative lags, meaningless in one-dimensional

scaling analysis, are necessary in two-dimensional scaling analysis. The combinations of p, q should allow for measurement of semi-variance along all orientations (0° to 360°) of the surface. The orientation at a given lag is:

$$\omega = \arctan\left(\frac{q}{p}\right)$$
(4.2)

If p and q are positive, only angles from 0° to 90° are covered, thus justifying the necessity to compute the semi-variance for all combinations of $\pm p$ and $\pm q$. However, examination of equations (4.1) shows a symmetry where $\gamma(p, -q) = \gamma(-p, q)$ and $\gamma(p, q) = \gamma(-p, -q)$. Computation of the semi-variances $\gamma(p, q)$ and $\gamma(p, -q)$ is therefore sufficient.

Furthermore, inspection of eq. (4.1) reveals that for a given (p, q) lag, the semi-variance is evaluated along all parallel lines of direction ω on the surface thus giving much a bigger sample size than if a single elevation profile of the surface along direction ω had been used. Figure (4.2a) shows an example semi-variogram surface. These figures are best analysed by extracting profiles from them and plotting on log-log axes. Figure (4.2b) shows an example. Here the profile has been extracted along the 0° direction corresponding to the p-lag direction. The profile shows 3 linear sections with breaks of slope. Each linear section corresponds to a scaling band within which the surface is self-affine. The existence of multiple bands on a given surface may be explained by the action of multiple processes, each at a different scale. For example, Robert (1988, 1991b) attributed the observation of 2 scaling bands to grain and form roughness, respectively. It should be noted however that the number of scaling bands observed on a semi-variogram profile is highly dependent upon the resolution and scale of the topographic data, be it a profile or a surface, used in its calculation. Processes operating on a scale inferior to the resolution of the topographic data cannot be detected and inversely, those operating on a scale greater than entire modelled surface or profile will remain inaccessible. Furthermore, linear bands that span less than one order of magnitude, as can be

seen in figure 4.1, are rarely considered significant. However, the presence of linear scaling bands still gives a basis for an evaluation of external reliability. Provided the surface has a Gaussian distribution of elevations, derivations from this linear behaviour may be attributed in errors in the surface or DEM, therefore allowing for evaluation of DEM quality without the recourse to independent check data.

4.5 Methodology
4.5.1 Data collection in the field

This study was concerned with the surface structure of riverbed gravel. For this reason, four exposed banks, labelled RSM1 through RSM4, of the Ste-Marguerite river, Québec, Canada were selected for the study. The areas were selected for increasing roughness and grain size. Median diameter (D_{50}) for each site was evaluated at 18, 27, 57 and 61 mm respectively. Data was collected using a single Minolta X-300 35-mm film based SLR camera, mounted on a gantry. The optical axis was always oriented to be approximately vertical. The camera could slide between 2 positions along an aluminium railing system. The translation (baseline) distance was calculated in order to obtain a 60 % overlap in the stereo-pairs. The camera lens was approximately 1.1 m above the ground. Figure 4.3 shows raw images of all 4 study sites.

Within the overlap area of each stereo pair, 30 survey points were identified with targets. The targets consisted of copper disks of 1.5cm diameter and approximately 2mm thickness. Each target was painted in fluorescent orange and marked with a cross hair. All targets were surveyed with a Leica TC-600 total station. To obtain better results, the standard total station prism staff was replaced by a prism mounted on a 15 cm steel prism-foot that finished in a sharpened point. Additionally, a level was added to the prism. No measure of

camera exterior orientation parameters was taken in the field; these were determined during the processing stage.

4.5.2 Digitisation of images

Digital images were obtained by scanning negatives to an interpolated density of 10 μm (2400 dpi) with 256 grey levels with an UMAX desktop scanner. One important feature of this scanner is the presence of two glass plates that flatten the film during scanning, minimising additional image deformation during to this process. However, this is not a standard photogrammetric scanner and some loss of quality was expected to occur.

4.5.3 Restitution of surface topography

The stereo-pairs were processed using the OrthoMAX module of the ERDAS Imagine software. This softcopy photogrammetry package carries out interior orientation, ground control point measurement and estimates exterior orientation with a least-squares block bundle adjustment. At this point in the process, the CUBA software is used to perform camera calibration. With calibrated values for the camera parameters, automated DEM extraction may be carried out with OrthoMAX using area-based matching.

The interior orientation is normally established using fiducial marks present on the image. In the case of a 35mm SLR camera, such marks are absent and an alternative method must be applied. Short (1992) showed that, provided the inner geometry of the camera is stable and the dimensions of the negatives are known, the use of the corners of the negatives as fiducial marks was acceptable, giving rapid solutions for inner orientations with a minimal loss of accuracy. The image size was therefore set at 36X24 mm with fiducials in all 4 corners.

Ground control was established using 20 of the 30 survey targets, the other 10 being reserved as independent checkpoints. In the ground control measurement phase, the user must manually identify conjugate pairs for each ground control

point. This will yield photo-coordinates for each ground control point used in camera calibration. This calibration, carried out with the CUBA software, also requires initial values for camera principal distance (i.e. the focusing distance), principal point offset and radial distortion. The initial value for camera principal distance was estimated using the basic lens equation (Wolf 1983) assuming a focal length of 50mm and a flying height of 1.1m. The parameters of principal point offset and lens distortion were initially set to zero. The CUBA software then carries a least-squares bundle adjustment to attempt to accurately estimate the camera parameters.

DEM extraction may now be carried out with these calibrated camera parameters. During extraction several parameters may be user specified to control and optimize stereo matching performance. The parameters adopted here were determined by Butler *et al.* (1998) as being optimal for close range digital photogrammetry of coarse gravel. The DEMs were therefore collected with optimal matching parameters and at a resolution of 1 mm yielding DEMs of approximately 400 000 X 400 000 pixels in size.

4.5.4 Quality check

The first quality check should always be visual inspection. Comparison of DEMs and orthorectified images should provide the user with a qualitative measure of the overall success of the DEM in representing the topography of interest. Gross errors may thus be identified as spikes in the DEM that are not present in the surface topography.

Quantitative aspects of DEM quality were examined in terms of accuracy, precision and external reliability. The quality of the block bundle adjustment may be estimated with the standard deviation of unit weight parameter ($\hat{S}_w$). For cases with an $\hat{S}_w$ below 1, the problem is under-constrained and if the $\hat{S}_w$ is over 1, the problem is overconstrained. Although this parameter should ideally be

unity, values ranging from 0.5 to 2 are considered acceptable (Vision International 1999). High $\hat{S}_w$s are often observed when gross field measurement errors are present.

After visual inspection, unused survey points were used to establish mean elevation differences and standard deviation of elevation differences indicating surface accuracy and surface precision respectively. External reliability was evaluated with respect to the scaling properties of the surface. Prior to the calculation of semi-variograms for each DEM, minor editing was carried out to eliminate spikes along the edges. These errors may be dismissed as edge effects and should be eliminated since they have a great effect on the semi-variogram (equation 4.1). Thus, a local statistical filter with a spatial extent of 3 X 3 mm was applied to replace edge spikes by the local average. After editing, the semi-variogram was computed for each DEM. Following Klinkenberg (1994) and Butler *et al.* (2001b), a distance of reliability of half the image size was adopted. Therefore, each semi-variogram was computed (see eq. 4.1.) with all combinations of p, ranging from 1 to M/2 and q ranging from –N/2 to N/2. This satisfies the symmetry requirements to obtain semi-variances in all directions. The profiles extracted from the semi-variance surfaces were then examined to determine if the scaling properties were similar to those of natural surfaces.

4.6 Results

4.6.1 Preliminary results

Repeated attempts at camera calibration with the CUBA software failed to provide reliable calibrated camera parameters. The parameters of principal point offset and radial distortion, expected to be similar since the same camera was used, showed variations of over 100%. Furthermore it was found that the error estimated by the calibration software for each parameter was also of the order of 100%. Attempts at calibrating only the focal length were also inconclusive. The most likely reason for this failure is the presence of distortion in the image that was introduced by film curvature at the time of exposure. Film unflatness at the time of exposure is often recognised as the major limiting factor for the successful calibration of non-metric cameras (Fryer 1996, Robson 1990).

However, DEMs generated with 20 control points and uncalibrated camera data were of an unexpectedly high quality. Figure 4.4 shows 20 control point DEMs for each study site. Feature identification is good especially considering the fact the camera data used in the process was approximate. The standard deviations of unit weight are, for sites RSM1 through RSM4, 1.26, 1.30, 1.10, 0.94, respectively. These results suggest that for the scale of interest to this project, camera calibration may not be required.

It was therefore decided to study the quality of DEMs generated with the uncalibrated and therefore approximate camera parameters in order to determine if these were of sufficient accuracy to yield geomorphologically significant information. Additionally, an analysis was carried out to determine the sensitivity of DEM quality to the number of control points. Another series of DEMs was therefore generated using uncalibrated camera data and an increasing number of control points. For each study site, additional DEMs were generated with 3, 5, 10 and 15 control points. Finally, another sensitivity analysis was carried out to

examine the effect of a perturbation of the focal length to assess the potential error introduced by the use of an approximate value for the camera focal length.

4.6.2 Visual inspection of DEMs

Figures 4.5 present DEMs collected with 3 control points with arrows indicating the position of the control points. The number of features identifiable in the DEM is immediately seen to be poor with wide areas showing significant levels of noise. This figure illustrates a well-established principle of photogrammetric design: the ground control points should cover the whole X Y Z dimensions of the imaged surface. Particularly in figures 4.5a and 4.5b, the corners are of reduced quality. An improved spread of control points could improve results and it is necessary to use more than the theoretical minimum of 3 ground control points.

Figure 4.6 shows the DEMs collected with 5 control points. The increased coverage has led to a large increase in the level of feature identification. Increasing the number of control points beyond 5 had qualitatively little effect at first observation. However if 5 control point DEMs and 20 control point dems are compared (figure 4.7) it can be seen that stone edges are much more clearly defined in the 20 control point DEMs. This demonstrates that elevations in the vicinity particle edges are more sensitive to the number of control points.

4.6.4 Standard deviations of unit weight

Table 4.1 gives $\hat{S}_w$ for all collected DEMs. It can be seen that for a low number of control points, the $\hat{S}_w$ tends to be below 1 meaning an under constrained problem. However, results for 15 and 20 control points are well within the acceptable range of 0.5-2.

4.6.5 Independent check data analysis

The unused surveyed targets were used as independent checkpoints for comparison with their elevations as predicted by the DEM. A check data analysis

was carried out to compare the measured elevations of these points with their elevations as predicted by the DEM. Two results are output by this analysis: the mean difference of measured and predicted elevations and the standard deviation of this difference. These results are normalized with the D_{50} value for each respective study site. Table 4.2 gives the results of this quality assessment. Surface accuracy is generally seen to be proportional to the number of ground control points. The mean errors decrease as a function of the number of GCPs. However, the trend for the standard deviation is less clear. The results for the 20 GCP DEMs are nevertheless good. For all DEMs, the mean error for 20 control points is below 10% of the D_{50} . This yields surface accuracy's range from −1.5 to 3.6 mm. Similarly, the standard deviation of elevation differences for checkpoints yields surface precisions ranging from ±2.1 to ±8.5mm. These results are encouraging since they are sub-centimetric, the range of this research. However, these results were generated with a low number of check points offering a limited spatial coverage of the surface of the surface and further analysis is required to asses the quality of these DEMs.

4.6.6 Matching precision

Sites RSM1 and RSM2 are seen to have the highest percentage of matched points (Table 4.3). These surfaces are the most textured and it is to be expected that the stereo-matching algorithm perform best on these. An examination of the spatial distribution of matched and interpolated points revealed that, for RSM1 and RSM2, matched points are fairly evenly distributed along the surface but with perspective errors reflected in some concentrations of interpolated points along rock edges. In cases RSM3 and RSM4, the coarser grains have increased roughness and relief and have made the effects of perspective error more important. The increased grain sizes have increased the total area of the DEM that is subject to perspective error thus explaining the matching results.

4.6.7 Scaling analysis

External reliability, with respect to scaling properties of the surface, was evaluated using the semi-variogram. Following editing, semi-variogram surfaces were generated for each DEMs with 3 and 20 control points. Figure 4.8 shows an example of semi-variance surfaces for RSM3. It can be seen that the 3 ground control point case has higher semi-variance and important differences of morphology. However it is difficult to study the scaling behaviour of the DEM with figure 4.8. In order to assess the presence or absence of power law scaling behaviour, semi-variogram profiles were extracted from the surface, as in figure 4.2, and plotted in log-log space (figure 4.9). This figure shows that the 3 ground control point profile has systematically higher variance. Furthermore the greatest differences are observed at smaller scales. Similarities may be seen between cases RSM1 and RSM4 and between RSM2 and RSM3. For cases RSM1 and RSM4, the high lag, larger scale, section appears to have higher slope than the small scale section. This is contrary to theoretical expectations and a plausible explanation would be that error at small lags is very important. Cases RSM2 and RSM3 fit more closely with theoretical predictions since slope at high lags is lesser than at lower lags. The differences in semi-variogam profiles may be explained by differences in errors and how these errors affect the semi-variogram. The high error at low lags for case RSM4 may be understood by re-examining figure 4.5d. The large amount of small scale noise present along rock edges dominates the semi-variogram signal. Since a high amount remains in the 20 GCP case (Figure 4.4d), the semi-variogram profiles are similar. Profiles for RSM1 may also be understood by re-examining the DEMs. The profiles show an important change in shape from concave to convex. An examination of the DEMs used in the generation of the semi-variograms (figures 4.4a and 4.5 a) show the errors to be of different nature. In the 3GCP case, figure 4.5a, large areas with small amplitude error ('noise') can be seen. However in figure 4.4a, the errors seem to be located in a few small areas, particularly along the edge of rocks. These spikes around rock edges were not edited and these results suggest that

they adversely affect the semi-variogram by causing an over-estimation of semi-variance at small lags. This means that the errors in the 3CGP case are related to problems in the 3D restitution of the surface caused by insufficient control points. However for the 20 GCP case, the errors are controlled by perspective problems which is why error zones are found along rock edges.

Quantitative analysis of semi-variogram profiles was based on their linearity. Prior to calculating the linearity of the profiles, the user must establish slope breaks between self-affine scaling bands. Slope breaks were identified visually with a graphic interface running under the MATLAB environment. The user must determine the number of segments and then visually regress lines drawn across the points of each segment. Breaks points are then given by line intersections. Once slope breaks are established, linear regression is carried out on each segment and the sum of squared errors (SSE) is used to quantify linearity. Table 4.4 gives the results of the linearity tests. For sites RSM2, RSM3 and RSM4, the addition of control points has linearized the first band of the semi-variogram profile. In the case of RSM1, the curvature in the low lag section suggests that further editing is required in order obtain the expected linear behaviour. It can therefore be seen that the addition of control points produces a DEM that obeys more closely the power-law scaling pattern recognised in natural surfaces. However, this analysis also suggests that more research is required to fully understand the effect of error on the scaling properties of a surface.

4.6.8 Sensitivity to focal length error

Given the difficulties of determining an adequate camera calibration an analysis was undertaken to examine the effect of an approximate focal length upon accuracy. This was done by perturbing the focal length and examining the resulting effects upon derived DEMs. A perturbation of 2 mm was used representing a change of approximately 50 cm in the object space. This is therefore an important perturbation that exceeds the error associated with

manual measurement of the focusing distance with a steel tape. For the 20 control point DEM of each study site, this 2 mm perturbation was applied to the focal length and the DEM was recollected. Once again, edge effect spikes were edited prior to comparison in both perturbed and non-perturbed DEMs.

The resulting DEMs were subtracted from the original 20 gcp DEM (figures 4.10). It can be seen only a few points show a large difference. Furthermore these points are almost exclusively located along rock edges where perspective errors are very important and the collection process is unstable. Overall the median differences, expressed as a percentage of D_{50} are −0.1%, -0.1%, -0.3% and − 1.3% for sites RSM1 through RSM4 respectively. This demonstrates that areas of perspective problems are more sensitive to focal perturbation since coarser substrates generally have more relative relief and thus are more subject to perspective problems. Although there is a trend for the perturbed DEM to be slightly higher, the difference in elevation remains very small when compared to our accuracy requirements. It was however noted that the block bundle adjustment in OrthoMAX compensated for focal length perturbations by adjusting the camera flying height. During this free-network least squares adjustment, the co-ordinates of the ground control points are considered fixed and therefore the adjustment varies other parameters to obtain a solution. This explains why focal perturbation has such a minor effect.

4.7 Discussion

The objective of this study was sub-centimetric surface precision. Statistics for the 20 GCP DEMs show the required sub-centimetric precision was achieved. Scaling analysis reveals the expected power-law behaviour, thus supporting the validity of the DEMs. Matching statistics were lower than hoped for but some loss of quality is inevitable when using non-calibrated cameras. Furthermore, in coarse environments poorer performance of the matching algorithm is expected due to the increased presence of perspective problems. However, the overall results suggest that camera calibration is not required in order to obtain sub-centimetre precision at this scale. Assuming a camera height of 110 cm and an average surface precision of 0.5 cm, this represents an error of 1/220. Whilst much lesser errors could be possible using advanced methods and specialized equipment, this was not necessary despite the loss of accuracy, there is an important gain of accessibility and cost-effectiveness.

The accuracy, precision and redundancy of the ground control are the key element in the success of this methodology. This research showed that 15 to 20 GCP are necessary in order to eliminate camera calibration. Accurate ground control was also found to be highly important. Initial attempts at photogrammetric surveys in the course of this research have shown that inaccurate ground survey will lead to very poor accuracy and may even prevent the block bundle adjustment from converging thus making DEM collection impossible. One key element was found to be prism foot design. Since ground control targets are small, it is imperative to accurately place the prism on a given target. Conventional total station rods were found to be awkward and inaccurate for this scale of work. Positioning of ground control is also important. Figure 4.5 shows that when control points are aligned a loss of DEM quality occurs. Control points should be distributed evenly through the X, Y, and Z dimensions of the study site.

Perspective errors are the most important cause of matching failure and DEM error. Unfortunately, perspective errors are a fundamental difficulty for photogrammetry where there is high relative relief. Area-based matching stereo-matching algorithms will always achieve poor results in these areas. Post-processing provides the only solution. Automated DEM collection requires a post-processing phase of inspection and manual editing to a greater extent than traditional manual DEM collection methods. Gross errors can easily be identified and replaced by the local average. Smoothing is commonly applied to DEMs. However recent results (Butler *et al.* 2001b) show that simple automated editing using a 3X3 low pass filter may cause curvature in the semi-variogram profile. This suggests that more refined filter design is required if DEMs are to retain the power-law scaling behaviour characteristic of natural surfaces. One possible avenue of research is in the design of filtering methods that target areas of perspective error.

4.8 Conclusion

A method has been proposed for a cost-effective implementation of digital photogrammetry. In close range applications, the resulting surface precision of 1:220 obtained with "off the shelf" equipment translates into sub-centrimetric surface precision. This level of precision, achieved without camera calibration, is made possible by the presence of numerous and redundant ground control points. Issues of data quality still require more research in order to be properly assessed. Scaling analysis offers much potential for establishing a measure of DEM quality without recourse to large check data sets. However, our results show that different types of errors, present in an automatically collected DEM, will affect the semi-variogram in different ways. Progress in this area therefore requires research and classification of the possible ways in which errors affect the scaling properties of a DEM. Current methods of assessment still produce a valid estimate of DEM quality. Our results therefore show that photogrammetry can be made more accessible to a much wider range of users who might benefit from high-density topographic data with reasonable accuracy obtained at minimal cost.
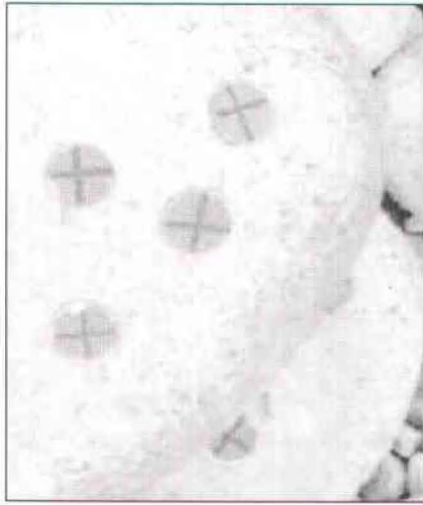
(a)   (b)

Figure 4.1. Illustration of perspective error.
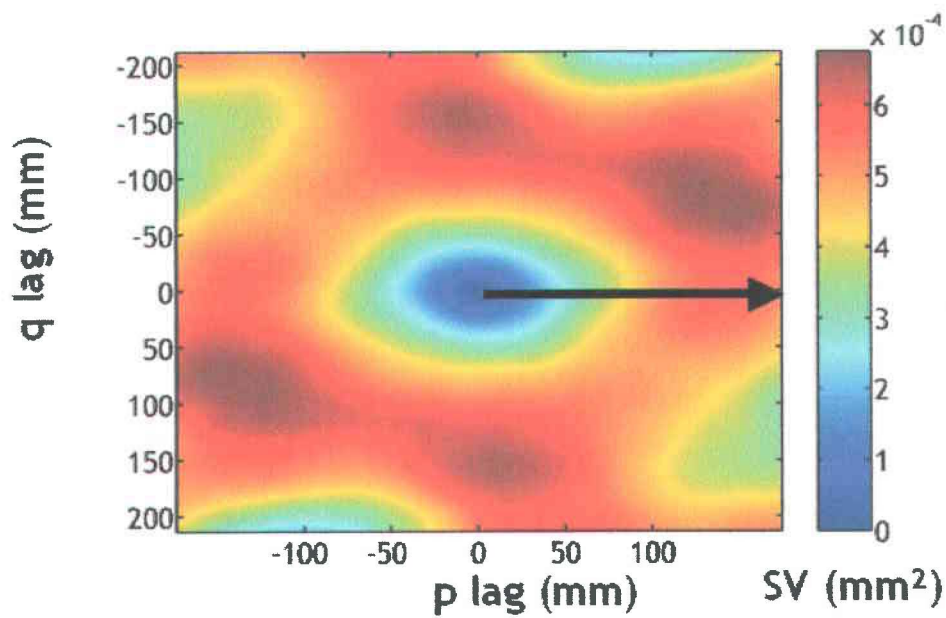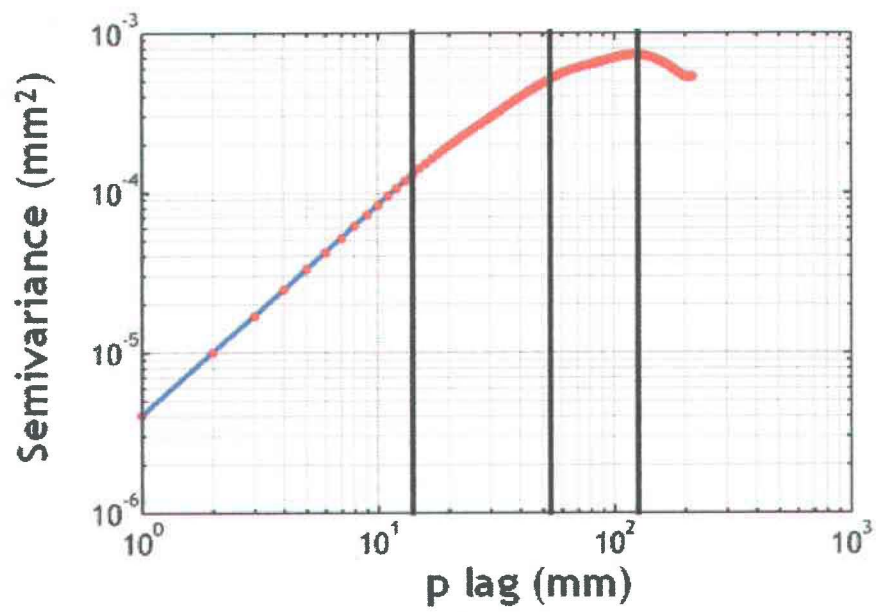
Figure 4.2. a) Example of a semi-variogram surface b) profile extracted from a).
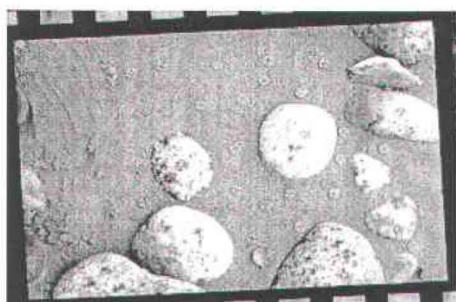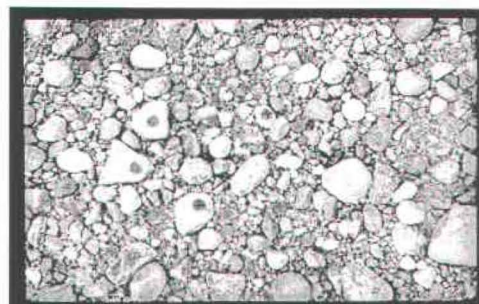
a) RSM1 b) RSM2
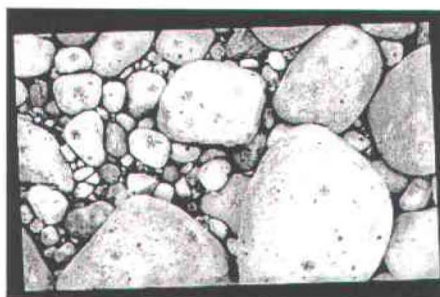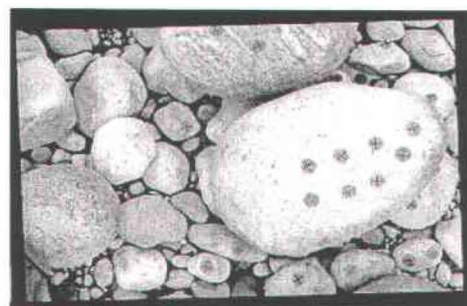
c) RSM3 d) RSM4

Figure 4.3. Raw images of the four study sites.
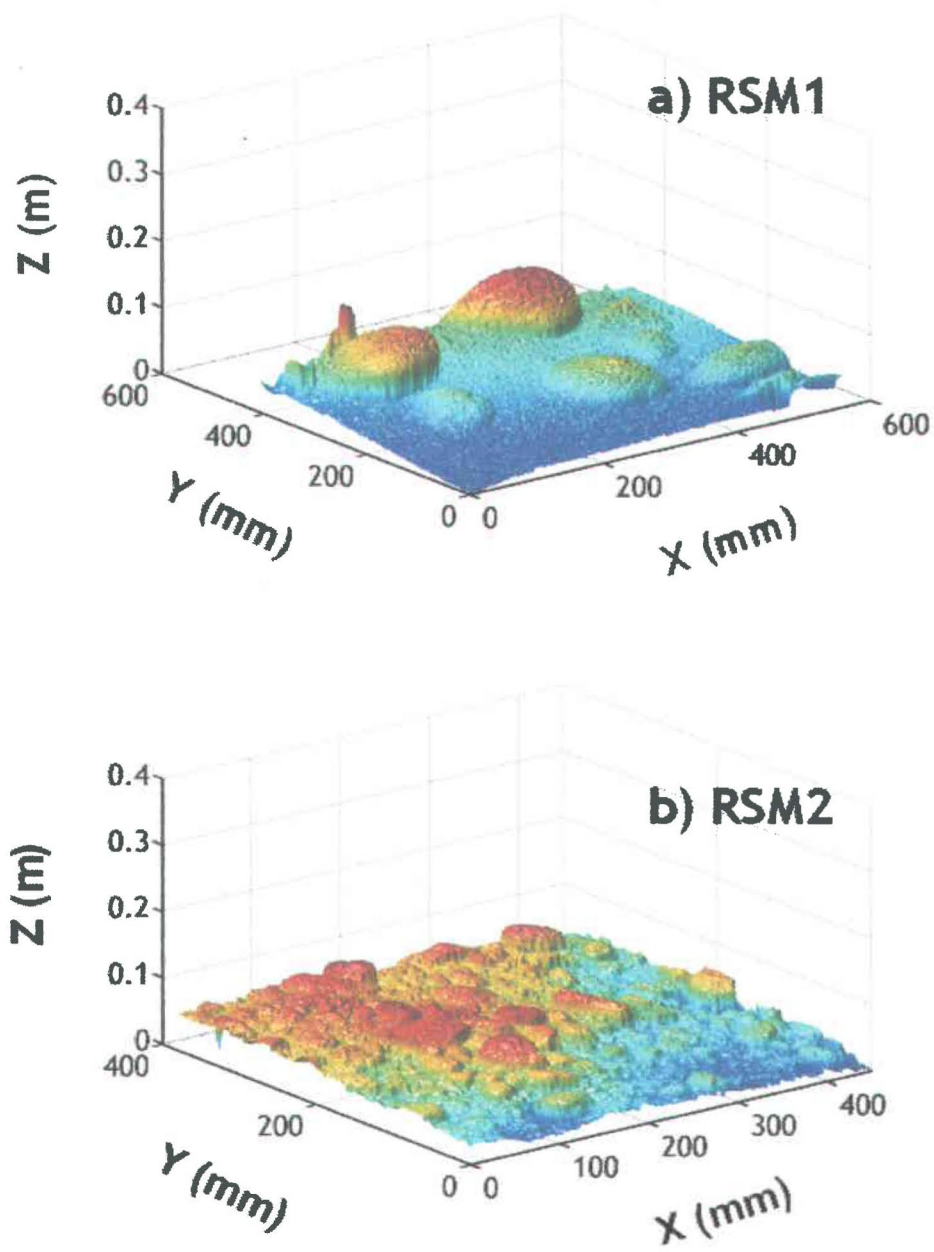
Figure 4.4. Digital Elevation Models (DEMs) collected with 20 control points and uncalibrated camera parameters.
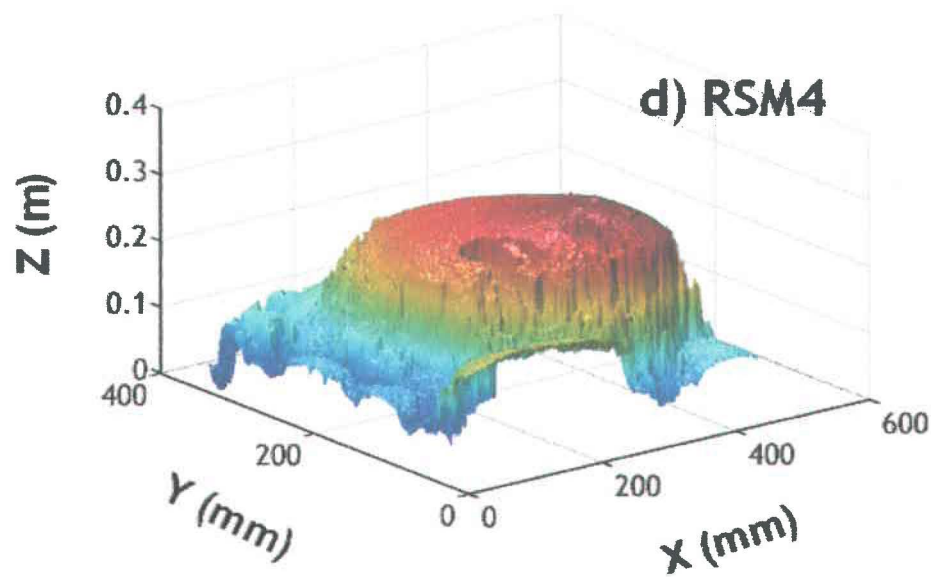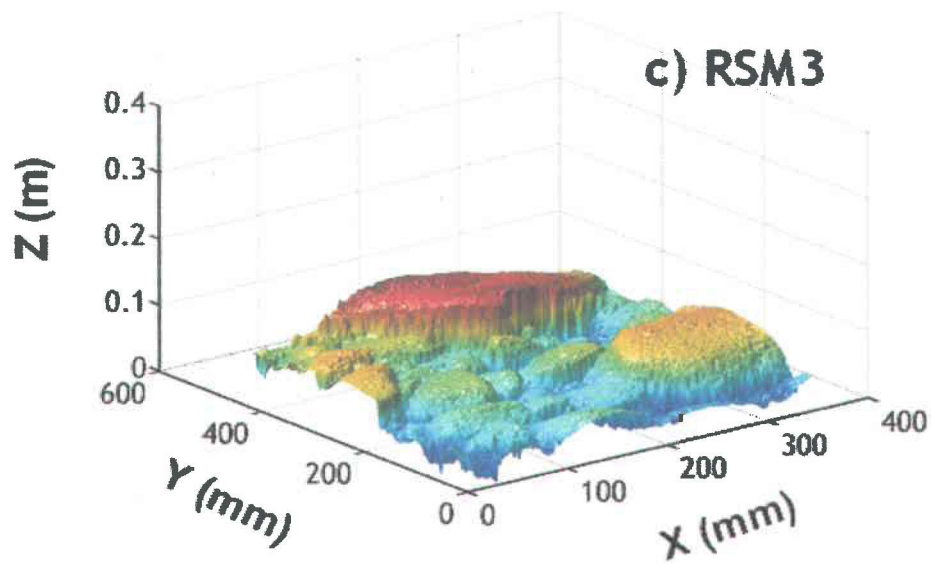
Figure 4.4 (continued). Digital Elevation Models (DEMs) collected with 20 control points and uncalibrated camera parameters.
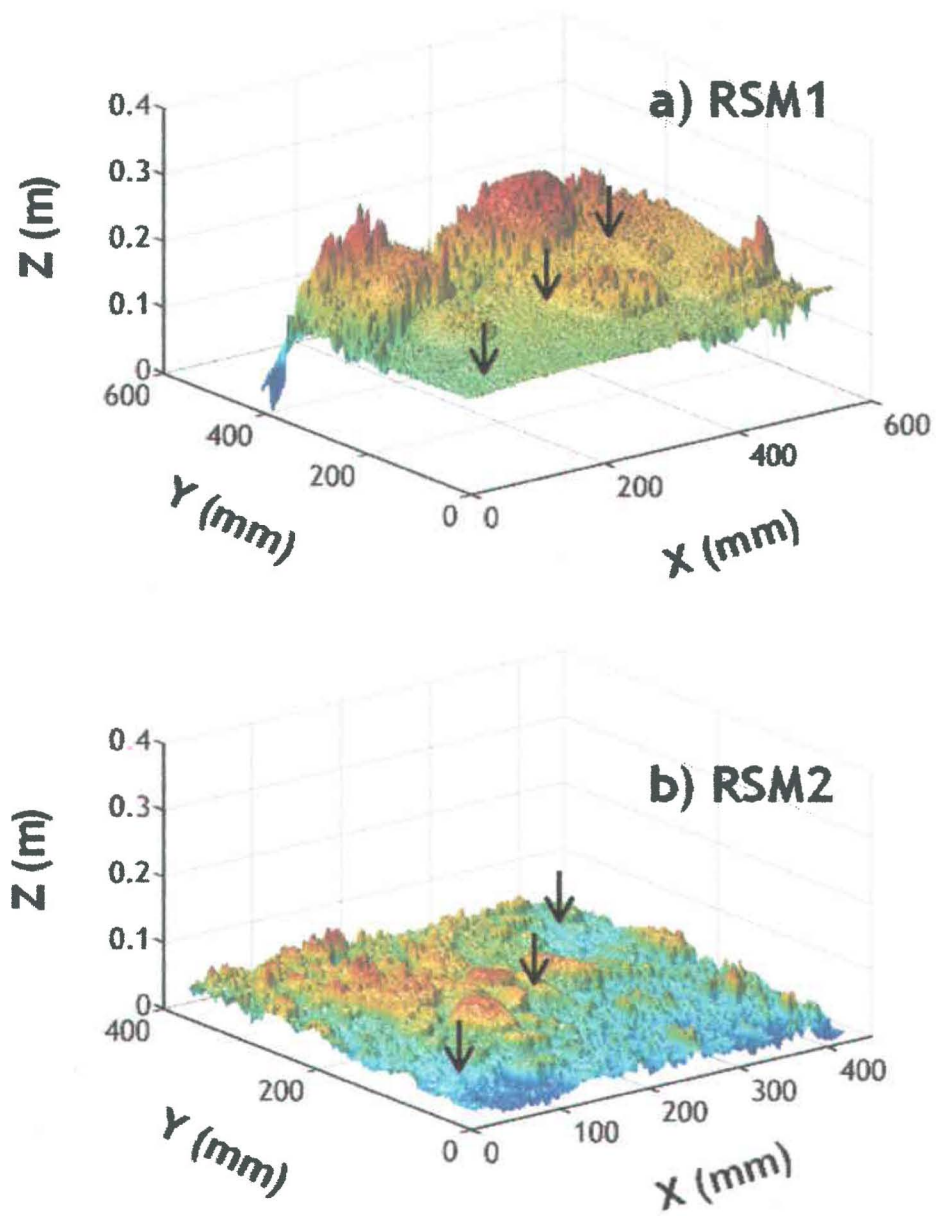
Figure 4.5. Digital Elevation Models (DEMs) collected with 3 (shown with arrows) control points and uncalibrated camera parameters.
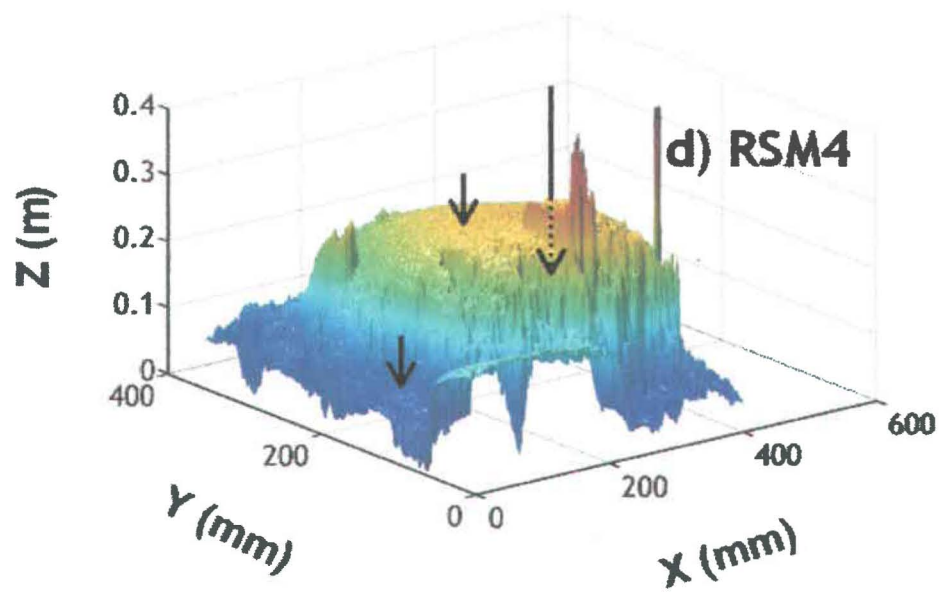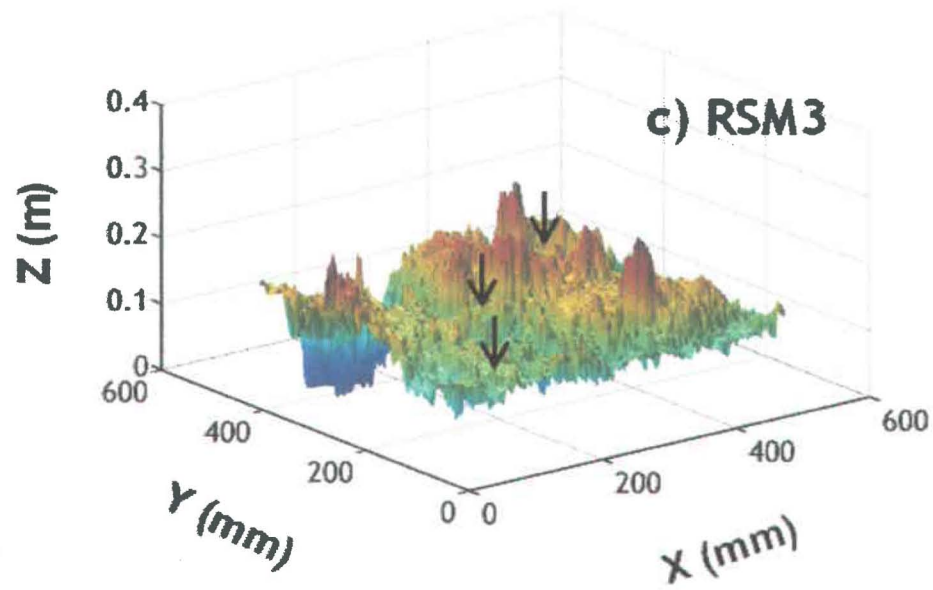
Figure 4.5 (continued). Digital Elevation Models (DEMs) collected with 3 (shown with arrows) control points and uncalibrated camera parameters.
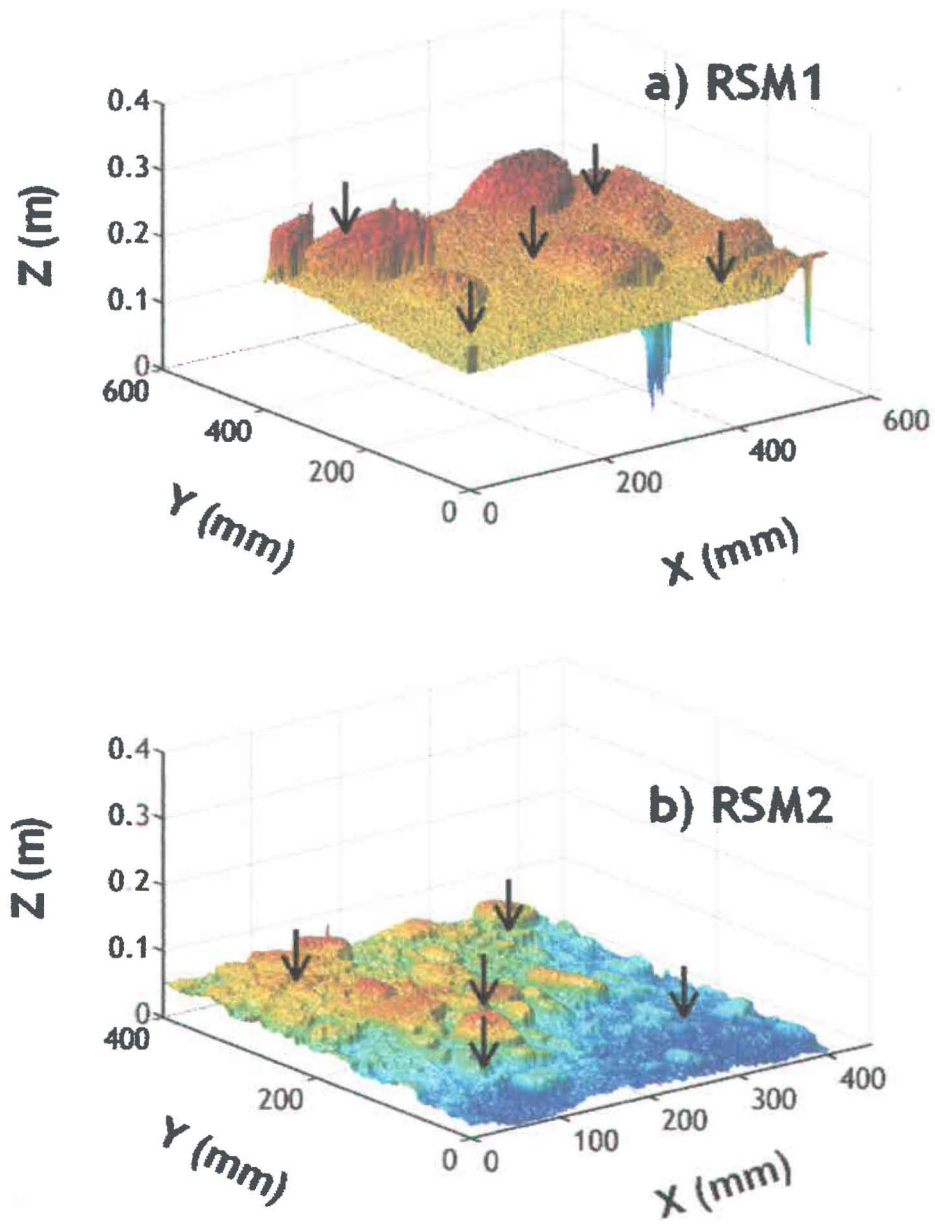
Figure 4.6. Digital Elevation Models (DEMs) collected with 5 (shown with arrows) control points and uncalibrated camera parameters.
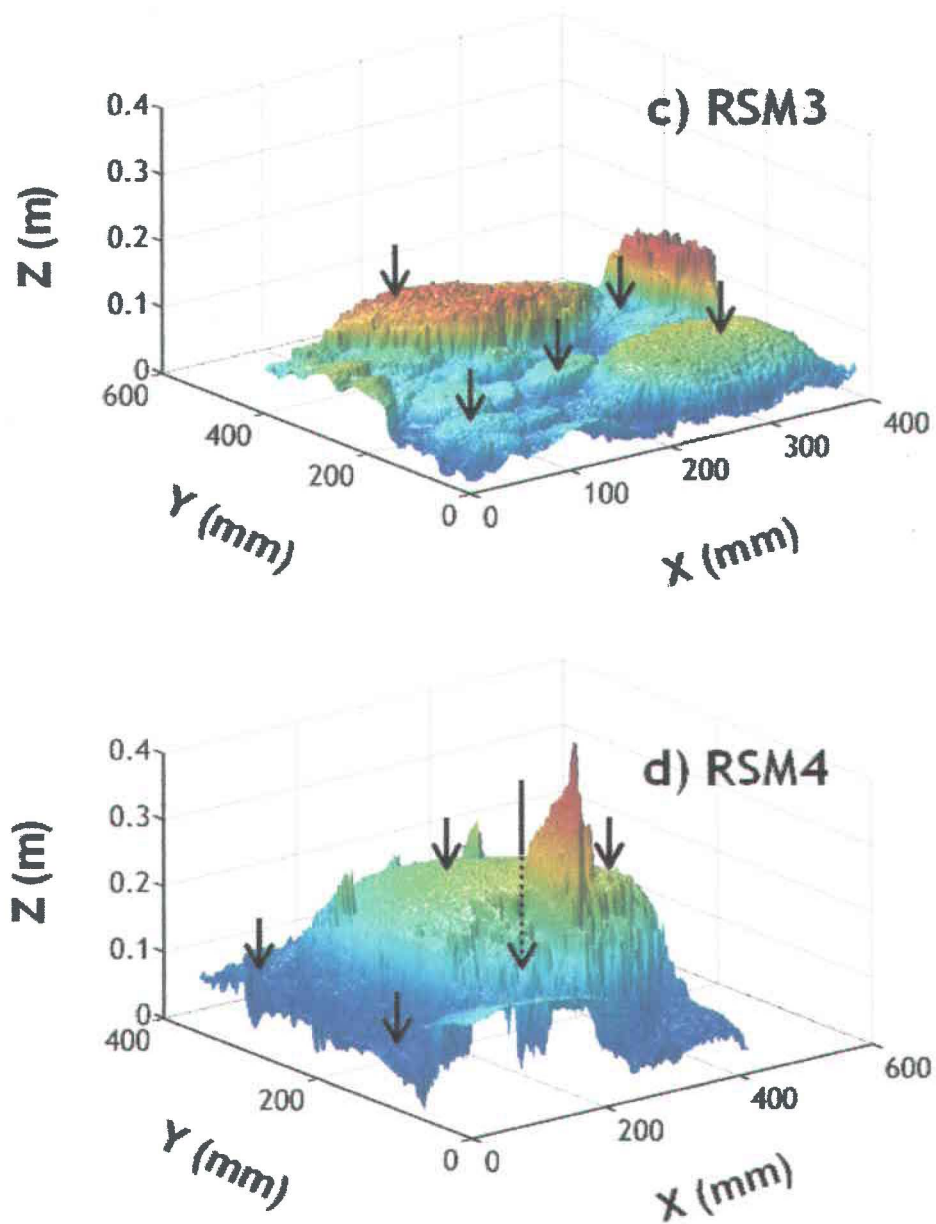
Figure 4.6 (continued). Digital Elevation Models (DEMs) collected with 5 (shown with arrows) control points and uncalibrated camera parameters.
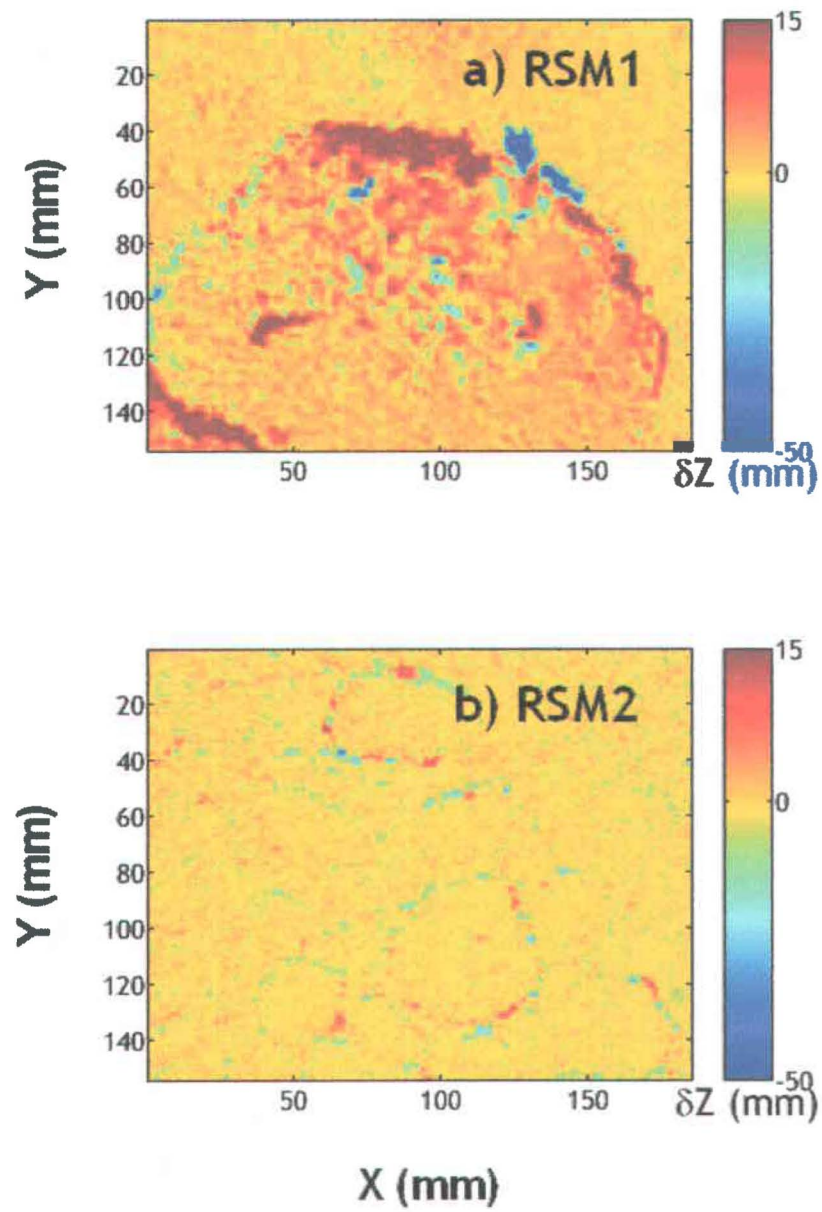
Figure 4.7. Enlarged areas showing, in plane view, the difference between the DEM with 20 ground control points and 5 gcps.
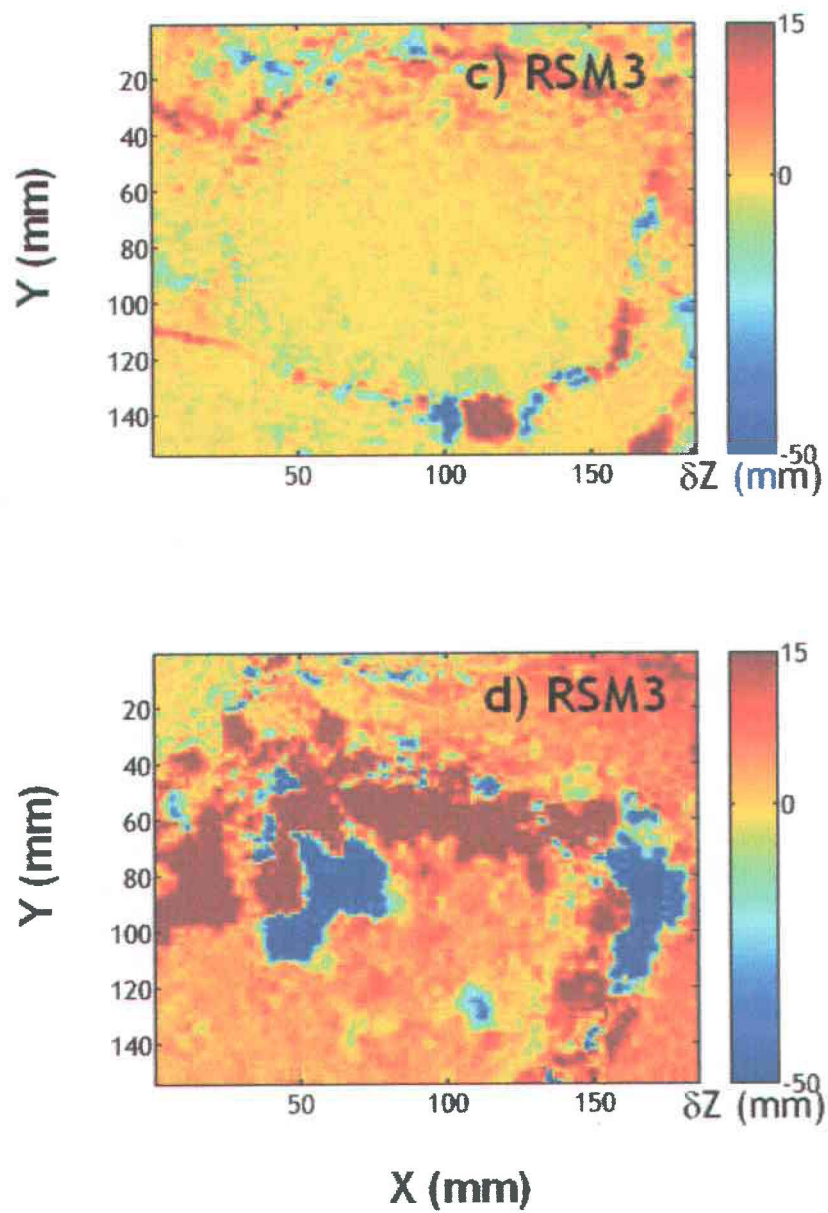
Figure 4.7 (continued). Enlarged areas showing, in plane view, the difference between the DEM with 20 ground control points and 5 gcps.
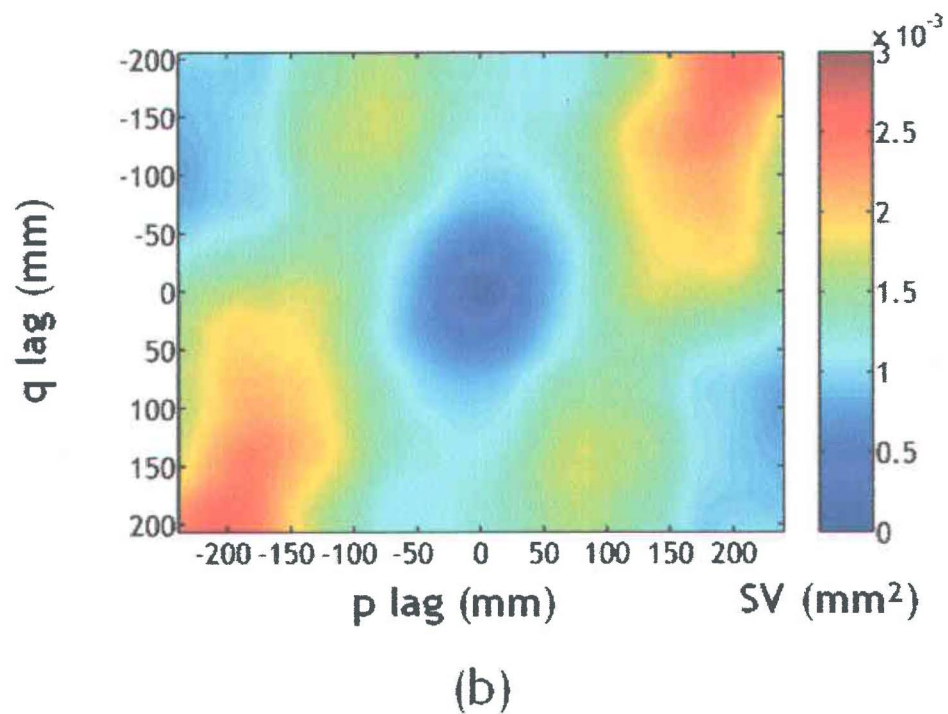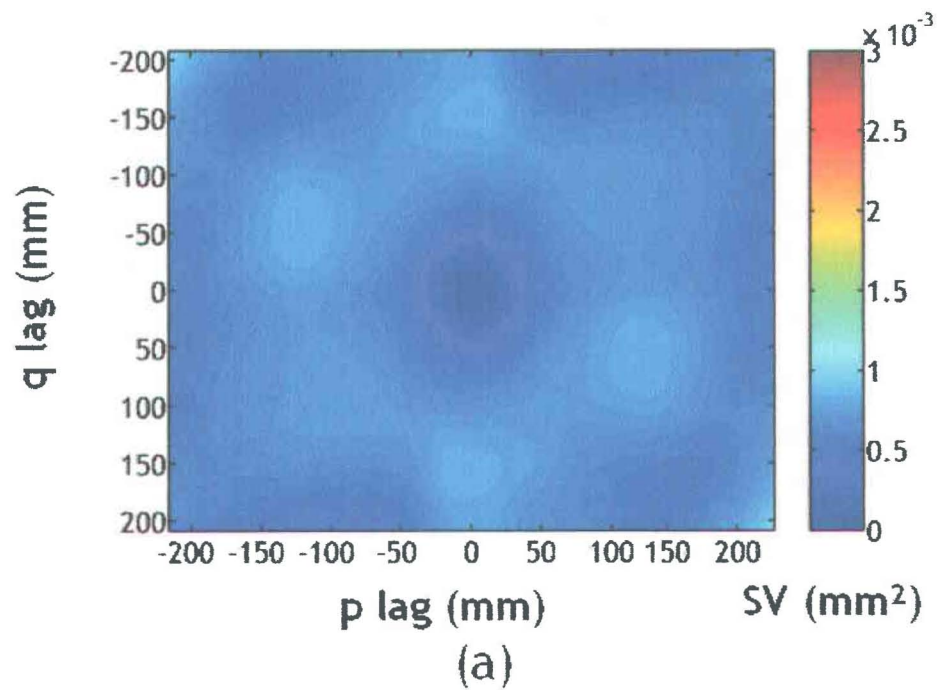
Figure 4.8. Semi-variogram surfaces for site RSM3. a) 20 ground control point case b) 3 ground control point case.
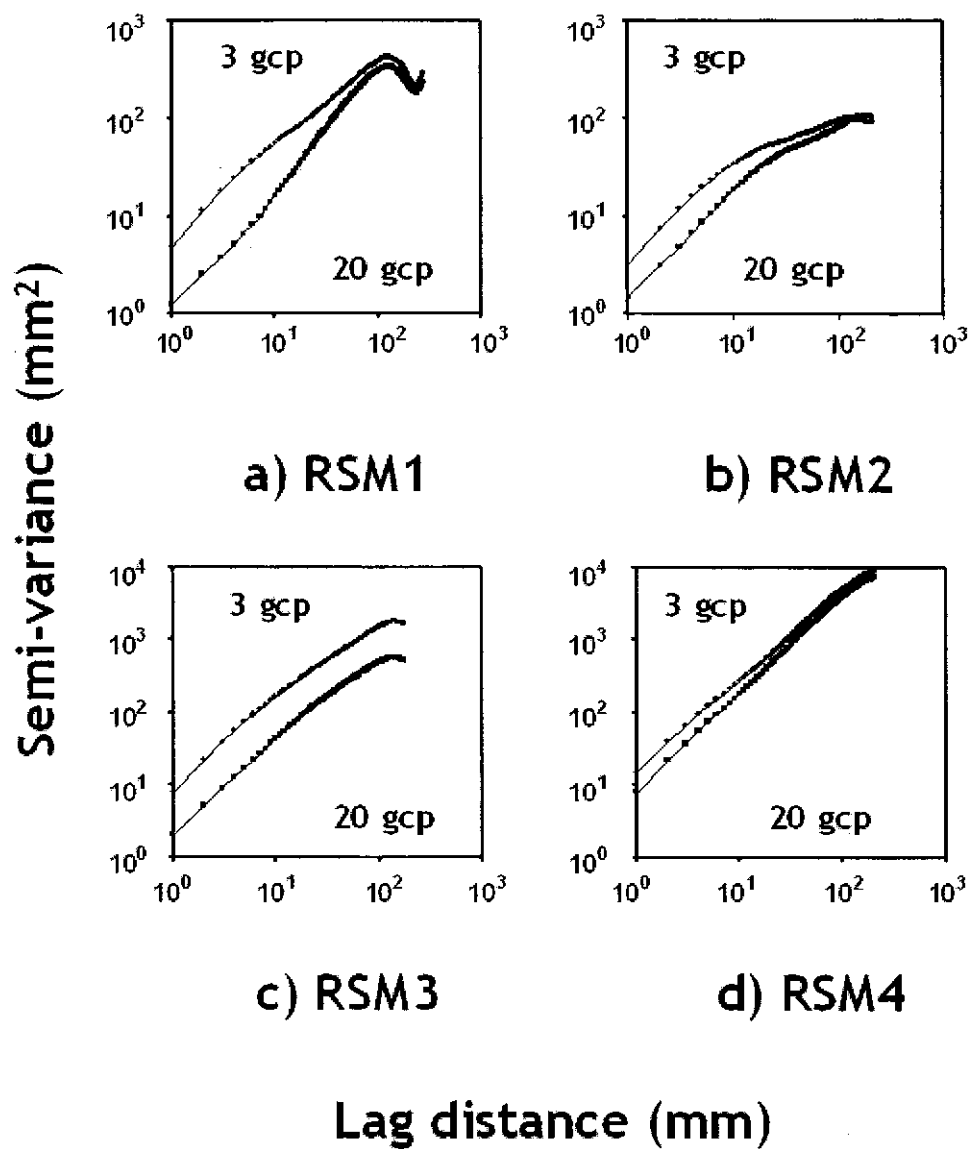
Figure 4.9. Semi-variogram profiles for 3 ground control point and 20 ground control point extracted along the p lag axis.
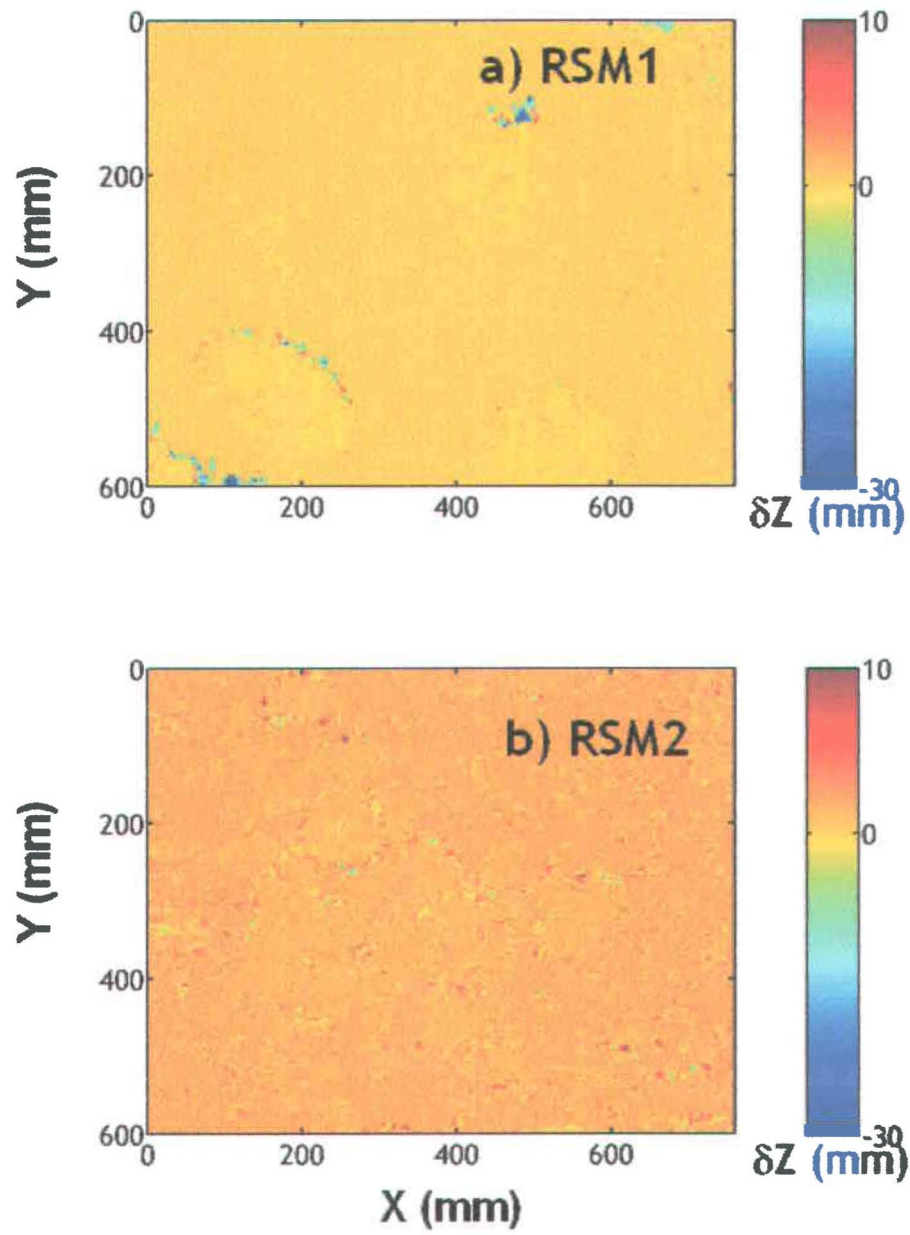
Figure 4.10. DEM differences for focal length perturbation results.
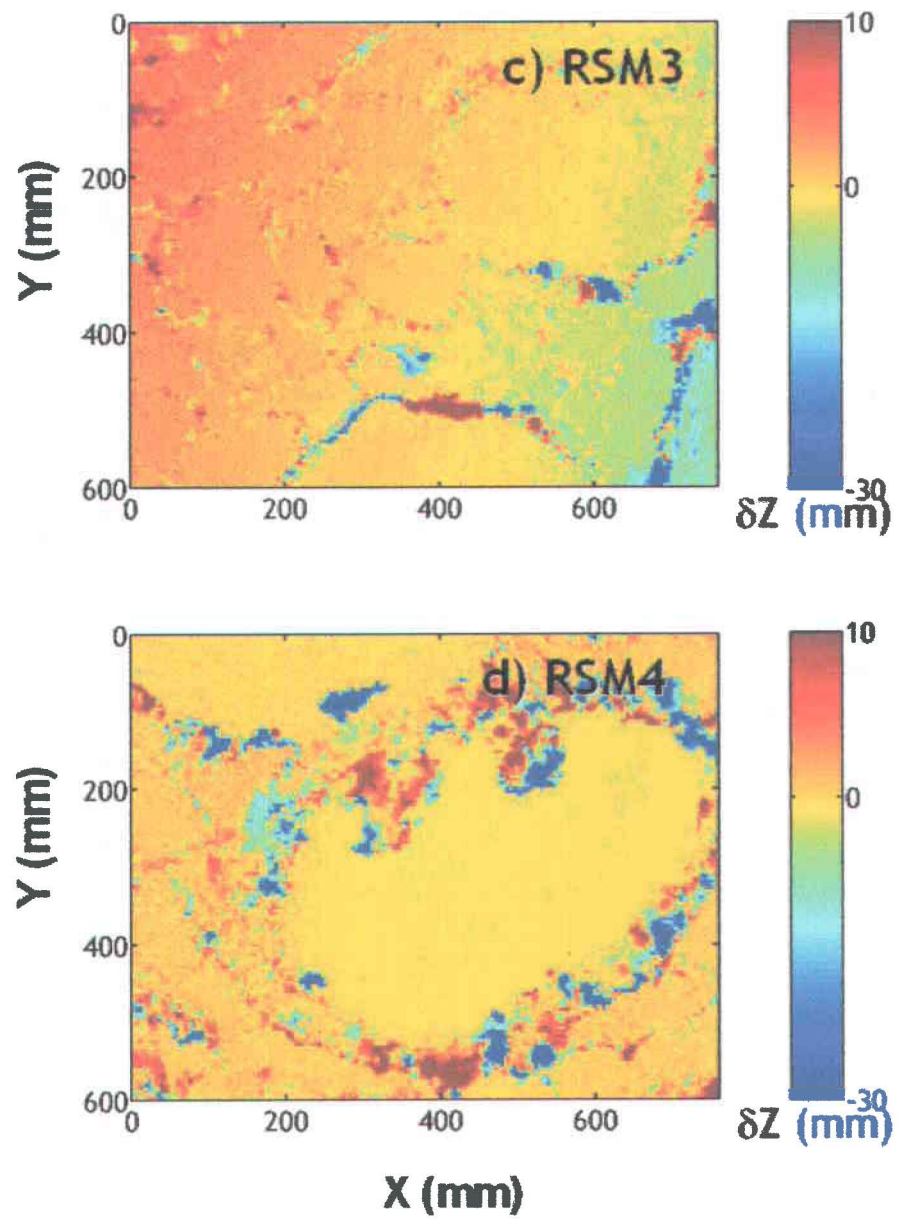
Figure 4.10 (continued). DEM differences for focal length perturbation results.

Table 4.1. Standard deviations of unit weight.

	3GCT	5GCT	10GCT	15GCT	20GCT
RSM1	0.5	0.5	0.66	0.64	1.26
RSM2	0.69	0.55	1.16	1.19	1.30
RMS3	0.86	0.90	0.74	0.79	1.10
RMS4	0.70	0.85	1.20	1.33	0.94

Table 4.2. Quality assessment based on elevation differences between independent checkpoints and DEM elevations.

# of GCPs	RSM1		RSM2		RSM3		RSM4	
	mean (%)	std (%)	mean (%)	std (%)	mean (%)	std (%)	mean (%)	std (%)
3	-27.2	9.8	-19.8	19.4	-28.1	55.3	8.9	12.7
5	-27.8	11.5	-5.3	7.9	4.1	25.5	10.0	20.7
10	-20.4	13.0	-3.2	7.8	1.2	37.1	8.7	10.5
15	-16.7	11.5	0.4	8.2	2.9	21.6	6.2	11.6
20	-8.0	13.1	0.0	8.1	7.2	18.4	5.0	17.7

All values are expressed as a percentage of the D_{50} for the DEM surface.

Table 4.3. Percentage of matched points.

	3GCT	5GCT	10GCT	15GCT	20GCT
RSM1	71	90	89	90	90
RSM2	55	78	74	82	71
RMS3	30	33	42	42	43
RMS4	47	48	48	55	55

Table 4.4.   SSE values for linear regressions carried out on scaling bands.

# of GCPs	RSM1 SSE		RSM2 SSE		RSM3 SSE		RSM4 SSE	
	band 1	band 2	band 1	band 2	band 1	band 2	band 1	band 2
3	0.190	n.a.	0.070	0.002	0.006	0.090	0.022	0.010
20	0.230	n.a.	0.001	0.010	0.011	0.006	0.007	0.001

Chapitre 5: Automated identification and omnidirectional mapping of linear bands in semi-variogram analysis

Automated identification and omnidirectional mapping of linear bands in semi-variogram analysis*

Patrice E. Carbonneau[1†]

Stuart N. Lane[2]

Normand E. Bergeron[1;]

1 Université du Québec, INRS-ETE, 880 chemin Ste-Foy, CP 7500, G1V 4C7, Québec, Canada, phone: (418) 654-2647 fax: (418) 654-2615 email: pcarbonn@nrcan.gc.ca

2 School of Geography, University of Leeds, Leeds, UK

*Contribution to the program of CIRSA (Centre Inter universitaire de Recherche sur le Saumon atlantique)

† Corresponding author

5.1 Résumé

Un nombre croissant de chercheurs appliquent l'étude des propriétés d'auto-affinité des surfaces afin de mieux comprendre la structure complexe des surfaces naturelles et aussi afin d'étudier les caractéristiques des erreurs des modèles numériques de terrain (MNT). En géomorphologie, l'approche la plus répandue est l'analyse des surfaces et des profils de semi-variance. Par contre, deux difficultés fondamentales surgissent lors de l'étude des surfaces de semivariance à des fins de compréhension des surfaces naturelles. Premièrement, il n'existe aucune méthode acceptée pour identifier automatiquement et objectivement les bandes linéaires d'auto-affinité dans les surfaces de semi-variance. Deuxièmement, il n'existe aucune méthode de représentation synthétisée des propriétés d'auto-affinité de la surface entière d'une semi-variogramme en deux dimensions. Cet article propose une solution à ces deux difficultés. Premièrement, l'article présente une méthode automatisée d'identification des bandes linéaires d'auto-affinité fondée sur des techniques de vision numérique. Deuxièmement, nous présentons un nouveau graphe, la carte de dimension fractale, conçu pour une représentation concise de toutes les propriétés d'auto-affinité d'une surface. Finalement, l'utilité de la carte est démontré par un exemple d'application à l'étude de la qualité des MNT du chapitre 4.

5.2 Abstract

A growing number of researchers are applying semi-variogram analysis to study the scaling properties of natural surfaces (Robert, 1988; 1991) or the quality of digital elevation models (Carbonneau *et al.,* in press). When applying semi-variograms to scaling analysis, two fundamental problems emerge. First, there is no established method for automated identification of linear bands in semi-variance surfaces. Second, there is no established method for the synoptic representation of scaling properties and fractal dimension as a function of both lag and direction. This paper addresses both issues. First, we describe a new method for the automated identification of linear bands based on image processing methods for line detection. Second, we present a new graph used for the omnidirectional mapping of fractal dimension which is shown to be useful for a synoptic assessment of the extent of linear bands, their fractal dimension and their level and degree of anisotropy. Finally, the usefulness of fractal dimension maps is examined through their application to the quality analysis of the high resolution DEMs of chapter 4.

5.3 Introduction

Semi-variograms are often used to study and characterize the scaling properties of natural surfaces. For example, Robert and Richards (1988), Robert (1988; 1991) and Bergeron (1998), have used 1D semi-variograms of topographic profiles to study roughness and scaling properties of river beds. In such studies, 1D semi-variograms are modelled as log(semi-variance) vs log(lag) and assume a Gaussian distribution of elevation differences. In this representation, linear portions of the semi-variogram correspond to self-affine scaling bands and their slope allows the calculation of the Hausdorff dimension which gives a measure of profile complexity (Robert, 1988; Robert and Richards, 1988; Klinkenberg and Goodchild, 1992; Bergeron, 1998). For natural surfaces, the physical significance of these self-affine scaling bands lies in the roughness scales of the surface.

Scaling analysis has allowed for the identification of a roughness scale associated with particle roughness and another larger scale associated to form roughness (Robert, 1988; Robert, 1991; Bergeron, 1998). Each scale of roughness has its own Hausdorff dimension H_D, also known as the fractal dimension, as calculated from the slope of the scaling band on the semi-variogram plot. Scaling analysis has also been applied to the analysis of DEM quality (Chapter 4). In the case of DEMs derived from automated digital photogrammetry, the high resolution and large size that can be achieved leads to difficulties in the determination of DEM quality since the surveying of a suitable amount of check point data becomes tedious (Lane *et al.*, 2000). Scaling analysis has been proposed as an alternate method of quality analysis which does not rely on conventional methods of check point surveying (Chapter 4). The basis for this approach is the observation that natural surfaces show specific scaling properties (Oliver and Webster, 1986; Butler *et al.*, 2001). However, for both these applications of scaling analysis, the objective identification of linear scaling bands and associated slope break points in the semi-variogram plot is difficult. Figure 5.1 shows an example of two semi-

variogram profiles with associated linear bands. In the case of natural surfaces, the semi-variogram plot will present one scaling band for each scale of roughness present in the measured surface. Figure 5.1 shows that certain sections of the semi-variogram are curved. Since the spatial extent of the linear bands is generally our main interest, the identification method must distinguish linear and curved sections, and so determine the number of bands and the extent of each band. This process, which may be readily accomplished by human judgement, is difficult to automate. No method for formal band identification has been proposed in the literature and current methods for band identification in semi-variograms rely on human observation or *a priori* knowledge on the number of scaling bands in the profile. However, if the process of band identification is to be truly objective, it must be automated and it must not require *a priori* knowledge. Furthermore, automation of band identification offers the potential of processing large numbers of semi-variogram profiles.

A second difficulty arises when considering the fractal analysis of a surface such as modelled by a digital elevation model (DEM). In this case, the 1D semi-variogram may be extended to 2D as shown in chapter 4. 2D semi-variograms have often been used in geomorphology (Oliver and Webster 1986, Klinkenberg and Goodchild 1992, Butler et al. 2001b, chapter 4). They are particularly useful when the scaling properties of a surface are anisotropic. Figure 4.2a shows an example of such a semi-variogram surface, calculated from a DEM. The main advantage of 2D semi-variogram analysis is that surface anisotropy may be studied since semi-variance is calculated for all combinations of lags in the x and y directions. However, the methods currently used for the analysis of 2D semi-variograms are still strongly based on methods originally developed for 1D semi-variograms. The analysis of 2D semi-variograms is generally performed by first extracting four profiles in directions 0°, 45° 90° and 135° and then identifying linear bands visually for each profile (Butler et al. 2001b). The use of four profiles provides only a partial description of a semi-variogram surface.

Extraction of more profiles is possible, but since no method exists for automated band identification, this rapidly becomes a tedious process. Furthermore, concise representation of this information is difficult. There still is no established method for representing both fractal dimension and the extent of linear bands for all profile directions on a single graph. Consequently, it is currently difficult to fully interpret 2D semi-variograms. This is especially true of the interpretation of the anisotropic properties of a 2D semi-variogram. With the use of four profiles, this interpretation has an angular resolution of 45°. Clearly, a method capable of representing semi-variogram surface properties with increased angular resolution could lead to a much-improved understanding of the scaling properties of natural surfaces.

This paper addresses the issues of automated band identification and representation of semi-variogram surface properties with a new method for analysing semi-variogram surfaces and profiles. We shall discuss a fully automated method for objective identification of statistically significant linear bands in 1D semi-variogram profiles that uses a line detection algorithm. We then show how automated band identification applied to all 1D semi-variogram profiles present in a 2D semi-variogram surface can be used for the construction of an omnidirectional map of fractal dimension which plots fractal dimension and band extent as a function of lag and direction. The high information content and usefulness of this omnidirectional mapping of fractal dimension will be demonstrated with applications of scaling analysis to DEM quality.

5. 4 Methods

5.4.1 Linear band identification

Traditional band identification methods rely upon human judgement to identify the extent of linear bands or to determine the number of bands present. Whilst this method has given good results in the past, it remains subjective and can be tedious if many semi-variograms are to be analysed. Automated linear band

identification would allow for objective analysis of large numbers of 1D semi-variogram profiles. An automated linear band identification algorithm should be able to identify the lower and upper bounds of all scaling bands in a semi-variogram without any *a priori* knowledge of the number of bands present. A pattern recognition approach based on line detection was chosen to perform this task. This approach was selected for its capacity to identify lines in an image without *a priori* knowledge of their number, orientation or position in the image. The algorithm developed here is an extension of basic algorithms developed for line detection by researchers in the fields of digital image processing and remote sensing (Babu and Nevatia, 1980; Castleman, 1996; Richards and Jia, 1999).

5.4.2 Line detection in a binary image

Basic line detection in an image is a type of convolution filtering. The following kernel noted K_{45} is used for detection of lines with an orientation of 45°:

$$K_{45} = \begin{pmatrix} -1 & -1 & 2 \\ -1 & 2 & -1 \\ 2 & -1 & -1 \end{pmatrix} \tag{5.1}$$

This convolution kernel has an important property. The sums of the elements of each line and each column is zero. Consequently, the sum of all elements is zero. Let us consider two 3X3 binary image matrixes, L_{45} and L_{90}, representing lines with orientations of 45° and 90°, respectively.

$$L_{45} = \begin{pmatrix} 0 & 0 & 1 \\ 0 & 1 & 0 \\ 1 & 0 & 0 \end{pmatrix} \qquad L_{90} = \begin{pmatrix} 0 & 1 & 0 \\ 0 & 1 & 0 \\ 0 & 1 & 0 \end{pmatrix} \tag{5.2}$$

If we convolve these matrixes with K_{45} we obtain:

$$K_{45} \otimes L_{45} = 6 \qquad \text{and} \qquad K_{45} \otimes L_{90} = 0 \tag{5.3}$$

therefore, the convolution of a line detection kernel K_ω with a binary image will yield a predictable maximum, called here the detection threshold, in areas of the image where lines of orientation ω are present. Exact calculation of the threshold value will be demonstrated further. It is important to note that a kernel

K_ω can only detect lines in direction ω. Position of the line in the image may also be determined from the convolution result. In applications of line detection, images submitted to detection are larger than the kernel. For an image of size NxN and kernels of size S_K, convolution will have a valid output of size $N-S_K+1$. Points in this matrix equal to or greater to the threshold identify lines and their position in the image. The identification and localisation of multiple linear portions of different slope in an image is then possible if we successively apply several kernels with values of ω spanning the desired range.

For 3X3 kernels, only lines with orientations of 0°, 45° and 90° may be detected. However, for our purpose kernels capable of high angular resolution are required. It is therefore necessary to increase the size of the kernel to improve angular resolution. However, whilst bigger kernels will have a better capacity for angular resolution, the increased processing time they require imposes an upper limit on maximum kernel size. After a trial and error process, a kernel size of 50X50 was found to have sufficient angular resolution. Kernels are constructed from a 50X50 matrix. Pixels on a line of angle ω and one pixel wide are set to 49 with the rest of the matrix set to -1. This respects the property of zero sum. When convolved with a 50X50 binary image of a line of orientation ω the result is 2450. The difference in convolution maxima for angles $\omega°$ and $\omega°+1°$ is at least 1225 which allows for a reliable capacity for resolving angles $\omega°$ and $\omega°+1°$.

In order to apply line detection kernels to 1D semi-variograms, the semi-variograms must be converted to binary images. Image size was determined based on kernel size. Since kernel size was already determined to be 50X50, the lines detected in the semi-variogram image by this kernel will have a minimal length of 50 pixels. Since length is counted in pixels, line length is not a function of angle in this method. It was decided that linear bands with a minimal length of one half order of magnitude should be detectable. Semi-variogram image size is therefore set as a function of the spanned orders of magnitude with 50 pixels

being equivalent to one half order of magnitude. For example, a semi-variogram spanning two orders of magnitude will be digitised to 200X200 pixels. Following digitisation, morphological dilation is required because round-off errors in the digitising process often result in minor imperfections in linear sections. Due to these imperfections, not all positive pixels in the detection kernel will fall within the linear section, causing line detection to fail. Dilation of the semi-variogram image insures that the positive pixels of the line detection kernel fall within a linear section when it is present. However, dilation alters the predicted detection threshold and it is therefore necessary to recalculate this value.

If we apply morphological dilation to image L_{45} we obtain:

$$DL_{45} = \begin{pmatrix} 0 & 1 & 1 \\ 1 & 1 & 1 \\ 1 & 1 & 0 \end{pmatrix} \tag{5.4}$$

after convolution with K_{45} we obtain:

$$K_{45} \otimes DL_{45} = 2 \tag{5.5}$$

Each off diagonal value has caused a reduction of 1 in the convolution result. Therefore, to predict the detection threshold in the case of a dilated line, it is necessary to count the off diagonal pixels. This can be done with a convolution filter. If we convolve DL_{45} with a 3X3 identity matrix we obtain:

$$DL_{45} \otimes I_3 = 7 \tag{5.6}$$

Since DL_{45} has 3 pixels along the diagonal, this means that 4 pixels are off-diagonal. A generalized detection condition for linear sections can therefore be established as:

$$K \otimes DL \geq (S_K)^2 - I_{SK} \otimes DL \tag{5.7}$$

Where K is the line detection kernel, DL is the dilated binary line image, S_K is the size of the detection kernel in pixel and I_{SK} is an identity matrix of size S_K . This yields an exact threshold value for each $S_K X S_K$ area in the line image by counting the number of pixels in each $S_K X S_K$ area and subtracting their contribution to the maximum convolution value. Single points satisfying the condition represent a

detected line of length S_K. For lines with length I pixel, with $I > S_K$, the number of points, or pixels, satisfying the condition will be $I-S_K$. Linear sections are therefore identified by successive convolution of binary semi-variogram images with detection kernels for angles ranging from 0 to 90°, in increments of 1°. After each convolution, and thus for each angle, the detection condition is verified to determine if a linear section is present.

5.4.3 Statistical testing of identified bands

The morphological dilation of the binary images induces a slight tolerance to curvature which makes a linearity test necessary. Once linear bands have been isolated, the original semi-variogram profile, plotted on log-log axes, is used to carry out linear regression within the bounds of the detected bands. Conventional regression statistics are inadequate to detect potential outliers in this case. Each semi-variogram point represents half the variance in a population of elevation differences. Since fractal theory predicts the existence of linear scaling bands, the regression line may be seen as a series of predicted semi-variances for the elevation difference populations at different lags. If a semi-variogram point does not fall on the regression line, this means that semi-variance for that elevation difference population is different than that predicted by the regression line. To determine the significance of this difference, it is therefore necessary to test the difference between the semi-variances observed on the semi-variogram and those predicted by the regression line. Since the ratio of two semi-variances is equivalent to the ratio of two variances, the statistical F-test can be used as a linearity test in this case. The ratio of semi-variogram points to regression line points is compared to a threshold that is determined by an F-distribution and the degrees of freedom in the samples used to calculate the variances. Since semi-variograms are typically calculated from very large elevation data sets, such as high density DEMs, very slight changes in semi-variance are statistically significant. For example, for a 200X200 DEM, a difference of 2.3% between predicted semi-variance and observed semi-variance

is significant at the 99% level. Therefore, use of the F-test gives better results than conventional regression statistics because it takes into account the size of the elevation difference populations.

5.4.4 Determination of scaling properties associated with each band

The scaling properties associated with each band are characterized by their fractal dimension D, calculated from regression of semi-variance vs lag in the original semi-variogram profile, not in the line image, and the equation (modified from Schroeder, 1991):

$$H_D = E + 1 - \frac{m}{2} \tag{5.8}$$

Where, H_D is the fractal dimension, E is the number of Euclidian dimensions in which the fractal is embedded, 2 for surfaces and 1 for profiles, and m is the slope of the scaling band in the semi-variogram profile.

Omnidirectional mapping of the fractal dimension in 2D semi-variograms

The automated identification of linear bands and calculation of associated fractal dimension is especially useful for the analysis of 2D semi-variogram surfaces where it allows for the processing of all semi-variogram profiles in a semi-variogram surface. The first step is to extract profiles in all directions from 0° to 180° along the semi-variogram surface. Profiles are extracted by sampling the semi-variance surface at fixed lag intervals along a vector with a given direction and origin at the surface centre. The 0° direction is defined as being parallel to the positive x axis. For most samples, sample points are located between pixels in the semi-variance surface, and cubic spline interpolation was therefore used to obtain accurate semi-variance values. For this work, the number of samples in each profile is set to the required binary image size. Also, profiles were extracted in increments of 2° in order to study surface anisotropy at high angular resolution. Automated band identification is carried out on each profile, thus yielding band extent and fractal dimension for all bands in all profile directions.

The result is plotted as a sparse surface giving H_D vs. log(lag) vs. direction where a linear band is present. A gap is left in areas where semi-variogram profiles are curved. This type of graph is called a fractal dimension map (figure 5.2).

5.4.5 Testing of the algorithm

The algorithm was tested with 90 profiles generated with known slopes and known break points thus simulating the 90 profiles extracted from a semi-variance surface with increments of 2°. Each test profile had 2 sections. The first section was a linear band with a slope increasing linearly from 1 to 2 as a function of direction, from 0 to 178°. Also, the length of this linear band was made to increase linearly from 1.2 orders of magnitude to 2.1 orders of magnitude as a function of direction. After the breakpoints, semi-variance was made to increase as a square root function originating at the break point. This curve was chosen because it is characterized by an initially high curvature which tapers off and becomes nearly linear thus testing the algorithm's tolerance to curvature.

Test results, shown in figure 5.3, were excellent. The algorithm determined the slope break points with an error no greater than 2 pixels. This error was always an underestimation of band length. A regression of detected slope vs actual slope for directions gave perfect results: a 1 to 1 correlation, no bias and with an R^2 value of 1.0. This result is not surprising since band length was never overestimated and slope values are calculated with regression of semi-variance vs lag in the initial profiles which were constructed as perfect lines. Thus, the validation test indicates that the algorithm can precisely identify slope break points. In the curved sections, the algorithm systematically distinguished the initial portion of the curved section from the linear sections. However, short linear bands were detected approximately 0.5-0.7 orders of magnitude after the slope break point. This result shows that the algorithm does have a slight tolerance to curvature which justifies the need for the statistical testing phase.

This test also shows that the algorithm performs as expected and is capable of reliable identification of linear bands in semi-variogram profiles.

5.5 Discussion

5.5.1 Artefacts in the fractal dimension map

Examination of figure 5.2 reveals that the fractal dimension map has arch shapes at low lags. These features are artefacts resulting from the discreet nature of the semi-variogram surface and they should not be interpreted. The spacing of pixels along a Cartesian grid causes the distance between neighbouring pixels to be a function of direction. The first semi-variance sample at a direction of 0° (defined as horizontal) is at a distance of 1 pixel from the centre pixel. However, for a direction of 45° the first sample is at a distance of $\sqrt{2}$ pixels from the centre. Therefore the lag distance for the first semi-variance sample is a function of direction varying from 1 to 1.41. Whilst interpolation is used to obtain profiles sampled on identical lag axes, extrapolation of the profiles to 1 pixel gives very poor results. Therefore at low lags, for profiles where the first sample is further than one pixel, there is a gap in the data. On the fractal dimension map in which the lag axis is logarithmic, this gap reaches a maximum value of $\log(1.41) = 0.15$ for directions 45° and 135°. It should be noted that this arch shaped artefact will only appear in the fractal dimension map if a linear band extends to the lowest lags.

5.6 Application of fractal dimension maps to DEM quality analysis

The usefulness and advantages of the fractal dimension map will be demonstrated by applying them to the quality analysis of the DEMs presented in figures 4.4 and 4.5. These DEMs were derived from a cost-effective close range photogrammetry methodology described in chapter 4. This method uses a conventional 35mm film camera and an off-the-shelf commercial scanner for digitisation of images. DEMs were then generated using the OrthoMax module of ERDAS Imagine software which allows for automated stereo matching. In order to assess the type of error present in the DEMs, an analysis of the sensitivity of DEM quality to the number of photo-control points used in the DEM generation process was carried out. DEMs were therefore generated with 3 photo-control points and then with 20 photo-control points. Whilst chapter 4 showed that scaling analysis can be used to assess DEM quality and gain a better understanding of the type of error present in the DEM, this paper uses conventional 1D methods to analyse 2D semi-variograms. In the present paper, the fractal dimension map was applied to examine the scaling properties of the DEMs in chapter 4 in a more thorough and objective manner.

Examination of the fractal dimension maps for 3 gcp DEMs (figure 5.4) demonstrates the high information contents of the fractal dimension maps. For cases RSM1 and RSM3, figure 5.4 shows, at high lags, irregular bands of high fractal dimension which indicate the presence of noise at scales of 10 to 100 mm. Figure 5.4 also shows that this noise is not isotropic i.e. fractal dimension and band extent vary significantly as a function of direction. The fractal dimension map for RSM4 shows strong anisotropy of fractal dimension which is a result of the orientation of the boulder in the DEM (RSM4). Examination of figure 5.5 shows the effect of increasing the number of control points used in DEM generation. The removal of noise caused by the addition of control points can be seen to reduce the fractal dimension of the DEMs. Furthermore, the irregular

bands at high lags have largely been eliminated and the extent of the primary bands at lower lags has been increased. In figure 5.5, case RSM1 shows the presence at low lags of bands with a fractal dimension near 2.5. This indicated that at small scales, near-random noise is present. This effect can be qualitatively seen by examining figure 4.4 a). Therefore, the fractal dimension map has allowed for a quantification of this small scale noise. Furthermore, the fractal dimension map shows that this small scale noise is not isotropic and systematic for all directions. The fractal dimension map is therefore much better suited to quality analysis than 1D semi-variogram analysis techniques. Variations in fractal dimension and band extent as a function of direction allow for a quantification or anisotropic effects, band extent values allow for a quantification of the scale at which processes operate and the fractal dimension allows for a quantification of the randomness of these processes.

5.7 Conclusion

The fractal dimension map allows for an objective, rapid and thorough assessment of the scaling properties of a surface. Once a semi-variogram surface has been calculated, construction of the fractal dimension map plots on a single graph both fractal dimension and band extent as a function of lag and direction. The fractal dimension map therefore gives much more detailed information about a semi-variogram surface than previous methods of semi-variogram analysis. The additional information given by this new method has potential applications in any field which uses semi-variograms for the purpose of scaling analysis.
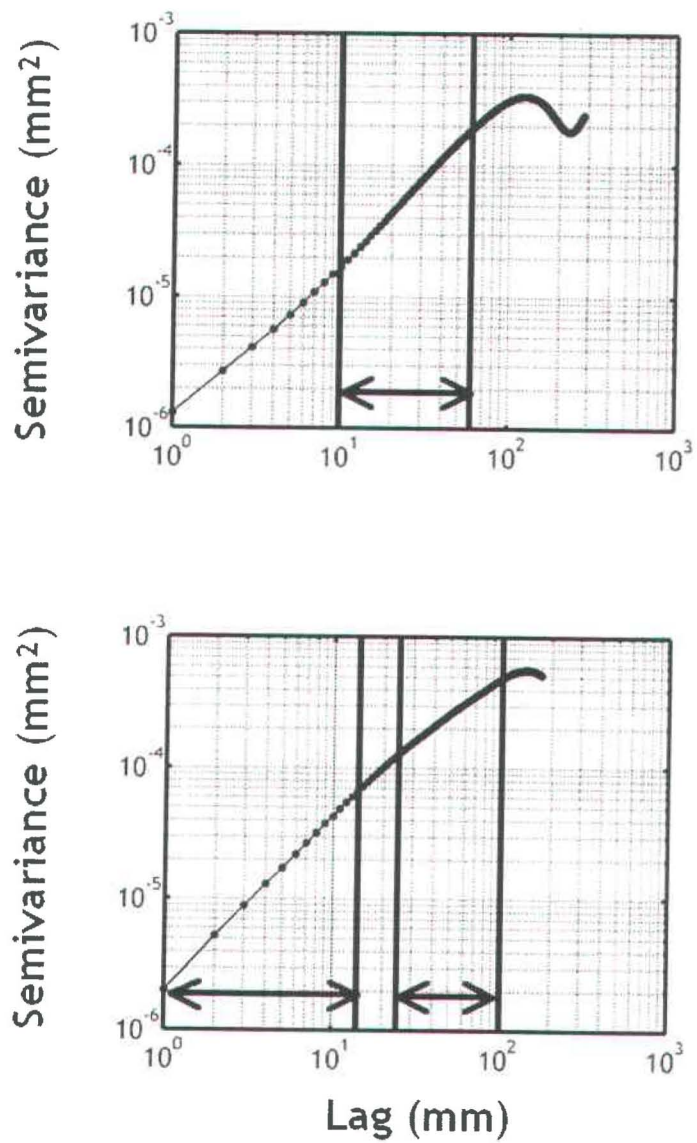
Figure 5.1. Example of two semi-variogram profiles.
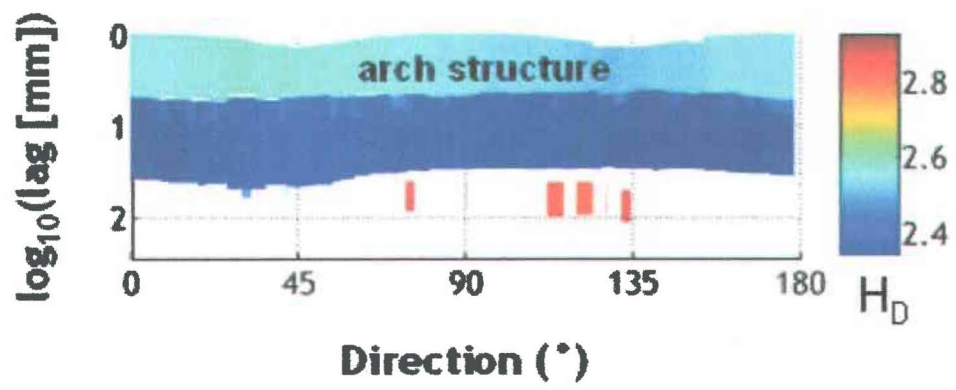
Figure 5.2. Example of a Fractal dimension map. Fractal dimension D is plotted as a function of direction and log(lag).
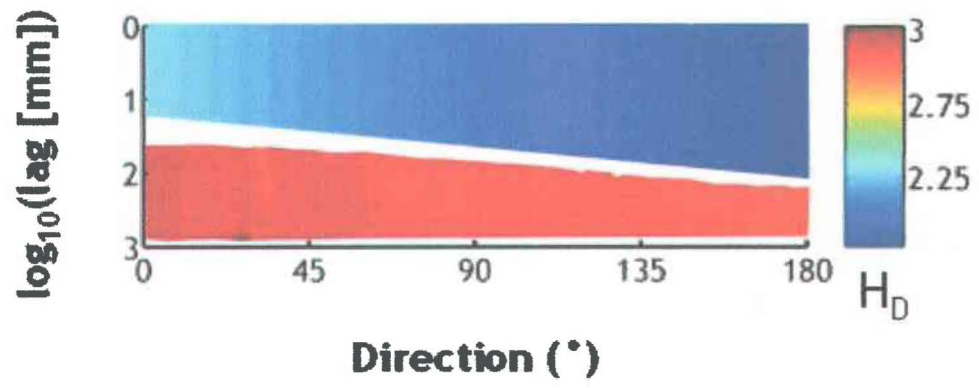
Figure 5.3. Fractal dimension map for the artificial test surface.
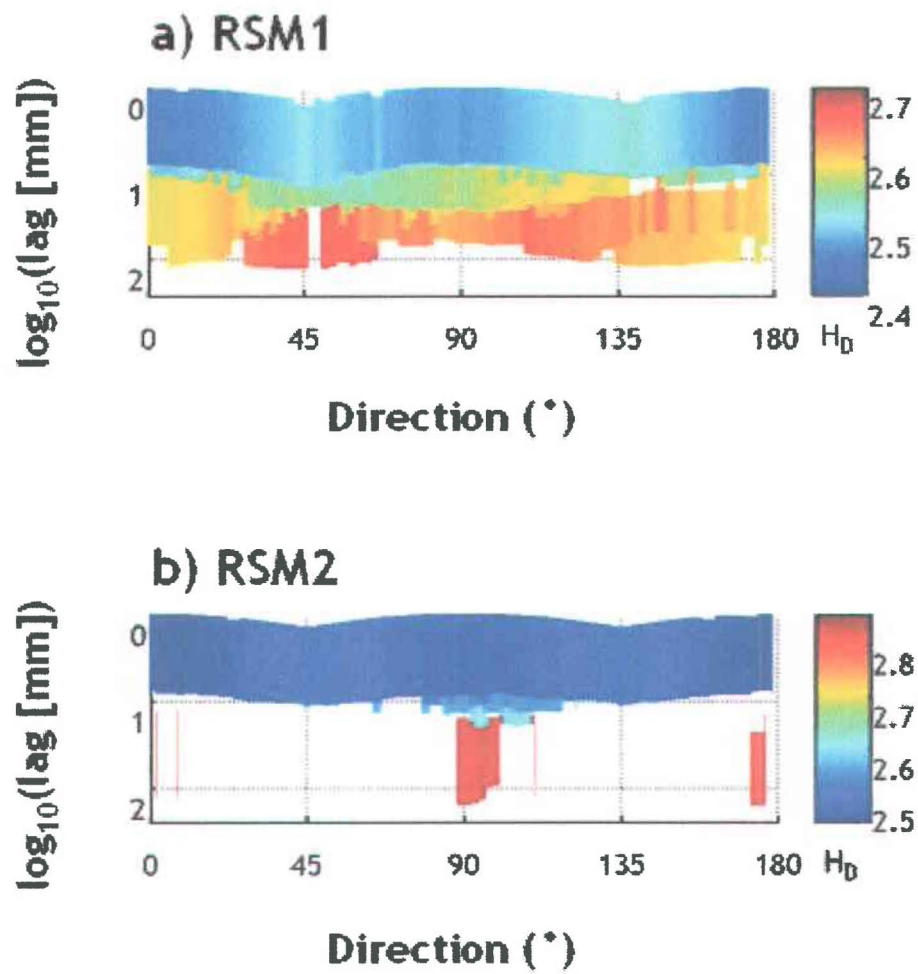
Figure 5.4 Fractal dimension maps for 3 gcp dems presented in figure 4.4.
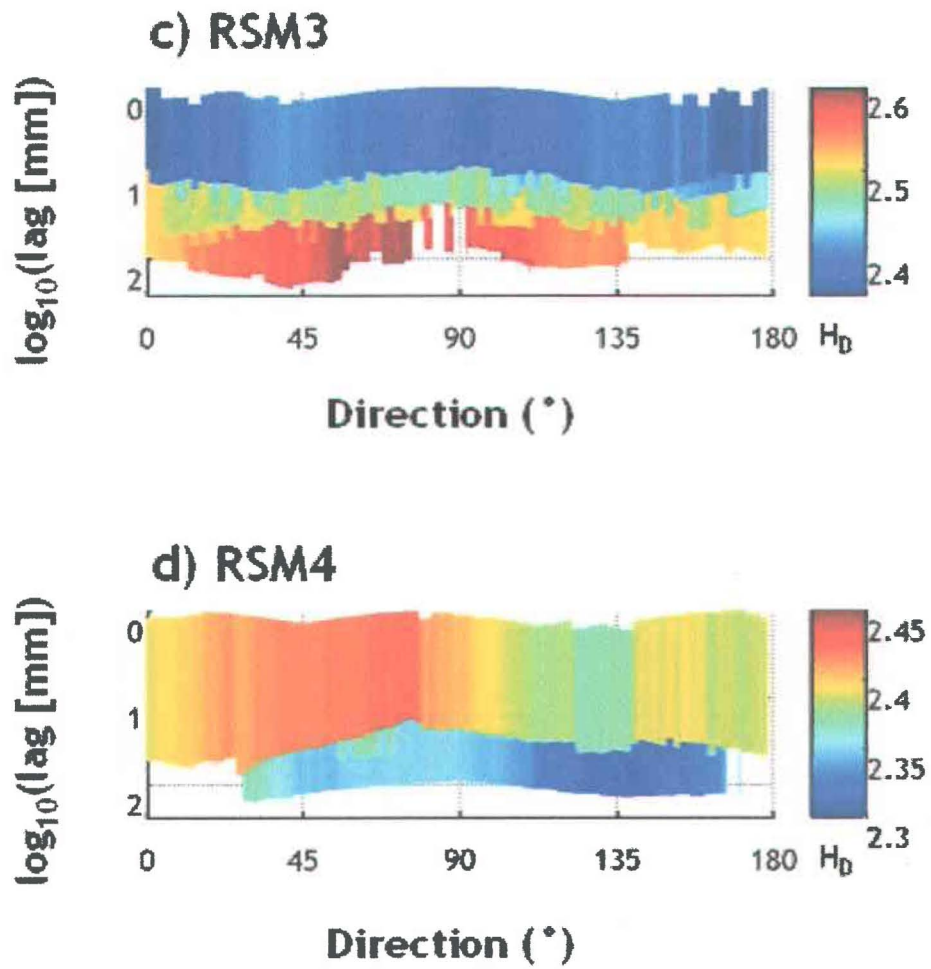
Figure 5.4 (continued) Fractal dimension maps for 3 gcp dems presented in figure 4.4.
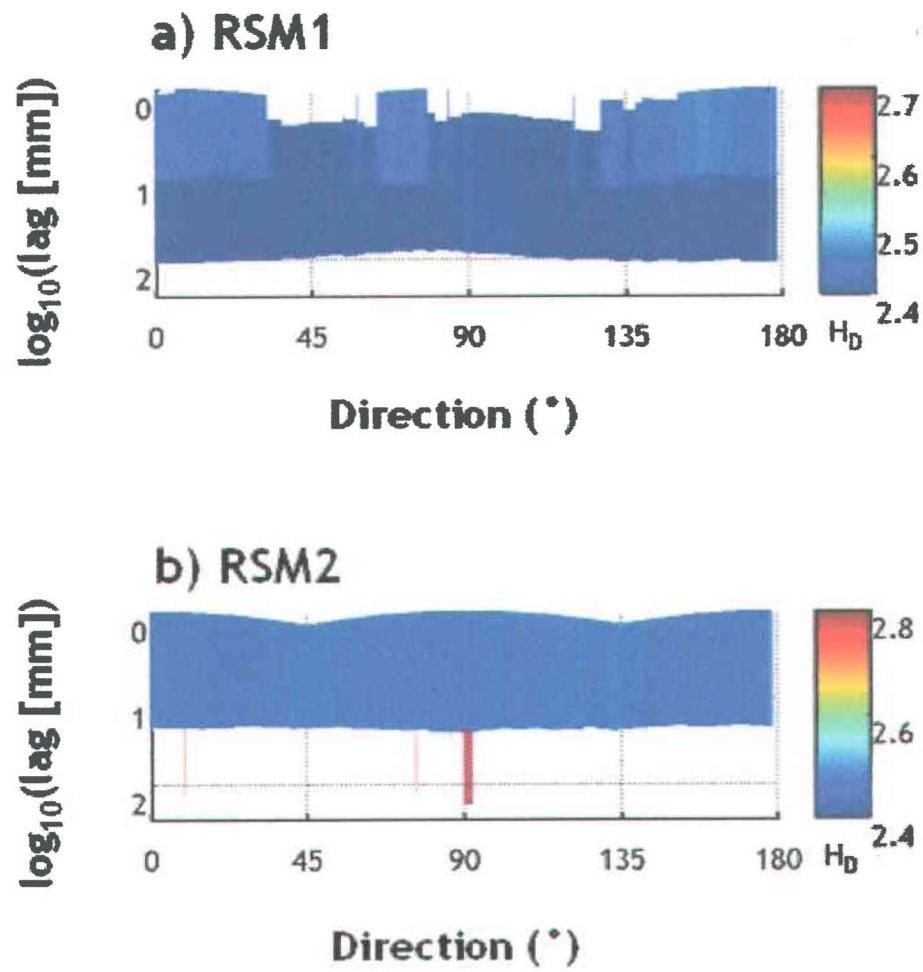
Figure 5.5 Fractal dimension maps for 20 gcp dems presented in figure 4.5.
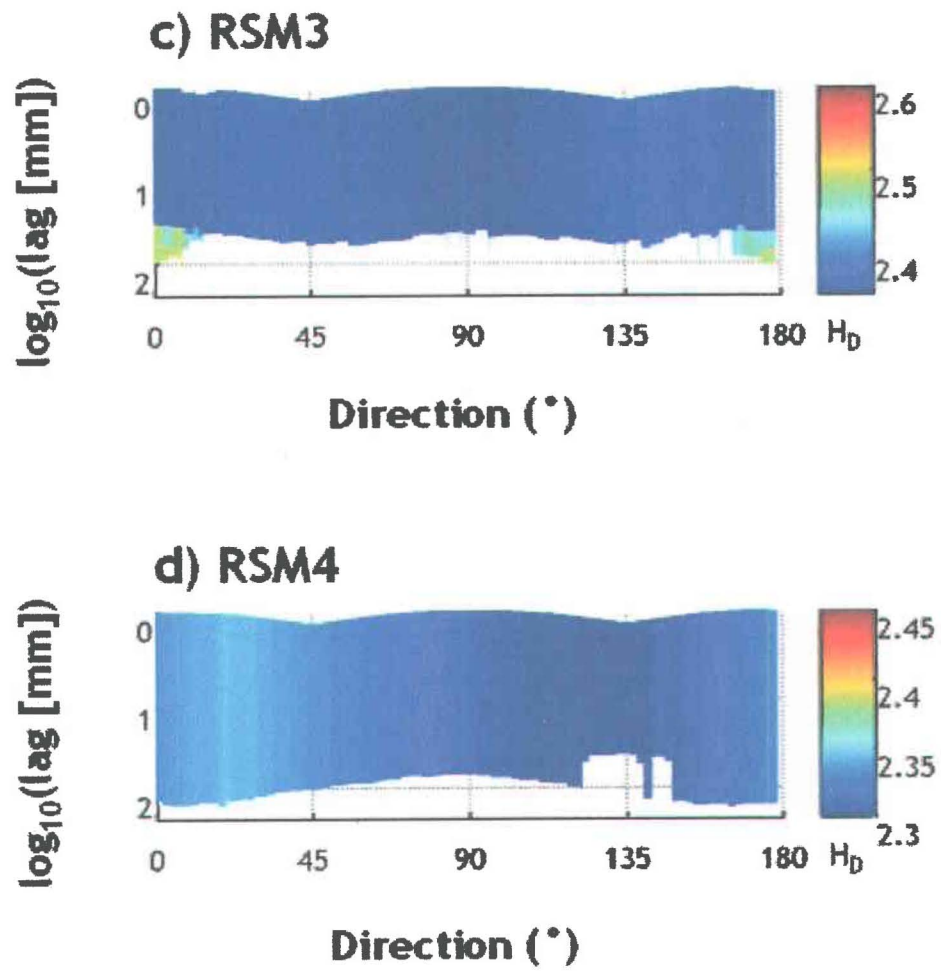
Figure 5.5 (continued)   Fractal dimension maps for 20 gcp dems presented in figure 4.4.

Chapitre 6: New methods for the quantitative analysis of stream gravel bed surface structure

New methods for the quantitative analysis of stream gravel bed surface structure

Patrice E. Carbonneau[1†]

Normand E. Bergeron [1]

Stuart N. Lane [2]

1 Université du Québec, INRS-ETE, 880 chemin Ste-Foy, CP 7500, G1V 4C7, Québec, Canada, phone: (418) 654-2647 fax: (418) 654-2615 email: pcarbonn@nrcan.gc.ca

2 School of Geography, University of Leeds, Leeds, UK

*Contribution to the program of CIRSA (Centre Inter universitaire de Recherche sur le Saumon Atlantique)

† Corresponding author

6.1 Résumé

La description des lits de gravier à l'échelle des grains est généralement limitée à la courbe granulométrique du lit. Par contre, des aspects autres que la taille des grains doivent être quantifiés afin d'avoir une description complète des lits de graviers. Cet article présente des nouvelles méthodes et concepts permettant la quantification de l'agencement des particules dans un lit de gravier. Tout d'abord, il sera démontré que les méthodes de quantification des structures de graviers basées sur les estimations visuelles sont d'une fiabilité limitée. Ensuite, le traitement d'images est employé pour obtenir une description quantitative de l'agencement des particules qui inclus des structures connues telles que l'imbrication et l'enchâssement. Ces méthodes ont été développées pour améliorer les méthodes actuelles de quantification de l'habitat hivernal disponible pour les saumons juvéniles en milieu fluvial. Cependant, ces méthodes sont applicables dans le contexte de toute étude qui nécessite une quantification plus approfondie des propriétés physiques des lits de graviers.

6.2 Abstract

Quantitative descriptions of fluvial gravel surfaces are often limited to grain size distributions. However, aspects other than size distributions can be of interest. In some situations, this may warrant the development of new formal quantitative methods for describing gravel surfaces. In this paper, the authors propose new methods for the quantification of particle arrangement on gravel surfaces. We begin by demonstrating that quantification methods of gravel structure based on visual estimation of surface properties are of limited reliability. Digital image processing is then applied in order to obtain quantitative descriptions of particle arrangement on gravel surfaces. The methods presented here were developed for the purpose of improving current methods for the quantification of the physical habitat of juvenile salmon by allowing for a description of bed material which includes particle arrangement. However, these methods are not application specific and could have widespread applications in other fields of fluvial geomorphology which require quantitative measurements of gravel bed structure.

6.3 Introduction

Field methodologies for the measurement of grain size distributions of fluvial gravel beds are well established (Church *et al.* 1987). Additionally, photography and digital image processing have been applied to the problem of grain size measurement in the field (Butler *et al.* 2001, Whitman *et al.* 2003). As a result of this focus on particle size, grain size distribution is the physical parameter most commonly used to describe fluvial gravels. However, research in a wide range of fields has established the importance of particle arrangement, hereafter termed surface structure, to a number of problems related to gravel bed rivers. For example, it is generally recognised that interlocking, imbricated particles require a greater shear stress to mobilize (Allan and Frostick 1999). Furthermore, the degree of roughness of gravel river beds has been qualitatively related to particle imbrication by Robert (1991a). Another example involves salmonid habitat requirements. Studies of juvenile salmonid behaviour have established that during winter months, juvenile salmons seek shelter in the voidspaces of fluvial gravels (Rimmer *et al.* 1984, Gregory and Griffith 1996). Therefore, surface structure is a relevant parameter to juvenile salmonid habitat characterization. Despite the fact that surface structure is of interest, existing methods for quantifying surface structure are scarce and difficult to apply (Bunte and Abt 2001).

A complete description of surface structure would require detailed knowledge of the exact shape and dimensions of each particle and their exact position within the gravel bed. Given the complexity of gravel bed rivers, this is impossible. However, practical descriptions of surface structure may still be possible. Two key concepts found in the literature may be used as a basis for a description of the structural characteristics of gravel beds: particle imbrication and cobble embeddedness. These are the focus of this paper.

Cobble embeddedness is described as the partial burial of coarse clasts by fine particles (Bunte and Abt 2001). In this case, 'fine particles' generally refers to sand and fine gravel. Bunte and Abt (2001) present methods for the quantitative measurement of cobble embeddedness which consider both individual clasts and surfaces. Methods for the measurement of individual clast embeddedness all rely on the establishment of a regular sand surface datum. This can be impractical in the field given the irregular nature of gravel beds. Also, surface based methods described in Bunte and Abt (2001) work by counting the number particles that are completely above the sand datum. Therefore, this method cannot take into account the partial burial effect described in the definition. The current definition of cobble embeddedness is qualitatively clear but the concept remains difficult to quantify.

Particle imbrication may be defined as a shingle-like deposit in which the upstream particle partially overlaps its downstream neighbour with clasts dipping in the upstream direction (Bunte and Abt 2001, Jain 1990). Whilst it is generally understood that the degree of imbrication is equivalent to the degree to which particles overlap each other, no quantitative method was found in the literature allowing for the measurement of imbrication.

The preceding definitions of imbrication and embeddedness stress two important characteristics of gravel bed surfaces which determine imbrication and embeddedness: the overlapping of neighbouring particles and the presence of sand particles on the bed surfaces. Imbrication is present when coarse particles of similar sizes overlap in a shingle like structure. Imbricated bed surfaces therefore have a low coverage of sand particles. Embedded cobbles share a common characteristic with imbricated cobbles in that they are also overlapped by neighbouring particles. However in the case of embeddedness, sand overlaps and partially buries coarser particles. This suggests that the presence of imbrication or embeddedness on a gravel bed reflects the state of two

fundamental variables describing structure: particle overlap and the presence of sand particles on the surface. These two variables could therefore be used as quantitative variables describing gravel bed structure.

Visual observations could potentially be used to describe particle overlap and sand coverage (Whitman *et al.* 2003). Such observations can also serve as a conceptual basis for a more quantitative approach. Figures 6.1a and 6.1b show surfaces that can intuitively be classified as free of superficial sand and as having an important amount of superficial sand, respectively. This causes the cobbles to be unembedded in 6.1a and embedded in 6.1b. Likewise, figures 6.1c and 6.1d show heavily overlapping and lightly overlapping surfaces both free of sand particles, respectively. In this case the heavy particle overlap and absence of sand has caused imbrication in 6.1c and the absence of both sand and particle overlap in 6.1d causes an unimbricated structure. In order to quantify such observations, digital image processing can be applied to gravel surface images to replace visual observations with quantitative measurements of particle overlap and surface coverage by sand particles. This paper begins with quantitative tests of the reliability of visual observations applied to the quantification of gravel surfaces. This is followed by the description of digital image processing methods capable of quantifying particle overlap and sand coverage.

6.4 Methods

6.4.1 Reliability tests for visual observations

Before proceeding with quantitative descriptions of particle overlap and sand coverage, the reliability of visual estimates for these variables was tested. A series of 30 test images was assembled. The first 20 images consisted of 20 X 20cm surfaces with superficial sand covering 5% to 90% of the surface. The other 10 images were a series of 40 X 40 cm cobble images with various degrees of overlap. A group of 10 subjects were asked to estimate the coverage of superficial sand and to rank cobble images in order of increasing particle overlap.

Ground truth values for the sand images were obtained manually as described in section 6.4.3 and compared to visual estimate results. The overlap estimates were first analysed with bivariate pearson rank correlations in order to examine the similarity of the rankings made by different observers. Bivariate pearson correlations were then applied to examine the similarity of observed overlap rankings and quantitative rankings obtained from the image processing methods of section 6.4.4.

6.4.2 General considerations for quantitative methods

The quantitative methods presented in this paper require images of exposed gravel beds as raw data. The quantification of sand coverage works with grey scale imagery and quantification of particle overlap requires colour imagery. The resulting images should have a pixel size roughly equivalent to the smallest particle on the bed. Either a film or a digital camera may be used. If a film camera is used, height of the camera with respect to the study surface can be adjusted in order to sample the desired surface dimensions and during image scanning, appropriate scanning resolution can be selected to achieve the required pixel size within the constraints of the maximum scanning density available. If a digital camera is used, careful consideration must be given to camera height during image acquisition since digital cameras have a fixed resolution. Additionally, the study surfaces should be dry. The methods are therefore currently limited to dry exposed gravels.

6.4.3 Quantification of sand coverage

Basic grey level segmentation generally gives poor results on highly complex images and texture based segmentation gives better results (Haralick *et al.* 1973, Conners *et al.* 1984). Given the complex nature of fluvial gravel images, the sand quantification procedure is carried out with texture based image segmentation. The accepted definition of image texture is: 'an attribute representing the spatial arrangement of the grey levels of the pixels in a region'

(IEEE 1990). Texture based segmentation operates by transforming a raw image into a textural measure image where regional texture information is represented as grey levels. Image texture is evaluated with the co-occurrence matrix. The co-occurrence matrix is constructed by comparing all image pixels separated by a distance D at direction V. The i, jth element of the co-occurrence matrix **P** for an image is the number of times that grey levels i and j occur in two pixels separated by distance D and direction V divided by the total number of pixel pairs (Castleman 1996). The co-occurrence matrix therefore is of size (G,G) where G is the number of grey levels in the image, usually 256. To make the co-occurrence matrix faster to calculate, the number of grey levels is generally resampled to 8, 16 or 32. Therefore, co-occurrence can quantify how many pixels of similar grey levels are neighbours. Once the co-occurrence matrix is calculated, textural features may be derived to reduce the information in the co-occurrence matrix to a single value (Harralick et al. 1973; Conners et al. 1984; Castleman 1996). For example, entropy is defined as:

$$E = \sum_i \sum_j P_{ij} \log P_{ij} \tag{6.1}$$

where E is entropy and P is the co-occurrence matrix. Areas of high entropy have low texture and are mapped to light grey levels.

To produce a textural measure image, the co-occurrence matrix is calculated for each window of size (W,W) in the original (M,N) image. For each co-occurrence matrix, the textural measure is calculated and the information is represented as a textural image of dimensions (M/W, N/W). Therefore in the texture image, the i, jth pixel is the textural measure value for the co-occurrence matrix of the region [i:i+W-1; j:j+W-1] in the original image. Basic grey level thresholding can then be applied to segment objects in the image based on textural measures.

Figure 6.2 shows an example of an image and its associated textural entropy image. The textural entropy was calculated with co-occurrence matrix of size 20X20. Automated grey level thresholding, following Otsu's method (Otsu,

1979), was then applied to the texture image to separate the dark high texture sand and the low texture rocks. A despeckling routine, based on binary morphology operations (Castleman, 1996), which removes objects smaller than 10mm² was applied to clean up the segmented image. This routine operates by detecting all aggregated pixel groups and eliminating those with 10 pixels or less. The critical size was set to eliminate pixel groups which most likely correspond to fine gravel of 2-3 mm in diameter. Fine gravels are easily mobilized and contribute to embeddedness by burying low mobility coarse clasts. They should therefore be considered in the detected sand percentage. After segmentation and de-speckling, sand percentage is calculated as the ratio of 0s (sand pixels) to the total number of pixels.

The results are shown in figure 6.3a. Figure 6.3 illustrates the improved performance of texture based segmentation by comparing the result of directly segmenting the original image and textural segmentation. In the segmentation of the original image, the despeckling routine was also applied to allow for a fair comparison. It can be seen that if the raw image is directly segmented, small particles with light grey levels pass the grey level threshold and create background noise.

6.4.4 Quantification of particle overlap

This method requires that the study surface be spray painted as a first step. After the image for sand coverage has been taken, paint is generously sprayed at an angle of 45° from vertical in all directions in order to insure that the voidspaces and overhangs exposed and/or open to the surface are painted. Paint colour should be close to one of the three primary colours in order to simplify the application of colour image processing. Once the paint is dry, the area of the study surface is measured. Rocks greater than 10mm are numbered, removed from the bed, placed on a black board (c-axis vertical), shielded from sunlight to obtain uniform illumination and finally, photographed. To obtain full coverage of

the whole surface of each rock, each clast is turned over and the black board is photographed again. This process is repeated until all rocks affected by paint have been photographed. Figure 6.4 shows an example of the resulting data with all three colour bands. In this case, a bright fluorescent orange spray paint was used. It can be seen that the orange gives high brightness levels in the red band, medium brightness in the green band and low brightness in the blue band. The high brightness contrasts in the red band simplifies the image processing operations required to obtain the final results.

The overlap quantification approximates the projected area of a clast on an image as equal to half the surface area of the clast. Whilst the projected area of a clast is not equal to it's total surface, the ratio of the projected areas of the upper and lower half of a clast will be equal to the ratio of surfaces if the c axis is symmetrical with respect to the plane defined by the a and b axis. Koster *et al.* (1980) demonstrated that no significant asymmetries exist in natural gravels which implies that the use of projected areas in this method should not introduce error.

The method operates by calculating, for each clast, the percentage of the total projected clast surface that is painted. Painted surface represents exposed area which is simpler to evaluate. Therefore, particle exposure percentage, equivalent to 100%-(particle overlap)%, shall be used from here on. The first step is the use of automated image segmentation to identify the individual rocks in the images. Basic image segmentation algorithms operate on 8 bit grey scale imagery (Harralick et Shapiro 1985, Castleman 1996). Since colour images are composed of three greyscale bands sampled in red, blue and green, only one of these bands will be used for image segmentation. The colour band most closely corresponding to the paint colour should be used for segmentation. In this case, the red band is used. Particle edges are identified with a 3X3 Sobel operator (Castleman 1996, Richards and Jia 1999). The presence of a black background

makes this basic operator very efficient by providing a uniform colour background which enhances contrasts between the rocks and the black board. After edge detection, binary morphological closure (Castleman 1996, Mathworks 2001) is used to transform detected edge pixels into closed continuous line. A flood fill algorithm is then used to fill the edges (Mathworks 2001). The result is a binary image where pixels with a value of 1 correspond to clasts (figure 6.5).

It may occur that some rocks in the image are not detected or their contours not defined correctly. The primary reason for this is lack of contrast between some or all of a given rock and the black background. It was observed that darker wet clasts from surfaces which were not completely dry are often not detected. The algorithm may be adjusted to be more sensitive but this may lead to oversegmentaion which typically results in the painted and unpainted parts of a given rock as being falsely identified as two distinct rocks. It was therefore decided to implement a semi-automated editing phase where the user manually defines the contours of undetected rocks. Depending on the moisture content in the bed and clast colour, 5 to 10% of rocks required editing.

After editing, the detected rock pixels may be labelled to create digital objects. This is an important step since groups of pixels become identified as being part a given rock which allows for the evaluation of certain properties separately for each rock. In this case, the properties of interest are the total number of pixels and the number of painted pixels. Segmented binary images such as shown in figure 6.2, are labelled based on connectivity considerations (Castleman 1996). A group of pixels is said to be 8-connected if their sides and/or corners are in contact. A group of pixels is said to be 4-connected if their sides are in contact. The use of 8-connection is therefore more appropriate if pixel groups of irregular shapes are to be created. The binary segmentation image is therefore processed to detect 8-connected objects and a label image is created. In this label image, all objects are numbered and all the pixels of a given object are set to the object

number. Pixels not corresponding to objects are set to zero. The label image, which is the same size as one of the bands in the original image, can therefore be used to carry out object based calculations. The label image is therefore used to define each clast and to count the number pixels in each clast.

Within each defined object/rock, pixel colour is used to establish the portion of rock that was painted. In digital imagery, colours are generally quantified in the RGB format (Red-Green-Blue). The colour of each pixel in the image is described as a linear combination of red, green and blue intensities. Colour digital images are stored in three bands with each band being associated to a colour. However, the RGB format is not appropriate for this work. In the RGB format, many colours that appear similar to the human eye are produced by varying two out of three colour components. This makes automated identification of painted pixels more difficult. An alternate colour format may be used to simplify the process. The HSI (Hue-Saturation-Intensity) colour format was designed to represent colour in a way that more closely resembles human perception (Mathworks 2001). This format still works with three components but it allows similar colours to be produced by varying only one component out of three. Shades of orange in the HSI format maintain low hue values, high saturation values and high intensity values. For the purpose of automated detection, the exact values must be determined based on the specific shade of paint that was used in the field. In this work, thirty 100 pixel areas were taken as training areas in the images for sites b), c) and d). Threshold values were set as the maximum hue, the minimal saturation and the minimal intensity. This yielded the following critical values: $H<26$, $S>200$, $I>200$. Once these boundaries are determined each rock is scanned and the number of coloured pixels can easily be counted.

In order to evaluate the percentage of clast surface covered by paint, the upper and lower faces of each rock, must be associated. Manual identification is used in order to identify lower and upper face images for a given clast and link the

binary objects for each face. Once both faces of each clast are associated, the total particle overlap may be calculated for each clast as the percentage of unpainted pixels to total pixels in each given clast. In order to quantify the particle exposure of each study surface with a single number, the 84th percentile value of the exposure distribution for all clasts in the study surface is used.

6.5 Application and validation of quantitative methods

The sand coverage quantification method was tested on 20 small 20cm X 20cm sandy gravel surfaces also used as test images for visual estimates. These surfaces were selected for increasing sand superficial content. Prior to running the detection algorithm on each surface, ground truth values of sand coverage for each image were established by manually tracing the outline of sandy patches in each image. This work was done with a graphic user interface programmed in the MATLAB environment. Ground truth values were then compared to visual estimates and to detected values obtained by the automated routine.

The particle overlap method was applied to the four sites shown in figure 1 and also to the ten sites of exposed cobbles used in visual estimate tests. These surface were free of sand with median grain sizes for these surfaces ranges from 32mm to 164mm. Success of the paint identification was established by selecting 30 painted clasts which ranged in size from 3.2cm to 34cm (b axis) and then manually establishing paint contours on the image with the MATLAB script used to validate sand identification. This allowed for a manual calculation of the particle exposure for each image.

6.6 Results

6.6.1 Visual estimates

Visual estimate for sand coverage were found to be better than expected with a mean error of 6%, a mean absolute error of 11% and a standard deviation of error of 9%. However, close examinations of the results showed that in the case

of the nine images with ground truth sand coverage ranging from 5% to 52%, both mean error and absolute mean error were 19%, a systematic overestimation, with standard deviation of error of 8%. For the other eleven images, with ground truth sand coverage ranging from 64% to 90%, mean error dropped to 4%, mean absolute error was 9% and standard deviation was 8%.

Visual estimates of particle overlap were found to be unreliable. All users agreed on the most overlapping surface but rankings for the other 9 surfaces were very variable. Bivariate pearsons rank correlations ranged from −0.65 to 0.97. Two of the 10 subjects gave similar answers, giving a correlation of 0.97 but for the other subjects maximum correlation was 0.48. In the case of five users, the pearsons correlations were negative indicating that some surfaces could be perceived as weakly overlapping by some and moderately overlapping by others. The mean bivariate correlation was 0.01 with a standard deviation of 0.4.

6.6.2 Quantitative method results

The comparison of automatically detected (d) versus ground truth (gt) sand coverage data was excellent. The relationship is $d=1.01gt-0.96\%$ with an R^2 value of 0.93 (figure 6.6a). Here, d is the value detected with automated processing and gt is the ground truth value obtained from manual tracing.

The paint identification algorithm was found to work precisely and accurately. When comparing manually calculated particle exposure and automatically calculated particle exposure, the relationship is $d= 0.96gt-0.35\%$, $R^2=0.95$. Here, d, the detected value, is automated particle exposure and gt is manual ground truth particle exposure. There is a very slight underestimation but overall the automated identification of painted surfaces is reliable. Frequency distributions for particle overlap results for the examples of figure 6.1 are given in figure 6.7. The 10 surfaces used for visual estimation tests were processed and ranked following the 84th percentile of the particle overlap and these results were tested against visual observations for rank correlations. Pearsons

correlation coefficients ranged from −0.564 to 0.236 with a   mean value of −0.1 and a standard deviation of 0.35.

6.7 Discussion

6.6.2 Visual methods

Visual estimate results in the case of sand coverage show that such procedures should be treated with caution. Error was found to be a function of the sand coverage. This is possibly due to the fact that in cases with high sand coverage, the observer can easily asses the surface percentage of large contiguous zones of sand. However, in the case of lower sand coverage percentages, the sand area is not contiguous with sandy patches being separated by clasts. In this case, it seems that the visual estimates are more prone to error. If applying visual estimates to classify surfaces for sand coverage, the width of a class, in % sand coverage, should be greater than the error of the estimates. Since error can be as high as 19%, such methods could therefore be used to classify surfaces into a maximum of 4 classes of increasing sand coverage.

The results for particle overlap clearly show that this method is very sensitive to the observer. The high standard deviation of rank correlation coefficients shows that different observers do not rank the surface particle overlap in a similar manner nor do they agree with the proposed quantitative ranking. This suggests that visual methods are not reliable for the descriptions of highly complex and irregular phenomena such as the imbrication and particle overlap of fluvial gravel surfaces.

6.7.2 Quantitative methods

The results of the automated sand coverage detection were very satisfactory and the procedure was deemed reliable. Close examination of the results of particle exposure analysis reveals a probable bias (figure 6.7). Figure 6.7 shows that frequency distributions of particle exposure all have a mode at low exposures.

However, some distributions are more skewed towards high exposures than others. The modal value is the result of a methodological bias rather than a reflection of bed structure. As stated earlier, during the data collection all clasts greater than 10mm affected by paint were photographed and their overlaps measured. Clasts which are deeper within the bed will inevitably be less exposed even if the bed is not structured which makes the low exposure part of the distribution less meaningful. However, the skewed part of the distribution reflects the gravel structure. A positive skeweness in the exposure distribution indicates the presence of clasts with high particle exposure values. These will likely be surface clasts who were heavily exposed to spray painting. However, the absence of a skew in the distribution indicates most clasts, even the surface clasts, were sheltered from paint by overlapping neighbouring clasts. The skewed part of the distribution is therefore more representative of the surface clasts. Characterization of surface particle exposure with the 84th percentile value of the particle exposure distribution was found to yield physically significant results which were in accordance with qualitative visual observations.

Quantitative validation of the particle overlap method was greatly hindered by the lack of well established methods. However, the success of the paint detection algorithm indicates that reliable information about intergranular organisation and relative particle positions is obtained. Since this is the first quantitative method aimed at studying imbrication, it could therefore be used as a standard against which to test future imbrication quantification methods.

An advantage of these digital image processing based methods is the possibility of covering large surfaces. Although the examples presented here were of small scale, data collection for one study site requires less than thirty minutes. It is therefore possible to characterize a large number of study sites in a relatively short time. Large datasets for particle exposure and sand coverage would allow for comparison of surface structure along the long profile of gravel rivers and

would also allow for quantitative cross-river comparisons. Additionally, using hand held GPS systems, study sites could be georeferenced and surface structure data could be integrated into geographic information systems (GIS).

6.8 Conclusion

Field observations of waterworked gravel surfaces immediately reveal the complexity of their organisation. Whilst imbrication and embedded beds have been described for many years, an efficient and quantitative measure of characterizing these structures has been lacking as a result of this complexity. The procedure proposed in this paper aims to provide more rigorous methods for the quantitative characterization of fluvial gravel surface structures.
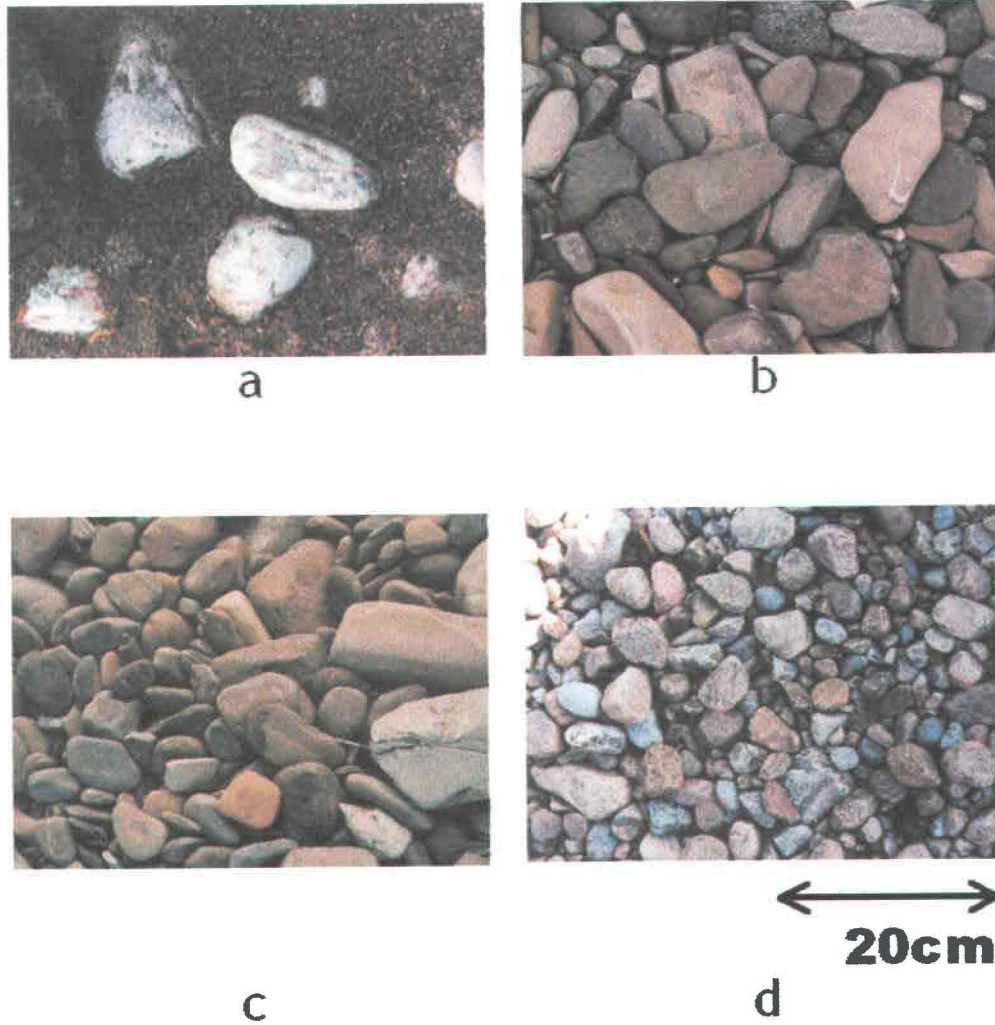
Figure 6.1. Examples of bed surface structures also used as study sites.

20cm

a   b
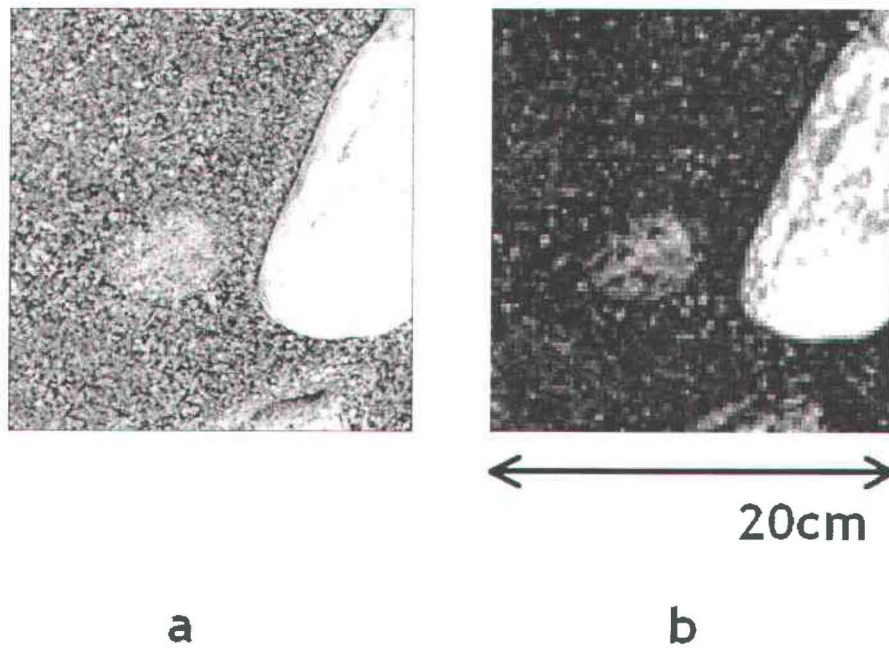
Figure 6.2. A) Raw image of sand covered surface B) Texture image associated with A).
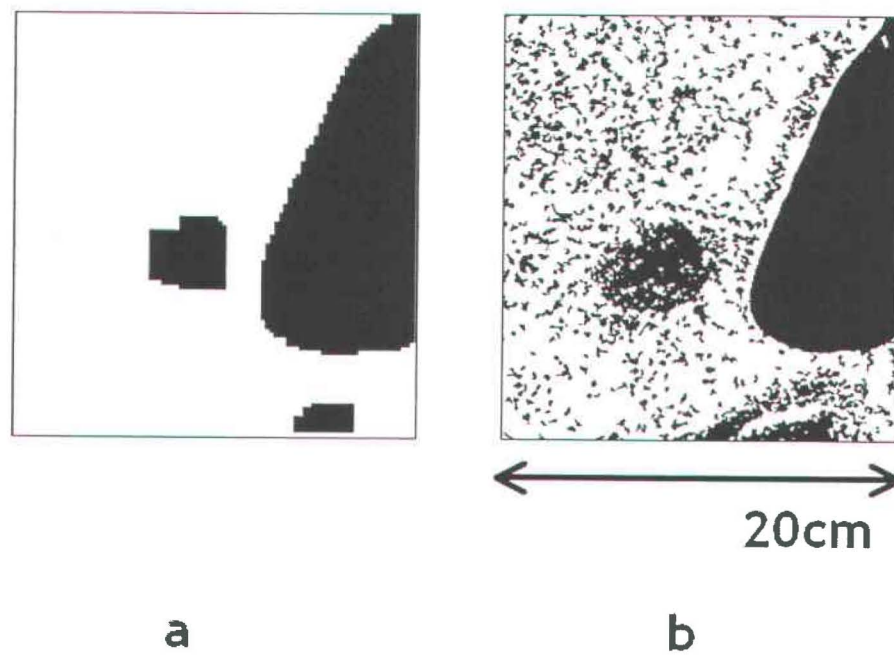
Figure 6.3. A) binary segmented image obtained with thresholding of the texture image. B) binary segmented image obtained with thresholding of the raw image.

A) Colour image

B) Red band

C) Green band

D) Blue band

20cm
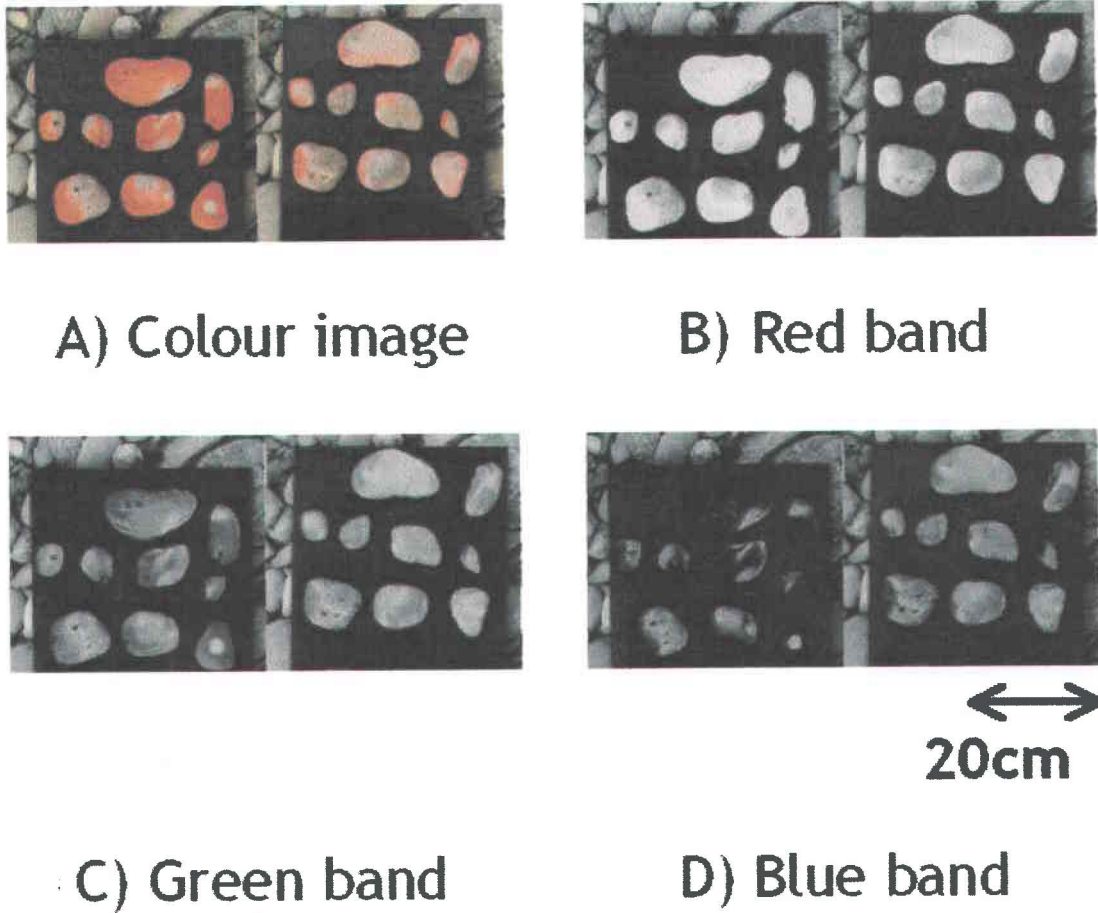
Figure 6.4. Colour image used for particle exposure analysis. A) is the raw color image and B, C and D are the decomposed colour bands.
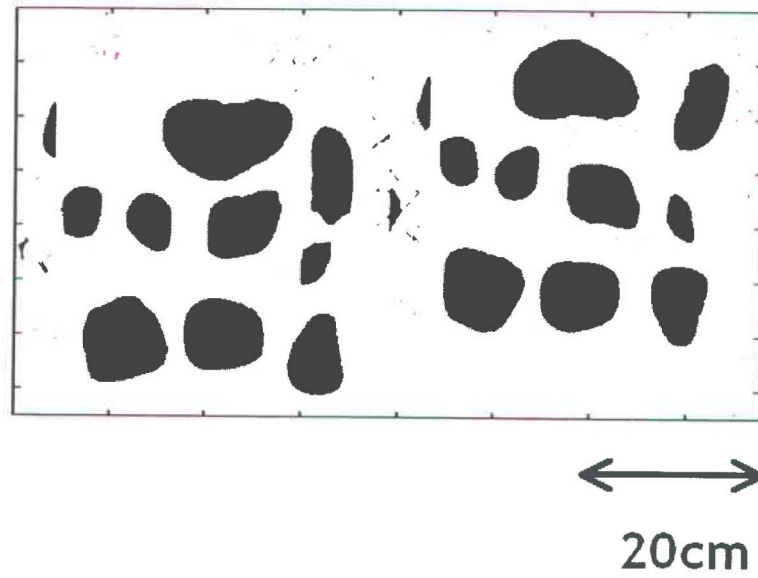
Figure 6.5 Binary segmented image used for clast identification in particle exposure analysis.
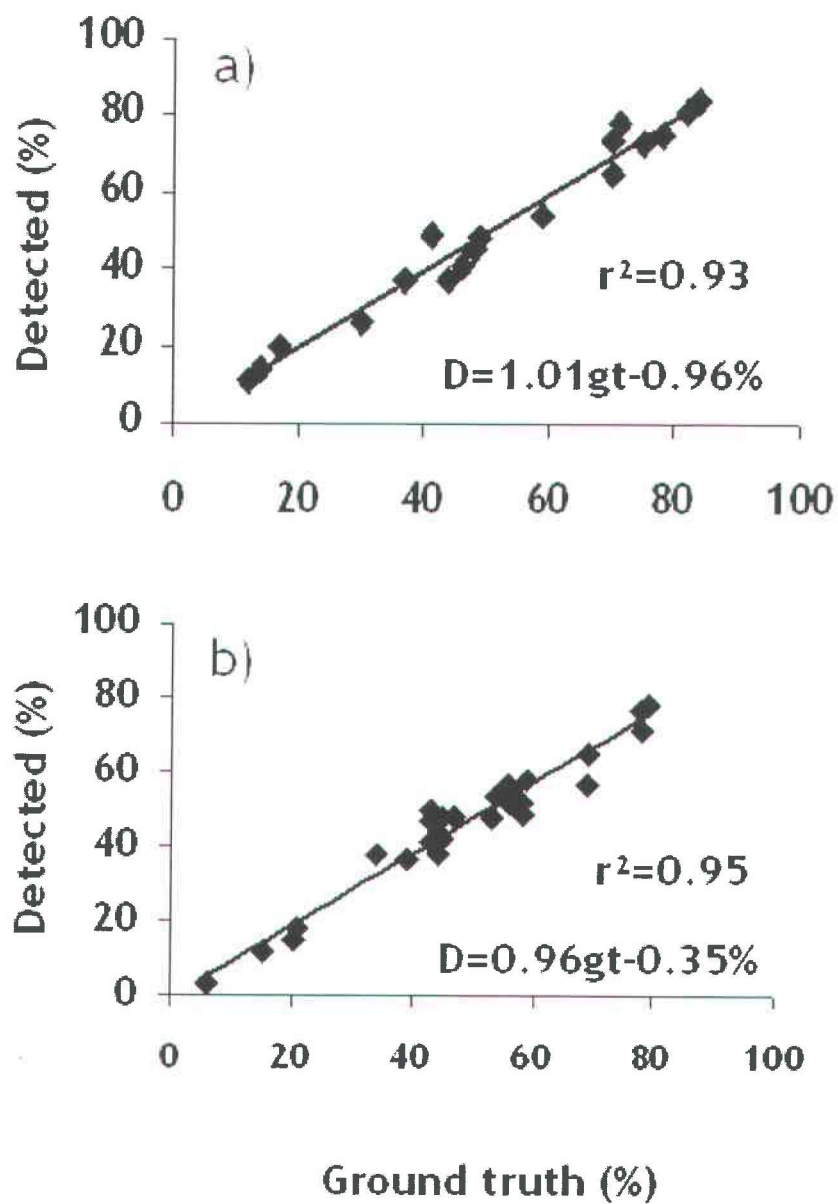
Figure 6.6. Validation results. A) sand identification. B) paint detection.
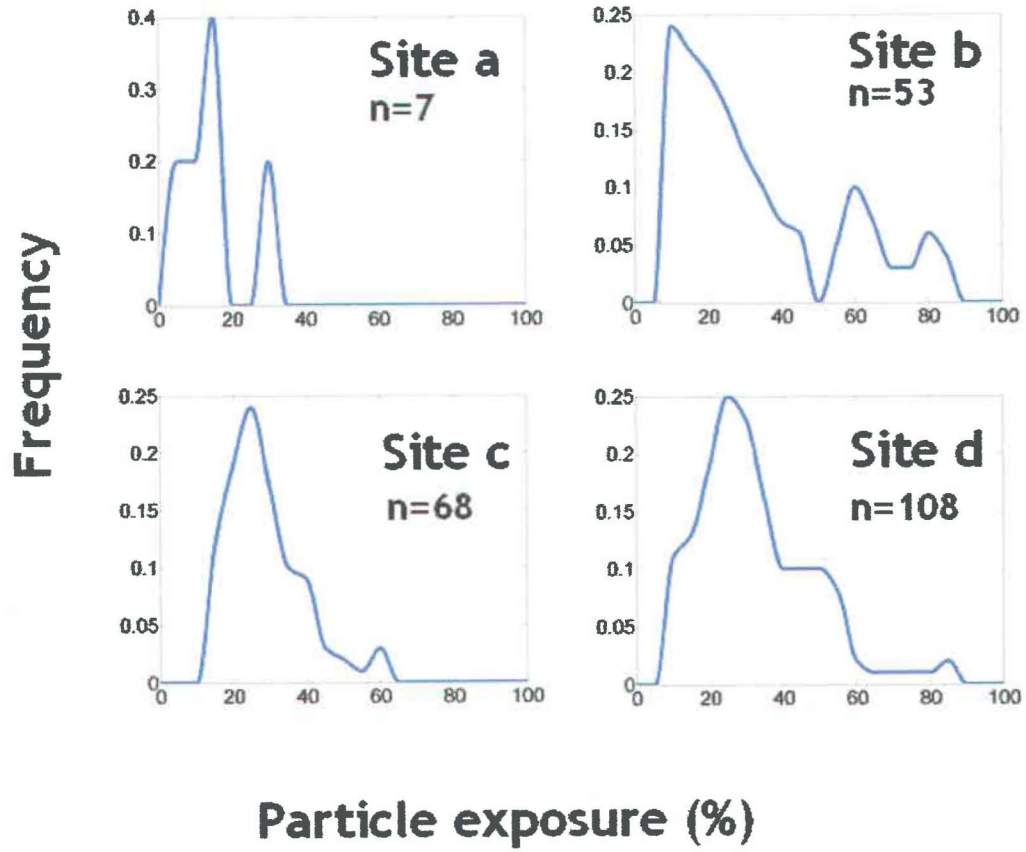
Figure 6.7. Frequency distributions for particle exposure results.

Chapitre 7: Predicting concealment space availability in salmonid river gravels

Predicting concealment space availability in salmonid river gravels

Patrice E. Carbonneau[1†]

Normand E. Bergeron [1]

Stuart N. Lane [2]

1 Université du Québec, INRS-ETE, 880 chemin Ste-Foy, CP 7500, G1V 4C7, Québec, Canada, phone: (418) 654-2647 fax: (418) 654-2615 email: pcarbonn@nrcan.gc.ca

2 School of Geography, University of Leeds, Leeds, UK

*Contribution to the program of CIRSA (Centre Inter universitaire de Recherche sur le Saumon Atlantique)

† Corresponding author

7.1 Résumé

Cet article présente les résultants d'une étude ayant pour objectif d'établir les premier models prédictifs pour la disponibilité de refuges dans les graviers fluviaux. La régression logistique est appliquée pour modéliser la probabilité de présence d'un interstice en fonction de la taille des grains et de l'agencement des particules afin de vérifier l'hypothèse que la taille est une mesure suffisante pour prédire la disponibilité de refuges pour les saumons juvéniles durant la période hivernale. L'agencement des gravillons est quantifié avec des nouvelles méthodes capables de mesurer la dimension fractale, la rugosité du lit, le chevauchement des particules et la présence de sable en surface. Les interstices ont été recensés manuellement sur le terrain ainsi que les tailles de grains. Les résultats montrent que, pour cette étude, l'utilisation de la taille seule prédit avec succès 50% des observations. Le modèle le plus parcimonieux est une fonction de la taille, la rugosité et la présence de sable en surface et ce modèle prédit avec 86% de succès les observations de vides. Les résultats suggèrent donc que l'agencement des particules doit être considéré afin d'obtenir des estimés valables de la disponibilité d'habitat hivernal pour le saumon juvénile.

7.2 Abstract

This paper presents the results of a study aimed at establishing the first predictive relationships for concealment space availability in fluvial gravels. Logistic regression is applied to model the presence of voidspaces as a function of grain size and measures of gravel bed surface structure in order to test the assumption that particle size alone is sufficient to predict the availability of concealment spaces for juvenile salmonids during winter. Gravel bed surface structure is evaluated with newly developed measures allowing for the quantitative evaluation of surface fractal dimension, surface roughness, particle arrangement and surface coverage of sand. Voidspaces for the model were manually measured in the field along with maximum grain size for each study parcel. The results show that, for this study, use of grain size successfully predicts 50% of the observed voids. Furthermore, this work shows that the most successful and parsimonious set of predictors is: grain size, surface roughness and sand coverage with a success rate of 86%. These results suggest that the inclusion of gravel structure is necessary for the reliable prediction of the concealment spaces present in a gravel river bed.

7.3 Introduction

The world decline of atlantic salmon populations is well established and documented (Parrish *et al.* 1998). Consequently, much effort is being devoted to management of the fluvial habitat necessary for egg and juvenile survival. In cold climate rivers, management practices must include over-wintering survival requirements. During winter months, juvenile salmon display a shift in behaviour and habitat requirements. When water temperature drops below a threshold of 8-10 °C, juvenile salmon use the interstitial voidspaces of the riverbed as concealment spaces during the day to avoid endothermic predators and minimize energy expenditure (Rimmer *et al.* 1983; Cunjak 1988). This use of voidspaces for concealment therefore makes the riverbed an important component of the winter habitat of juvenile salmon. However, the assessment of available winter habitat for management and modelling purposes is currently limited by a lack of suitable methods (Cunjak *et al.* 1998). Current methods are based on in stream observations of the use of concealment spaces during winter (Cunjak 1988). Rimmer *et al.* (1983), observed that during winter, juvenile salmon are generally found in proximity to clasts of roughly 17 cm in size. Therefore, habitat availability is often inferred from observation of substrate sizes with coarse substrates being associated to high diurnal winter habitat availability (Bourdages and Bujold 2000). However, the underlying hypothesis that suitable voidspaces are associated to the presence of coarse substrate has not been tested. Meyer and Griffith (1997) have shown that, in artificial substrates of identical size, juvenile rainbow trout preferentially select concealment spaces where particle arrangement yields the most voidspaces. This suggests that particle size is not the only relevant variable for the prediction of habitat availability. The effect of sand infiltration on egg and alevin survival has been studied (Crisp and Carling 1989, Sear 1993). However few studies have considered the effects of sand infiltration on concealment spaces used by salmon parr and fry.

The main objective of this paper is to test the hypothesis that size alone is an adequate predictor of voidspaces in fluvial gravels. These parameters were then used to test gravel structure as a predictor of voidspaces.

7.4 Methods

7.4.1 Data collection

The data collection procedure was designed to obtain a data set which could allow for a quantitative study of the relationships between the number of voids and their size to the surface roughness, fractal dimension, surface coverage by sand, particle overlap, and grain size. Fieldwork was carried out on three salmon rivers in Quebec, Canada: the Sainte-Marguerite, the Petite-Cascapédia and the Bonaventure. For each river, ten 0.4 X 0.4 m study sites of exposed gravels were selected. Each site was then divided into 4 parcels of 0.2 X 0.2 m yielding 120 parcels. Sites were selected to obtain a range of grain sizes, sand to large cobbles, a range of superficial sand coverage and a range of particle overlap.

7.4.2 Surface topography

Detailed topographic information for each study parcel was established from high-resolution digital elevation models measured with the digital photogrammetry procedure described in chapter 4. This method of cost-effective close range digital photogrammetry was applied to each selected study parcel and yielded high-resolution digital elevation models (DEMs) with a spacing of 0.001 m in the x and y directions. Therefore, the micro-topography of each study parcel was described by 40 000 elevation measurements. The accuracy of the model, discussed in chapter 4, was evaluated at ± 2-8mm with smoother surfaces having less error than rougher ones.

7.4.3 Surface roughness

The DEMs were used to calculate surface roughness and surface fractal dimension. In order to quantify surface roughness with a single meaningful

number, a new roughness measure was developed. Called the R_{84}, it gives a measure of the vertical extent of the surface for a chosen horizontal scale. In the case of this study, a horizontal scale of 20 mm was selected since it represents a scale comparable to the lateral dimensions of a juvenile salmon. The first step in calculating the R_{84} for a given surface is to calculate the absolute elevation differences for all points of the DEM separated by the desired horizontal distance (in this case 20mm) and plotting their frequency distribution. The R_{84} is then obtained by taking the 84th percentile of this distribution. The selection of the 84th percentile is analogous to the use of the 84th percentile as representative of the coarse fraction of a grain size distribution. Depending on the focus of a given study, other percentile values could be used as is the case for grain size curves. Therefore the R_{84}, in mm, gives a measure of the height of the largest edges in a surface. Rough surfaces will have larger values of R_{84} than smooth surfaces. The R_{84} measure was not found to be correlated to D_{100} with a Pearsons coefficient of 0.29 taken from 120 test surfaces.

7.4.4 Surface fractal dimension

The fractal dimension of each study parcel was obtained following the methods discussed in chapter 5. This method employs pattern recognition algorithms applied to semi-variograms obtained from DEM data to automatically identify self-affine scaling bands in all surface directions and then to calculate the fractal dimension of each scaling band. In order to reduce omnidirectional fractal dimension to a single value, the mean fractal dimension at a scale of 20mm for all directions was used. The fractal dimension was found the be weakly correlated to D_{100} with a Pearsons coefficient of -0.40.

7.4.5 Overlap of surface particles

The overlap of neighbouring particles is a measure of particle arrangement. Particle imbrication may be defined as a shingle like structure where neighbouring clasts overlap each other. Furthermore, cobble embeddedness may

be defined as the partial burial of cobbles where finer particles such as sand or fine gravels overlap the cobbles. In order to evaluate particle overlap, study parcels were spray painted and once dry, all clasts greater than 10mm were numbered, removed, measured and photographed (chapter 6). Image processing is then applied to automatically calculate the surface percentage of each clast which is covered by paint. Particles covered by a neighbour will have little paint. The percentage of clast surface covered by paint is termed the particle exposure and is equivalent to 100%-(particle overlap)%. Particle overlap is therefore easier to quantify with particle exposure. The particle exposure for each parcel was reduced to a single number by taking the 84th percentile value in the exposure distribution for particles in a given parcel (chapter 6).

7.4.6 Surface coverage by sand

The sand coverage parameter is the percentage of the surface which is visibly occupied by finer particles such as sand. This can objectively be calculated from digital images of the bed surface. In this case, images of the digital photogrammetry survey were use. Sand patches were automatically identified with texture based image segmentation as described in chapter 6. After identification, sand coverage was expressed as the percentage of the surface covered by sand.

7.4.7 Measurement of surface voidspaces

The objective of this step was to manually measure the size all surface voids present on each study site in order to be able to relate voidspaces to gravel bed descriptors. Voidspace measurements were undertaken on the painted and numbered study surfaces before clast removal. A thin steel rod of 3 mm in diameter was used to manually measure the size of each observable void. Voids with openings in both the horizontal and vertical planes were considered. Overhangs associated to larger clasts were also considered. For each void greater than 3mm, the depth and the dimensions of the opening were measured

which gives three orthogonal measurements of void size. After each void was measured, the numbers of the rocks constituting the void were recorded thus giving an approximate position and allowing to relate a void to its constituting clasts.

The resulting data set can therefore be summarised as 120 parcels with a DEM giving high resolution topographic information, a quantitative measure of particle exposure and sand coverage, the size of each surface clast and, a detailed survey of surface voids giving, for each parcel, the number of voids and their size.

7.4.8 Linear regression modelling

Linear regression was applied to study the relationship between voidsize and associated clast size. For each clast, the size of the largest associated void was used as associated void size for a given clast. Multiple regression was then applied to model the size of measured voids as a function of both rock size (b axis) and particle exposure.

7.4.9 Logistic regression modelling

Logistic regression was used to model the probability of finding at least one voidspace in a parcel as a function of maximum grain size, roughness, particle exposure, sand coverage and fractal dimension. Within the voidspace data set, only voids with a minimal depth of 20mm and openings of 10mm X 10mm were selected in order to maintain a scale of voidspaces which roughly corresponded to the scale of juvenile salmon. Examination of the spatial distribution of the voidspaces with dimensions greater than 20mm X 10mm X 10mm revealed that they were located within 40 surfaces. The distribution was as follows: 25 surfaces had a single voidspace, 12 surfaces had 2 voidspaces and 3 surfaces had 4 voidspaces. The model was therefore constructed with these 40 surfaces. To complete the model and supply surfaces without voids, 40 voidless surfaces were randomly selected from the remaining 80 surfaces. This yielded a total of

80 usable study surfaces. Logistic regression curves were then fitted with all linear variable combinations. Pearson coefficients for all combinations of predictors were never higher than 0.49 indicating that the variables were not correlated. Therefore, in the absence of strong correlations, interaction terms were not considered. Since no physical reason can justify the application of second and third powers to the descriptors, only linear combinations of variables were used. Logistic regression models were then verified with the standard Wald statistics (Hosmer and Lémeshow, 1989). Models which passed the Wald test were then used to predict the observed voidspaces with the collected gravel bed descriptors. This was done by assuming that if a model predicted that a surface had a probability of voidspace presence greater than 0.5 and that a voidspace was in fact present, the prediction was successful. Similarly, if a model predicted that voidspace presence probability was lower than 0.5 and a given surface was voidless , the prediction was successful.

7.5 Results

7.5.1 Linear regression modelling

Figure 7.1 shows a plot of clast size vs void size. It can be seen that no strong trend exists. Furthermore, several clasts ranging in size from 4 mm to 218 mm have no associated voids. Regression of clast size vs void size yields an r^2 of 0.03. The addition of particle overlap into a multiple linear regression model did not improve the predictive power of the relationship giving a multiple r^2 of 0.02.

7.5.2 Logistic regression modelling

Table 7.1 gives the results for all models that passed the Wald test within the 95% confidence level. The 3 variable model with D_{100}, SC and R_{84} was selected as the most parsimonious model with the best predictive capacity. The logistic equation for this model is:

$$P=\frac{\exp(-3.855+0.023D_{100}-0.081FC+0.085R_{84})}{1+\exp(-3.855+0.023D_{100}-0.081FC+0.085R_{84})} \tag{7.1}$$

where P, the probability of a voidspace of suitable size being present, is a function of maximum diameter (in mm), sand coverage (in %) and surface roughness (in mm). Figure 7.2 shows a graphic representation of this model. In figure 7.2a, the probability is plotted as a function of size and roughness with sand coverage being held constant at 0%. In figure 7.2b the probability is plotted as a function of size and sand coverage with the roughness held constant at 30mm which is the median value for roughness in the data set. Table 7.2 shows the odds ratios for the 3 variable model presented in equation (7.1). The odds ratio presented here gives the factor by which the probability of finding a void increases if a given parameter increases by 10% of its range. Note that if the odds ratio is greater than 1, the probability increases and if the odds ratio is less than unity the probability decreases.

7.6 Discussion

The presence of clasts with sizes of 4 to 216 mm without associated voidspaces and the failure of multiple regression modelling suggest that the formation of a voidspace is not controlled by a single particle, thus implying that bed structure does play a role in voidspace availability. This is supported by the fact that a surface based approach such as was applied in the logistic regression model gave significant results. The first important result obtained by regression modelling is that if the maximum clast diameter alone is considered, the model passes the Wald test but only 50% of the voidspace presence predictions are correct. Whilst the most complex five variable model predicted presence or absence of voidspace with 85% success, it can be seen that the most parsimonious model includes D_{100}, R_{84} and SC. Figure 1a shows that voidspace presence is very sensitive to roughness. For example, examination of figure 7.2a shows that surfaces with a maximum particle diameter of 75mm and a roughness of 10mm have a 20% chance of having a voidspace. However, if the roughness is increased to 60mm, the probability of voidspace presence increases to 0.8. As bed material size approaches boulder sizes (>256mm) the probability of finding

voidspaces becomes greater than 0.9. Figure 7.2b also shows a very strong effect of sand coverage. Even for clasts surfaces where D_{100} is 250mm, voidspace presence probability drops below 0.5 if sand coverage (SC) is greater than 60%. For surfaces ranging from 100mm to 150mm in D_{100}, voidspace presence probability drops below 0.5 if sand coverage (SC) is greater than 40%. The odds ratios in table 7.2 confirm the observations of figure 7.2. Odds ratios for D_{100} and R_{84} are of similar magnitude showing that voidspace presence is sensitive to both variables. An increase of 10% of the variable range causes voidpsace presence probability to increase by a factor of 1.5 for D100 and a factor of 1.7 for R_{84}. Sensitivity to sand is also confirmed with a 10% increase in SC causing a decrease of voidspace presence probability by a factor of 0.4.

Conclusion

The results of this study show that voidspace presence probability in cobble size substrates is sensitive to values for D_{100}, R_{84} and SC. This shows that maximum diameter alone is not an adequate predictor of voidspace presence. The results also show that surface voidspaces usable by juvenile salmonids are formed by multiple particles thus supporting the importance of gravel structure. Accurate modelling and assessment of juvenile salmonid habitat will therefore require that the measurement of bed structure in addition to grain sizes be integrated into current field measurement practices.
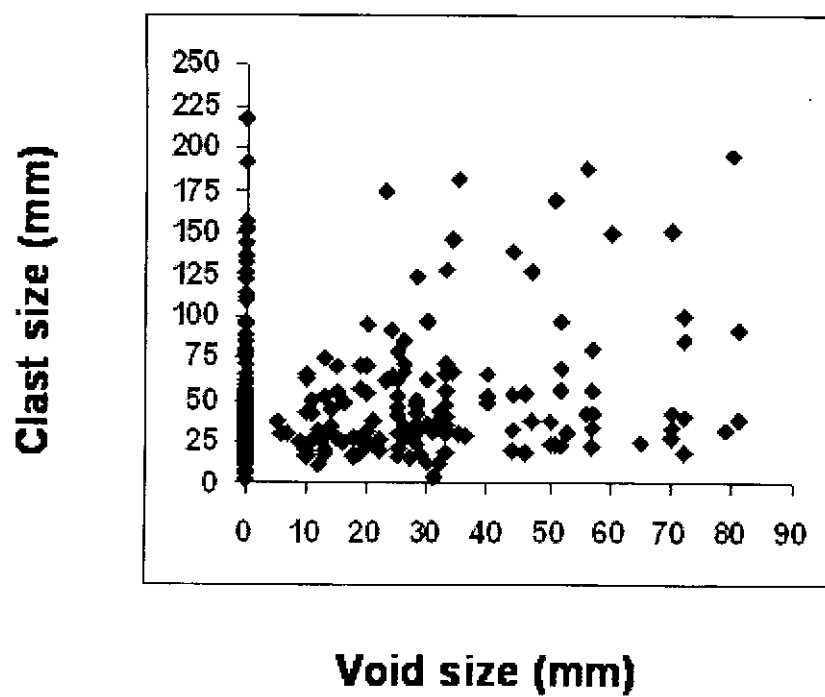
Figure 7.1 Scatterplot of clast size vs void size.
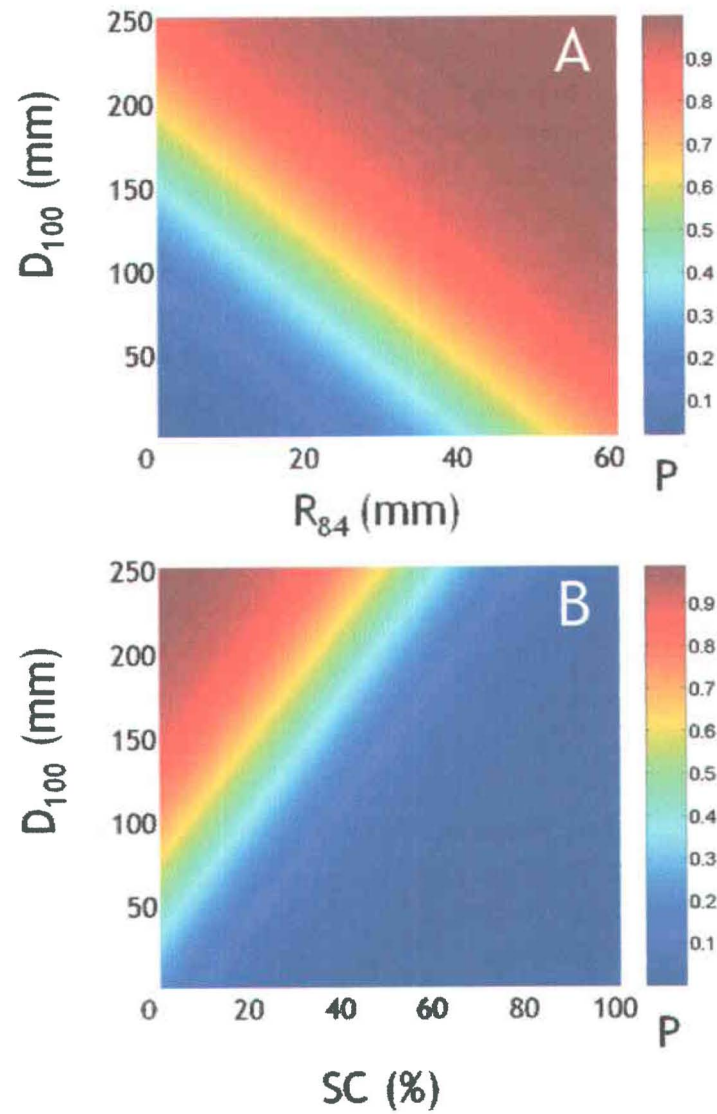
Figure 7.2. Predictive model for voidspace presence. A) voidspace presence probability as a function of D_{100} and R_{84}, SC=0%. B) voidspace presence probability as a function of D_{100} and SC, R_{84}=30mm.

Table 7.1.   Results for logistic regression models.

Model variables	% of explained observations
D_{100}	50
R_{84}	53
SC	50
D_{100} R_{84}	75
D_{100} SC	85
R_{84} SC	76
D_{100} R_{84} SC	86
D_{100} R_{84} D100	79
D_{100} R_{84} SC D	84
D_{100} R_{84} SC D PE	85

Table 7.2. Odds ratios.

model	Parameter Δ	Odds ratio
D_{100}, SC, R_{84}	+20mm D_{100}	1.5
	+ 6mm R_{84}	1.7
	+ 10 % SC	0.4

Chapitre 8 : Conclusion

Nous terminons avec une discussion des approches possibles pour la mise en application des résultats de la thèse. Des moyens techniques sophistiqués ont été développés et appliqués dans le cadre de cette recherche doctorale. Les résultats indiquent que la rugosité des surfaces et le pourcentage de sable en surface doivent être considérés afin de prédire adéquatement la présence d'interstices sur une surface de gravier fluviaux. Par contre, nous ne croyons pas qu'il sera obligatoire de mettre en oeuvre des méthodes aussi complexes que celles décrites dans cette thèse pour mettre à jour les méthodes des travaux d'évaluation d'habitat. De plus, nous croyons que les résultats de la présente thèse peuvent être adaptés pour caractériser les graviers du périmètre mouillé. Whitman *et al* (2003) ont mis au point un système simple permettant de prendre des images de graviers submergés qui pourrais donc permettre d'évaluer le recouvrement de sable des graviers submergés. De plus, la méthode de Whitmat *et al.* (2003) permet de mesurer la taille des graviers submergés. Il manque donc une méthode pour évaluer le R_{84} dans le périmètre mouillé. Nous envisageons 2 solutions possibles.

La première solution s'applique au travaux a petite échelle. Il serait possible de concevoir une machine simple, utilisable autant dans les zones mouillées que sèches, qui mesure la différence d'élévation entre deux points séparés d'une distance horizontale. Cet engin pourrait être utilisé pour échantillonner les différences d'élévation d'une surface et obtenir un estimé du R_{84} de la surface. Un tel prototype surnommé le «bipède», a été développé durant cette thèse (figure 8.1). Les résultats des essais de ce prototype ont montré que l'appareil était trop lourd et qu'il remaniait la surface. La rugosité mesurée ne correspond donc pas à l'état naturel de l'agencement des particules de la surface de graviers à l'étude. Des travaux supplémentaires seront donc nécessaires pour produire un appareil plus léger et pour déterminer un protocole d'utilisation approprié. Malgré ces difficultés, un tel appareil serait d'un grand intérêt. Il permettrait de

mesurer la rugosité des surfaces de graviers dans les zones exhondées et le périmètre mouillé sans recourir à la photogrammétrie. Cependant, de telles méthodes de caractérisation de l'habitat à petite échelle requièrent une quantité importante de travail s'il est nécessaire de caractériser l'habitat de tout un cours d'eau.

La deuxième solution envisageable au problème de la mesure du R_{84} s'applique donc aux études à grande échelle. Les applications récentes de la microtopographie des graviers fluviaux à une échelle inférieure au centimètre utilisent des méthodes de photogrammétrie terrestre (Butler *et al.* 1998, 2001b, chapitre 4). L'application de la photogrammétrie terrestre permet d'obtenir des MNT d'une très haute résolution spatiale mais réduit la superficie des MNT. Ceci est une conséquence directe des limitations technologiques actuelles de résolution des images digitales. Cependant, les progrès techniques dans le domaine de la photographie numérique amènent annuellement une augmentation considérable de la résolution des caméras digitales. Par exemple, la caméra DCS Pro 14n de Kodak inc. est capable de prendre des clichés d'une taille de 13.8 millions de pixels, soit 4200 X 3300 pixels. Une telle caméra montée sur une plate-forme héliportée volant à 155m d'altitude pourrait désormais prendre des images avec une résolution au sol de 1.5 cm sur une dimension d'environ 60 X 40 m. Il est donc concevable qu'à moyen terme, il soit possible de recueillir des informations microtopographiques à l'échelle sous-centimétrique à partir d'imagerie aérienne. Ceci implique qu'avec une série d'images couvrant tout les tronçons d'une rivière, il sera possible d'évaluer le R_{84} à l'échelle centimétrique pour toute la rivière. De plus, Westaway *et al.* (2000) ont montré qu'il est possible d'obtenir des informations topographiques dans le périmètre mouillé par photogrammétrie aérienne. Il est donc concevable que la photogrammétrie puisse éventuellement permettre d'évaluer le R_{84} pour le périmètre mouillé. Les méthodes de traitement d'images et de photogrammétrie ont donc un grand potentiel pour caractériser l'habitat du saumon. Dans

l'hypothèse de la disponibilité d'une série d'images pour toute une rivière, les résultats de cette thèse prennent donc toute leur valeur car ils contribuent de façon importante au développement d'une série de méthodes capables de quantifier les systèmes fluviaux à l'échelle centimétrique sur tout le réseau hydrologique d'un basin versant.
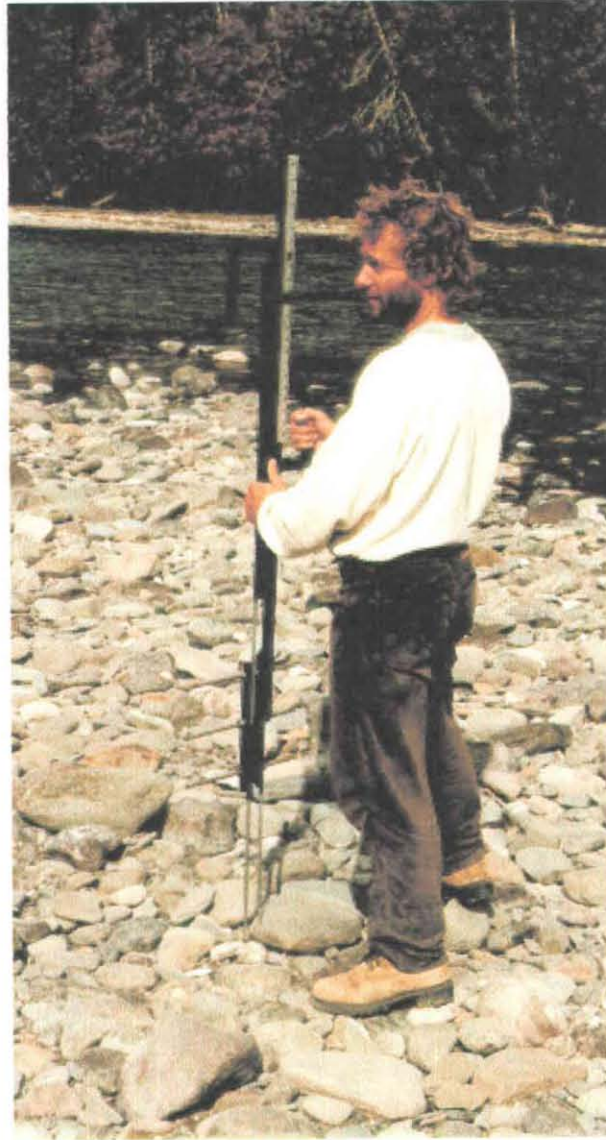
Figure 8.1 Prototype de mesure de rugosité des surfaces.

Annexe A

Recueil des principaux algorithmes

Cet annexe présente les principaux algorithmes développés durant la thèse afin que le lecteur puisse reproduire les résultats de la thèse sans avoir à refaire le travail de développement et de programmation. Le code est présenté dans la syntaxe de l'environnement MATLAB. Le fonctionnement des algorithmes présuppose la disponibilité de MATLAB 6.1 et du module te traitement d'images version 3.0.

Calcul des surfaces de semi-variances

Varsurf.m

Cet algorithme calcule la surface de semi-variance à partir d'un MNT selon l'équation 2.1. Il permet aussi de calculer le profil de semi-variance à partir d'un profil topographique. Avant le calcul, la moyenne de la surface et la tendance générale d'ordre 1 ou 2 (2 par défaut) sont soustrait de la surface. Le résultat est sous forme matricielle.

```
*********************************************************
function svarsurface=varsurf(IN, trendorder, hmap);
%2D or 1D semi-variograms
clock,tic

load (IN)
ZMAT=eval(IN);

if nargin==1
   trendorder=2;
   hmap=1;
end

if size(ZMAT,1)*size(ZMAT,2)>200*200
   disp('go have cofee, this may take a while....')
```

```
  end



  if size(ZMAT,1)==1 & size(ZMAT,2)>1
     ZMAT=ZMAT';
  elseif size(ZMAT,3)>1
     ZMAT=ZMAT(:,:,3);
  elseif size(ZMAT,1)==1 & size(ZMAT,2)==1
     error('input is a scalar')
  end




  %detrending
  if size(ZMAT,1)>1 & size(ZMAT,2)>1
  issurf=1;
  [X, Y]=meshgrid(1:1:size(ZMAT,2), 1:1:size(ZMAT,1));
  coef=poly2fit(X, Y, ZMAT,trendorder);
     if trendorder==1
        plane=coef(1,1)*X+coef(1,2)*Y+coef(1,3);
     elseif trendorder==2

  plane=coef(1,1)*X.^2+coef(1,2)*X.*Y+coef(1,3)*Y.^2+coef(1,4)*X+coef(1,5)*Y+c
  oef(1,6);
     else
        error('trend order too high, 2 max for surfaces')
     end
  ZMAT=ZMAT-plane;
  else
  issurf=0;
  X=1:1:length(ZMAT);,X=X';
  coef=polyfit(X, ZMAT,trendorder);
  plane=polyval(coef,X);
  ZMAT=ZMAT-plane;
  end
```

```
%matrix size and lag definition
[ZX, ZY]=size(ZMAT);
lagxmax=floor(ZX/2);
lagymax=floor(ZY/2);

% reverse semi-variance matrix
if issurf==1
RZMAT=fliplr(ZMAT);
end


%semi-variance


if issurf==1
    svar=zeros(lagxmax, lagymax);
    rsvar=svar;

  for lagy=0:lagymax

            for lagx=0:lagxmax

            svar(lagx+1,lagy+1)=sum(sum((ZMAT([1:ZX-lagx],[1:ZY-lagy])-
ZMAT([lagx+1:ZX],[lagy+1:ZY])).^2))/(2*(ZX-lagx)*(ZY-lagy));

            rsvar(lagx+1,lagy+1)=sum(sum((RZMAT([1:ZX-lagx],[1:ZY-lagy])-
RZMAT([lagx+1:ZX],[lagy+1:ZY])).^2))/(2*(ZX-lagx)*(ZY-lagy));
        end
    end

else
    svar=zeros(lagxmax, 1);


            for lagx=0:lagxmax
```

```
        svar(lagx+1)=sum(sum((ZMAT([1:ZX-lagx])-
ZMAT([lagx+1:ZX])).^2))/(2*(ZX-lagx));
    end

end


%final matrix
if issurf==1
surf=zeros(2*size(svar));
dim=size(svar);
surf([1:dim(1,1)],[1:dim(1,2)])=flipud(fliplr(svar));
surf([1:dim(1,1)],[(dim(1,2)+1):2*dim(1,2)])=flipud(rsvar);
surf([(dim(1,1)+1):2*dim(1,1)],[1:dim(1,2)])=fliplr(rsvar);
surf([(dim(1,1)+1):2*dim(1,1)],[(dim(1,2)+1):2*dim(1,2)])=svar;

%stripping the repeated values along central cross
surf2=[surf(:,[1:size(surf,2)/2]) surf(:,[size(surf,2)/2+2:size(surf,2)])];
surf3=[surf2([1:size(surf2,1)/2],:);surf2([size(surf2,1)/2+2:size(surf2,1)],:)];
surf=surf3; clear surf2, clear surf3

else
surf=svar;
end

svarsurface=surf;



%saving
sv=['sv',IN];
cd ('C:\Documents and Settings\Pat\Mes documents\semi-var02')
eval([sv , '=surf;'])
save([sv], [sv])


disp('Semi-variogram calculated')
```

```
toc

if hmap==1
   hdmap(sv,0);
end
```

Carte de dimension fractale

Autohdmap.m

Cet algorithme calcule la carte de dimensions fractales à partir d'une surface de semi-variance produite par varsurf.m. Le programme fait appel à la sous-routine findbands2.m pour identifier les bandes fractales par vision numérique.

```
*************************************************************
function hmap=autohdmap(svin,print,lag);

% function hmap=autohdmap('svin',lag, print);
% re-projected semi-variogram with Hausdorff dimension map
% this function plots the semi-variogram as direction vs log(lag vs log (SV) and also
plots
% a map of Hd.  The Hd map is evaluated line detection and statistical F-tests to ID
regions where linear fits are
% appropriate.  Enter svin as an alpha string with the quotes, the default lag is 1.
% the output is a 3D matrix with the values of Hd in the first band, the reprojected
SV in the second
% the direction meshgrid in the third and the lag mashgrid in the fourth.  The output
variable is saved
% if print =1, figures will be plotted


tic
disp('loading SV')

if isstr(svin)==1
load (svin)
x=eval(svin);
hmap=['hdmap',svin];
sstr=0;
else
```

```
    x=svin;
    svin=num2str(svin);
    sstr=1;
  end

  if nargin==1
     lag=1;
     print=1;
  elseif nargin==2
     lag=1;
  end

  %resize the semi-variogram to be square
  sq=floor(min(size(x)))-1;
  sq=250;
  if min(size(x))==size(x,1)
     diff=floor((size(x,2)-size(x,1))/2);
     x=x(:,[diff+1:size(x,2)-diff]);
  else
     diff=floor((size(x,1)-size(x,2))/2);
     x=x([diff+1:size(x,1)-diff],:);
  end

  %extract the profiles from 0 to 178 degrees
  disp('extracting SV profiles')


  n=1;
  for angle=0:pi/90:(pi-pi/90)
     [profil, xax]=extract_profile(x,angle,lag);
     xaxmatrix([1:length(profil)],n)=log10(xax);
     cylmatrix([1:length(profil)],n)=log10(profil);
     n=n+1;
  end
```

% interpolation correction for unequal lag spacing as a function of profile direction

```
cylmatcorr=zeros(size(cylmatrix));
limit=max(max(xaxmatrix));,
newx=0:1/100:limit;, newx=newx';
cylmatcorr=zeros(length(newx),90);
for npr=1:90
    cylmatcorr(:,npr)=interp1(xaxmatrix(:,npr),cylmatrix(:,npr),newx,'v5cubic');
end
[direction, lagdistance]=meshgrid(0:2:178,0:(newx(2)-newx(1)):max(newx));


%automated band ID with line detection
disp('running band identification')


bandcell=findbands2(cylmatcorr);, save bandcell bandcell
%load bandcell
%verification and adjustment of bands
disp('statistical testing of bands')
local_Hausdorff=NaN*ones(size(cylmatcorr));
fthreshold=sqrt(fq(0.99, (sq/2)^2, (sq/2)^2));
for dir=1:1:90
    scalingbands=bandcell{dir};


    for band=1:size(scalingbands,1)
        %initial regression
        xmin=scalingbands(band,1);, xmax=scalingbands(band,2);
        nonans=(isfinite(cylmatcorr([xmin:xmax],dir)));
        lim=find(nonans==1);,
        xmin=xmin+min(lim)-1;, xmax=xmin+max(lim)-1;
        reg=polyfit(newx([xmin:xmax]), cylmatcorr([xmin:xmax],dir),1);
        fxmin=xmin-25;, fxmax=xmax+25;
        if fxmin<=0
            fxmin=1;
        end
        if fxmax>length(newx)
            fxmax=length(newx);
```

```
        end
        fit=polyval(reg,newx([fxmin:fxmax]));
        resids=cylmatcorr([fxmin:fxmax],dir)./fit;
        uthresh=resids<fthreshold; lthresh=resids>(1/fthreshold);
        threshpassed=(3-0.5*reg(1,1)).*(uthresh & lthresh);
        local_Hausdorff([fxmin:fxmax],dir)=threshpassed;

    end

end
%set points that failed linearity test to NaN
for n=1:size(local_Hausdorff,1)
   for m=1:size(local_Hausdorff,2)
     if local_Hausdorff(n,m)==0
        local_Hausdorff(n,m)=NaN;
     end
   end
end




if print==1
%figures


figure, subplot(2,1,1)
surf(direction([1:size(local_Hausdorff,1)],[1:size(local_Hausdorff,2)]),
lagdistance([1:size(local_Hausdorff,1)],[1:size(local_Hausdorff,2)]),cylmatcorr),
view([0 90]), colorbar, title(['reprojected semi-variogram for ',svin]), axis('ij')
ylabel('log(lag)'),


subplot(2,1,2),
surf(direction([1:size(local_Hausdorff,1)],[1:size(local_Hausdorff,2)]),
lagdistance([1:size(local_Hausdorff,1)],[1:size(local_Hausdorff,2)]),local_Hausdorff),
```

```
view([0 90]), colorbar, title(['Hausdorff dimension map for ',svin]), axis('ij')
ylabel('log(lag)'),

% formatting the figure
h=gcf;, h1=get(h,'Children');
s1=h1(1);, s1surf=get(s1,'Children');
set(s1,'XLim',[0 178]), set(s1,'Ylim',[0 limit]), set(s1,'Color','k')
set(s1surf,'EdgeColor','interp')

s1=h1(3);, s1surf=get(s1,'Children');
set(s1,'XLim',[0 178]), set(s1,'Ylim',[0 limit]), set(s1,'Color','k')
set(s1surf,'EdgeColor','interp')

cb1=h1(2);,
cb2=h1(4);,
set(get(cb2,'XLabel'),'String','log(SV)');
set(get(cb1,'XLabel'),'String','D');
end

%outputs

    hdmap(:,:,1)=local_Hausdorff;
    hdmap(:,:,2)=cylmatcorr;
    hdmap(:,:,3)=direction;
    hdmap(:,:,4)=lagdistance;

    if sstr==0
    eval([hmap,'=hdmap;'])
    cd d:\apat\hdmap02
    save([hmap],[hmap])
    end

disp('done')
toc
```

findbands2.m

Cet algorithme procède à l'identification automatisée des bandes fractales dans un profil de semi-variance par vision numérique. L'algortithme fait appel à makelineimage.m pour transformer les profile en images et à mktemplate.m pour créer les kernels de convolution nécessaires.

****

```
function cell=findbands2(repsv);

% automated detection of linear sections in an image of a 1D SV function.  Uses
iterated line detection kernels.

for dir=1:1:90
prof=repsv(:,dir);

image=makelineimage(prof);

threshmap=(50^2-(filter2(ones(50,50),image,'same')));
na=1;
xb=zeros(65,3);

for angle=10:1:75
   t=mktemplate(50,angle);
   b=filter2(t,image,'same');,
   %adaptive thresholding
   bbw=(b>=threshmap);

   bbw=bwmorph(bbw,'bridge');
   %figure,subplot(2,2,1), imagesc(b), axis('square'), subplot(2,2,2),
imagesc(threshmap), axis('square'), subplot(2,2,3), imagesc(image), colormap(gray),
subplot(2,2,4), imagesc(bbw),colormap(gray),pause,close
   [bands, num]=bwlabel(bbw,8);
```

```
   clear bandsize
   if num>0
     for n=1:num
        [x,y]=find(bands==n);
        bandsize(n)=max(y)-min(y);
     end
     n=find(bandsize==max(bandsize));
     [x,y]=find(bands==n(1));
     xb(na,1)=min2d(y);
     xb(na,2)=max2d(y);
     xb(na,3)=xb(na,2)-xb(na,1);
     if xb(na,3)<25
        xb(na,1)=0;
        xb(na,2)=0;
        xb(na,3)=xb(na,2)-xb(na,1);
     end
     na=na+1;
   elseif num==0
     na=na+1;
   end
end


%multiple bands
bnum=1;
for nxb=2:length(xb)
   if (xb(nxb,3)~=0) & (xb(nxb,3)>xb(nxb-1,3))
     %if xb(nxb,1)<=49
     %   xb(nxb,1)=50;
     %end
     bandextent(bnum,[1:2])=[(xb(nxb,1)-50) xb(nxb,2)];
     bandend=0;


   elseif (xb(nxb,3)~=0) & (xb(nxb,3)<xb(nxb-1,3)) & (bandend==0)
     bnum=bnum+1;
     bandend=1;
```

```
      end
end


%no bands
if sum(xb(:,3))<=0
    bandextent=[1 1 0];
    disp(['no bands detected for direction ', num2str(2*dir)])
end


cell{dir}=flipud(sort(bandextent,1));,


%debugging figures
%axex=1:251;,figure, plot(axex,prof),hold on,
plot(axex([bandextent(1,1):bandextent(1,2)]),prof([bandextent(1,1):bandextent(1,2
)]),'go') , pause(3), close,
%close, flipud(sort(bandextent,1)),figure, subplot(2,1,1), plot(xb(:,3)),
subplot(2,1,2),plot(prof), pause(2)



clear bandextent
end
```

makelineimage.m

Ce programme transforme un profil de semi-variance tracé sur échelles logarithmiques en une image binaire du profil. Après la transformation, le profil peut être analyser par méthodes de traitement d'images.

```
*****************************************************************
function lineimage=makelineimage(prof)

%makes a binary image from 1D SV profile data

lineimage=zeros(length(prof)+51,length(prof)+51);
%lineimage=zeros(250+49,250+49);
for n=1:length(prof)-1
   yim=(length(prof))*(prof(n)-min(prof))/(max(prof)-min(prof));,
yim=round(yim)+1;
   if isnan(yim)==0
     lineimage(yim+25,n+25)=1;

   end
end

lineimage=flipud(lineimage);

%thickening
lineimage=bwmorph(lineimage,'dilate');
```

mktemplate.m

Cette sous-routine crée les kernels de convolution nécessaires à la détection des lignes par vision numérique.

```
*****************************************************************

function temp=mkline(a,b)

%create a line detecting kernel of size a and orientation b. (positive slope only)

if b<0
   error('orientations from 0 to 90 only');
end

temp=ones(a,a);, temp=temp*-1;
m=tan(b*pi/180);

if b<=45
   x=1:a;
   y=round(m.*x);
   for n=1:a
     if y(n)==0
       y(n)=1;
     end
     temp(x(n),y(n))=(a-1);
   end
elseif b>45
   y=1:a;
   x=round((1/m).*y);
   for n=1:a
     if x(n)==0
       x(n)=1;
     end
```

```
        temp(x(n),y(n))=(a-1);
    end
end

temp=flipud((temp)');
```

Quantification du recouvrement des particules grossières

Analysepaintboard.m

Ce programme calcule le pourcentage de peinture present sur les roches soumises à l'analyse du recouvrement par les particules voisines. Le programme fais appel à la sous-routine paintboardsegment.m pour créer des groupes de pixels correspondants à chaque roche individuelle.

****

```
function paintpercent=analysepaintboard(image)

%program to determine the percentage of paint covering rocks on a black board
close all
I=imread(image,'jpg');


%scale ID
figure, imagesc(I);
disp('select scaling control points')
refpoints=ginput(4);
dist1=sqrt(((refpoints(1,1)-refpoints(2,1))^2)+(((refpoints(1,2)-
refpoints(2,2))^2)));
dist2=sqrt(((refpoints(3,1)-refpoints(4,1))^2)+(((refpoints(3,2)-
refpoints(4,2))^2)));
dist=(dist1+dist2)/2;
%scale=input('object space distance?  ')/dist;
scale=260/dist;
close all

%segment rocks
SI=paintboardsegment(I(:,:,1),'no');
nedit=1;
EI=I;
```

```
while nedit>0

EI(:,:,3)=uint8((double(SI).*255)+double(I(:,:,3)));
figure, imagesc(EI),axis('square'), nedit=input('how many edits?  ');

if nedit>=1
   for n=1:nedit
      a=roipoly(EI);
      SI=(a | SI);


   end
   clear a
end
close all
end

%labelling and rock size
L=bwlabel(SI);
STAT=regionprops(L,'EquivDiameter');



%rock matching and pixel count
disp('select upper and lower faces of rocks, click at (0,0) to stop'), pause(1)

m=1;
num=1;
paintcell{1,1}=0;
paintcell{1,2}=0;
while num~=0
figure, imagesc(I),axis('square'), f=gcf;
paintpercent(m,1)=m;, unzoom
num=input('rock number? ');
unzoom,select=ginput(2);, select=round(select);
if select(1,1)<25
   break
end
```

```
rock1=bwselect(SI, select(1,1), select(1,2)) ;
rock2=bwselect(SI,select(2,1),select(2,2));
rockgroup(m,[1:2])=[L(select(1,2), select(1,1)) L(select(2,2), select(2,1))];
close(f);
if rockgroup(m,1)>0 & rockgroup(m,2)>0
%pixel counts
[y,x]=find(rock1==1);

hsvI=rgb2hsv(I([min(y):max(y)],[min(x):max(x)],[1:3]));
pixelcount1=0;
newy=y-min(y)+1;
newx=x-min(x)+1;
 for mm=1:length(x)
   if ((hsvI(newy(mm), newx(mm),1)<0.1) & (hsvI(newy(mm), newx(mm),2)>0.5) &
(hsvI(newy(mm), newx(mm),3)>0.5))
   pixelcount1=pixelcount1+1;
   I(y(mm),x(mm),1)=255;
   I(y(mm),x(mm),2)=1;
   I(y(mm),x(mm),3)=1;
   else
   I(y(mm),x(mm),1)=1;
   I(y(mm),x(mm),2)=1;
   I(y(mm),x(mm),3)=255;
   end
 end
 pixelcount1=100*pixelcount1/length(x);
 clear hsvI

[y,x]=find(rock2==1);
hsvI=rgb2hsv(I([min(y):max(y)],[min(x):max(x)],[1:3]));
pixelcount2=0;
newy=y-min(y)+1;
newx=x-min(x)+1;
 for mm=1:length(x)
   if ((hsvI(newy(mm), newx(mm),1)<0.15) & (hsvI(newy(mm), newx(mm),2)>0.35)
& (hsvI(newy(mm), newx(mm),3)>0.65))
```

```matlab
        pixelcount2=pixelcount2+1;
        I(y(mm),x(mm),1)=255;
        I(y(mm),x(mm),2)=1;
        I(y(mm),x(mm),3)=1;
        else
        I(y(mm),x(mm),1)=1;
        I(y(mm),x(mm),2)=1;
        I(y(mm),x(mm),3)=255;
        end
    end
    pixelcount2=100*pixelcount2/length(x);
    clear hsvI,
    paintpercent(m,1)=round((pixelcount1+pixelcount2)/2);
    paintpercent(m,2)=scale*(STAT(rockgroup(m,1)).EquivDiameter+STAT(rockgroup(m
    ,2)).EquivDiameter)/2;
    paintpercent(m,3)=num;
    m=m+1;
    save crash paintpercent
    else
        disp('WARNING no rock selected, pick again')
    end
end

paintpercent=paintpercent([1:size(paintpercent,1)-1],:);

out=['PE',image];
eval([out,'=paintpercent;'])

rep=['C:\Documents and Settings\Pat\Mes documents\paintresults']

cd (rep)
save ([out],[out])
```

paintboardsegment.m

Cet algorithme est la sous-routine de segmentation appliqué par
analysepaintboard.m. Il procède par seuillage de la bande rouge.

****

```
function SI=paintboardsegment(I,plotfig)

%segments painted rocks on a black background

tic
DI = imadjust(I, [], [0 1]);
%I=uint8(double(I)+150);
BWs = edge(DI, 'sobel');
se90 = strel('line', 3, 90);
se0 = strel('line', 3, 0);
BWsdil = imdilate(BWs, [se90 se0]);
BWdfill = imfill(BWsdil, 'holes');
BWnobord = imclearborder(BWdfill, 4);
seD = strel('diamond',1);
BWfinal = imerode(BWnobord,seD);
SI = imerode(BWfinal,seD);
toc
if strcmp(plotfig,'yes')==1
figure, imshow(BWfinal), title('segmented image');
end
```

Algorithmes d'analyse texturale

Cooc.m

Calcul de la matrice de co-occurrence.

****

```
function y=cooc(I, dx,dy,gl,objectmask);
% coocurence with lag step of dx,dy on image I.  gl gray levels.
%Objectmask  is used to calculate coocurence of an irregular shaped object

%rescale the gray level resolution
I=double(I);, I=round(I./(256/gl));

% COOC matrix
m1=I([1:size(I,1)-dy],[1:size(I,2)-dy]);
m2=I([1+dx:size(I,1)],[1+dy:size(I,2)]);

if nargin==5
objectmask1=objectmask([1:size(I,1)-dy],[1:size(I,2)-dy]);
objectmask2=objectmask([1+dx:size(I,1)],[1+dy:size(I,2)]);
end

y=zeros(gl,gl);
for n=1:gl
  gl1=(m1==n-1);

  for m=1:gl
    gl2=(m2==m-1);
    if nargin==5
      gl1=gl1.*objectmask1;, gl2=gl2.*objectmask2;
    end
    y(n,m)=length((find((gl1+gl2)==2)));
```

```
        end
    end


    if nargin==5
        y=y./sum(sum(objectmask));
    else
        y=y./((size(I,1)-dy)*(size(I,2)-dx));
    end
```

inertmap.m

Cartographie de la propriété d'inertie sur une image selon l'équation 2.12.

****

```
function y=inertmap(I,w,step,dx,dy,gl);

%maps entropy

for o=1:gl
 for p=1:gl
  icoef(o,p)=(o-p)^2;
 end
end

nn=1;,
for n=1:step:size(I,1)-w
   mm=1;
   for m=1:step:size(I,2)-w
     subI=I([n:n+w],[m:m+w]);,
     P=cooc(subI,dx,dy,gl);,
     y(nn,mm)=sum(sum(icoef.*P));
     mm=mm+1;
   end
   nn=nn+1;
end
```

homomap.m

Cartographie de la propriété d'homogénéité sur une image selon l'équation 2.13.

****

```
function y=homomap(I,w,step,gl);

%maps entropy
dx=1;,dy=1;
for o=1:gl
 for p=1:gl
  icoef(o,p)=1/(1+(o-p)^2);
 end
end

nn=1;,
for n=1:step:size(I,1)-w
   mm=1;
   for m=1:step:size(I,2)-w
     subI=I([n:n+w],[m:m+w]);,
     P=cooc(subI,dx,dy,gl);,
     y(nn,mm)=sum(sum(icoef.*P));
     mm=mm+1;
   end
   nn=nn+1;
end
```

energymap.m

Cartographie de la propriété d'énergie sur une image selon l'équation 2.14.

****

```matlab
function y=entropymap(I,w,step,gl);

%maps entropy, s is percentage of sand on surface

if ischar(I)==1
I=imread(I,'JPEG');
end
if ndims(I)>2
   I=rgb2gray(I);
end


dx=1;,dy=dx;




nn=1;,
for n=1:step:size(I,1)-w
   mm=1;
   for m=1:step:size(I,2)-w
     subI=I([n:n+w],[m:m+w]);
     P=cooc(subI,dx,dy,gl);
     y(nn,mm)=sum(sum(P.*P));
     mm=mm+1;
   end
   nn=nn+1;
end
```

entropymap.m

Cartographie de la propriété d'entropie sur une image selon l'équation 2.12.

```
*************************************************************
function y=entropymap(I,w,step,gl);

%maps entropy

if ischar(I)==1
I=imread(I,'JPEG');
end
if ndims(I)>2
   I=rgb2gray(I);
end

dx=1;,dy=dx;



nn=1;,
for n=1:step:size(I,1)-w
   mm=1;
   for m=1:step:size(I,2)-w
     subI=I([n:n+w],[m:m+w]);
     P=cooc(subI,dx,dy,gl);
     y(nn,mm)=sum(sum(P.*log(P+0.00000000001)));
     mm=mm+1;
   end
   nn=nn+1;
end
```

Références

Allan, A. et Frostick, L.E., Framework dilation, winnowing and matrix particle size: the behaviour of some sand-gravel mixtures in a laboratory flume. *J. of Sedimentary Research* (1), 69, 21-26, 1999.

Atkinson, K., *Close range photogrammetry and machine vision*, Caithness-Whitles, 371p, 1996.

Babu K.R. et Nevatia R., Linear feature extraction and description: Computer graphics and image processing, 13, 257-269, 1980.

Bathurst, J.C., Theoretical aspects of flow resistance, dans *Gravel Bed rivers*, édit. par Bathurst J.C., et Thorne, C.P., Wiley, 83-105, 1982.

Bergeron, N.E., Scale-space analysis of stream-bed roughness in coarse gravel-bed streams, *Math. Geo.*, 28(5), 537-561, 1998.

Bourdages D. et Bujold S., Recensement et localisation des nids et des sites de frais du saumon Atlantique dans les Bonaventure et Bonaventure ouest, automne. Rapport pour l'association des pêcheurs de la rivière Bonaventure, 2000.

Brayshaw, A.C., The characteristics and origin of cluster bedforms in coarse-grained alluvial channels, dans *Sedimentology of gravels and conglomerates*, édité par Koster, C.H. et Stell, R.H., Bulletin of the geological society of america, 96, 218-223, 1984.

Bunte, K. et Abt S.R, Sampling Surface and Subsurface Particle-Size Distributions in Wadable Gravel-and Cobble-Bed Streams for Analyses in Sediment Transport,Hydraulics,and Streambed Monitoring. *US dept of agriculture, Gen. Tech report* RMRS-GTR-74, 2001.

Butler, J.B., Lane, S.N. et Chandler, J.H., Assessment of DEM quality for characterisating surface roughness using close range digital photogrammetry, *Photogrammetric Record*, 16(92), 271-291, 1998.

Butler, J.B., Lane, S.N. et Chandler, J.H., Automated extraction of grain-size data from gravel surfaces using digital image processing for hydraulic research , *Journal of Hydraulic Research* , 391, pp.1-11, 2001a.

Butler, J.B., Lane, S.N. et Chandler, J.H., Characterisation of the structures of river-bed gravels using two-dimensional fractal analysis, *Math. Geol.* 333, 301-330, 2001b.

Carbonneau, P.E., *L'effet du transport en charge de fond sur les parties moyennes et turbulentes d'un écoulement fluvial* , mémoire de maîtrise, INRS-Géoressources, 64p, 1998.

Castleman, K.R., *Digital image processing*, Prentice Hall, Upper Saddle River, NJ, 666 p., 1996.

Chandler, J.H. et Padfield, C.J., Automated digital photogrammetry on a shoestring, *Photogrammetric Record*, 15(88), 545-559, 1996.

Chandler, J.H., Effective application of automated digital photogrammetry for geomorphological research, *Earth surface, proceesses and Landforms*, 24(1), 51-63, 1999.

Chin, C.O., Melville, B.W. et Raudkivi, A.J., Streambed armoring, *J. Hydr. Eng.*, 120(8), 1994.

Church, M.A., Mclean, D.G. et Wolcott J.F., Bed gravles: sampling and analysis, dans *Sediment transport in gravel-bed rivers*, édité par Thorne, C.R., Bathurst, J.C. et Hey, R.D., John Wiley & sons, 1987.

Conners, R.W., Trivedi, M.M. et Harlow, C.A., Segmentation of a high resolution urban scene using texture operators. *Computer vision, graphics and image processing*, vol 25, pp 273-310, 1984.

Crisp, D.T. et Carling, P.A., Observations on siting, dimensions and structures of salmonid redds, *J. Fish Biol.*, 34, 119-134, 1989.

Cunjak, R.A., Behaviour and microhabitat of young atlantic salmon (*salmo salar*) during winter, *Can. J. Fish. Aquat. Sci.*, 45, 2156-2160 1988.

Cunjak, R.A., Winter habitat of selected stream fishes and potential impacts from land-use activity, *C. J. Aquat. Sci.*, 53 (suppl. 1), 267-282, 1996.

Cunjak, R.A. et Randall, R.G., In-stream mouvements of young atlantic salmon (*salmo salar*) during winter and early spring, dans *Production of juvenile*

atlantic salmon , salmo salar, in natural rivers, édité par Gibson R.J. et Cutting R.E., Can. Spec. Publ. Fish. Aquat. Sci., 118, 43-51, 1993.

Cunjak, R.A., Prowse, T.D. et Parrish, D.L., Atlantic salmon (*salmo salar*) in winter: 'the season of parr discontent'?, *Can. J. Fish. Aquat. Sci.*, 55 (suppl. 1), 161-180, 1998.

Dowman, I.J., Fundamentals of digital photogrammetry dans: *Close range photogrammetry and machine vision* edited by K.B. Atkinson, 52-77, 1996.

Fraser, N.H.C. et Metcalf, N.B., The costs of becoming nocturnal: feeding efficiency in relation to light intensity in juvenile atlantic salmon, *Functional Ecology*, 11, 385-391, 1997.

Fryer, J.G., Camera calibration dans : *Close range photogrammetry and machine vision* edited by K.B. Atkinson, 156-179, 1996.

Gosh, S.K., *Analytical photogrammetry,* Pergamon Press 203p, 1971.

Gregory, J.S. et Griffith, J.S., Winter concealement by subyearling rainbow trout: space size selection and reduced concealement under surface ice and in turbid water conditions, *Can. J. Fish. Aquat. Sci.*, 74, 451-455, 1996.

Griffith, J.S. et Smith, R.W., Use of winter concealment cover by juvenile cutthroat and brown trout in the south fork of the snake river, *N. Am. J. Fish. Man.*, 13, 823-830, 1993.

Haralick, R.M., Shanmugan, K. et Dinstein, I., Textural features for image classification, *IEEE trans. on systems, man and cybernetics,* vol 3, (6), 610-621, 1973.

Haralick, R.M. et Shapiro, L.G., Image segmentation techniques. *Computer vision, graphics and image processing*, vol 29 pp 100-132, 1985.

Heggenes, J., Habitat selection by brown trout (*salmo trutta*) and young atlantic salmon (*s. salar*) in streams : static and dynamic hydraulic modelling, *Reg. Rivers : Res. Man.*, 12, 155-169, 1996.

Hosmer, D.W., Lemeshow, S., *Applied logistic regression,* John Wiley & Sons, New York, 307 pp., 1989.

IEEE standard 610.4, *IEEE standard glossary on image processing and pattern recognition terminology.* IEEE press, New york, 1990.

Jain, C.S., Armor or pavement, *J. Hydr. Eng.*, 116(3), 436-440, 1990.

Janoo, V.C., Quantification of shape, angularity, and surface texture of base course materials, US Army corps of engineers, CRREL special report 98-1, 1998.

Kironoto, B.A., Graf, W.H., Turbulence characteristics in rough uniform open-channel flow, *Proc. Imstm Civ. Engrs Wat., Marit. & Enregy*, (106), 333-344,, 1994.

Koster, E.H., Rust, B.R., et Gendzwill, D.J., The ellipsoidal form of clasts with practical applications to fabric and size analyses of fluvial gravels, *Can. J. Earth Sci.*, 17, 1725-1739, 1980.

Klingkenberg, B., A review of methods used to determine the fractal dimension of linear features, *Mathematical geology*, 26, 23-46, 1980

Klinkenberg, B. et Goodchild, M.F., The fractal properties of topography: a comparison of methods, *Earth surface processes and Landforms*, 17, 217-234, 1992.

Klingkenberg, B., A review of methods used to determine the fractal dimension of linear features, *Mathematical geology*, 26, 23-46, 1994.

Koster, E.H., Rust B.R. et Gendzwill D.J., The ellipsoidal form of clasts with practical applications to fabric and size analyses of fluvial gravels, *Can. J. Earth Sci.*, 17, 1725-1739, 1980.

Kreyszig, E., *Advanced Engineering Mathematics, sixth edition*, Wiley, 1294p, 1996.

Lane, S.N., Richards, K.S. et Chandler, J.H., Developments in photogrammetry; the geomorphological potential, *Prog. in phys. geog.*, 17, 306-328, 1993.

Lane, S.N., Richards, K.S. et Chandler, J.H., 'Developments in Monitoring and Modelling Small Scale River Bed Topography , *Earth Surface Processes and Landforms* , 19, 349-368, 1994

Lane, S.N., James, T.D. et Crowell, M.D., Application of digital photogrammetry to complex topography for geomorphological research. *Photogrammetric Record,* 16(95), 793-821, 2000.

Lane, S.N., Chandler, J.H. et Porfiri, K. Monitoring flume channel surfaces using automated digital photogrammetry, *ASCE J. Hydr.* , 12710, 871-877, 2001.

Lord Rayleigh, F.R.S., The ultimate shape of pebbles, natural and artificial, *Proc. Roy. Soc.,* 181(A), 107-119, 1942.

Mäki-Petäys, A., Muotka, T., Huusko, A., Tikkanen, P. et Kreivi, P. Seasonal changes in habitat use and preference by juvenile brown trout, *salmo trutta,* in a northern boreal river, *Can. J. Fish. Aquat. Sci.,* 54, 520-530, 1997.

Mandelbrot, B.B., *The fractal geometry of nature,* Freeman, 460p, 1982.

MathWorks inc., *Image processing Toolbox for use with MATLAB, user's Guide* (vol 3). Publié par MathWorks inc.. 2001.

Mason, J.C., Response of underyearling coho salmon to supplemental feeding in a natural stream, *J. Wildl. Manage.,* 40(4), 775-788, 1976.

Metcalf, N.B. et Thorpe, J.E., Anorexia and defended energy levels in over-wintering juvenile salmon, *J. Animal. Eco.,* 61, 175-181, 1992.

Meyer, K.A. et Griffith, J.S., Effects of cobble-boulder substrate configuration on winter residency of juvenile rainbow trout, *N. Am. J. Fish. Aquat. Sci.,* 17, 77-84, 1997.

Nikora, V.I., Goring, D.G., Biggs, B.J.F., On gravel-bed roughness characterization, *water ressources research,* 34(3), 517-527, 1998.

Oliver, M.A., and Webster, R., Semi-variogram for modelling the spatial pattern of land form and soil properties, *Earth surface processes and landforms,* 11, 491-504, 1986.

Otsu, N., A Threshold Selection Method from Gray-Level Histograms, *IEEE Transactions on Systems, Man, and Cybernetics,* vol. 9,1, 62-66, 1979.

Parrish, D.L., Behnke, R.J., Gephard S., McCormick, S. et Reeves, G., Why aren't there more Atlantic salmon? *Canadian Journal of Fisheries and Aquatic Sciences* 55 (Supple.1):281-287, 1998.

Polidori, L., Chorowicz, J. et Guillande, R., Description of terrain as a fractal surface, and application to digital elevation model quality assessment, *Photogrammetric Engineering and Remote Sensing*, 57(10), 1329-1332, 1991.

Powell, M., Patterns and processes of sediment sorting in gravel-bed rivers, *Prog. Phys. Geog.*, 22(1), 1-32, 1998.

Richards, J.A. et Jia, X., 1999, *Remote sensing digital image analysis, an introduction* (3rd ed.), Springer-Verlag, 363p.

Riehle, M.D. et Griffith, J.S., Changes in habitat use and feeding chronology of juvenile rainbow trout (*oncorhynchus mykiss*) in fall and at the onset of winter in Silver creek, Idaho, *Can. J. Fish. Aquat. Sci.*, 50, 2118-2028, 1995.

Rimmer, D.M., Paim, U. et Saunders, R.L., Changes in the selection of mocrohabitat by juvenile atlantic salmon (*salmo salar*) at the summer-autumn transition in a small river, *Can. J. Fish. Aquat. Sci.*, 41, 469-475, 1983.

Rimmer, D.M., Paim, U. et Saunders, R.L., Autumnal habitat shift of juvenile atlantic salmon (*salmo salar*) in a small river, *Can. J. Fish. Aquat. Sci.*, 40, 671-680, 1984.

Robert, A., Statistical properties of sediment bed profiles in alluvial channels, *Math. Geol.* 20(3) 205-225, 1988.

Robert, A., Boundary roughness in coarse grained channels, *Prog. Phys. Geog.*, 14, 42-70, 1991a.

Robert, A., Fractal properties of simulated bed profiles in coarse-grained channels, *Math. Geol.*, 23(3), 367-382, 1991b.

Robert, A. et Richards, K.S., On the modelling of sand bedforms using the semi-variogram. *Earth surface processes and landforms*, 13, 459-473, 1988.

Robson, S., The physical effects of film deformation in small format camera calibration, *Int. Arch. Photogr. Rem. Sens.*, 29(5), 561-567, 1990.

Russ, J.C., *Fractal Surfaces*, Plenum Press. New York, 390pp, 1994.

Sear D.A., Fine sediment infiltration into gravel spawning beds within a regulated river experiencing floods: ecological implications for salmonids. *Reg. Riv.* vol 8. pp 373-390, 1993.

Schroeder, M., *Fractals, chaod and power laws, minutes from an infinite paradise*, Freeman press, 429, 1991.

Short, T., The calibration of a 35mm non-metric camera and the investigation of its potential use in photogrammetry, *Photogrammetric Record*, 14(80), 313-322, 1992.

Short, T., *How to use CUBA, the City University Bundle Adjustment* software and web document available at: www.acts.demon.co.uk, 59 pp, 1999.

Stark, H., et Woods, J.W., *Probability, random processes, and estimation theory for engineers*, Prentice hall, 618p,, 1994.

Stojiic, M., Chandler, J.H., Ashmore, P. et Luce, J., The assessment of sediment transport rates by automated digital photogrammetry, *Photogr. Eng. Rem Sens.*, 64, 387-395,, 1998.

Vision International., *IMAGINE OrthoMAX user's guide*. 121 pages, 1999.

Vladimarsson, S.K. et Metcalf, N.B., Shelter selection in juvenile atlantic salmon, or why do salmon seek shelter in the winter?, *J. Fish Bio.*, 52, 42-49, 1998.

Walker, J.P. et Wilgoose, G.R., On the effect of digital elevation model accuracy on hydrology and geomorphology, *Water Ressources Research*, 35, 2259-2268, 1999.

Welsh, R. et Jordan, T.R., Analytical non-metric close-range photogrammetry for monitoring stream channel erosion, *Photogr. Eng. Rem. Sens.*, 49(3), 367-374, 1983.

Westaway, R.M., Lane, S.N., Hicks, D.M., The development of an automated correction procedure for digital photogrammetry for the study of wide, shallow, gravel-bed rivres. *Earth surface processes and landforms,* 25(2). 1-18, 2000.

Whalen, K.G., Parrish, D.L. et Mather, M.E., Effect of ice formation on selection of habitats and winter distribution of post-young-of-the-year atlantic salmon parr, *Can. J. Aquat. Sci.*, 56, 87-96, 1999.

Whitman, M.S., Moran, E.H. and Ourso, R.T., Photographic techniques for characterizing streambed particle sizes, *Trans. American fisheries society*, 132, 605-610, 2003.

Wong, K.W., Basic mathematics of photogrammetry, dans *Manual of photogrammetry*, édité par Slama, C., American society of photogrammetry, 1050p, 1980.

Wolf, P.R., *Elements of photogrammetry*. Second edition. McGraw-Hill, New York, 628 pages, 1983.